STABILITY, INTERACTIONS, AND ARCHITECTURES OF COLLOIDS WITH ADSORBED ZWITTERIONIC AND ETHYLENE-OXIDE POLYMER COATINGS

by
Matthew G. Petroff

A dissertation submitted to the Johns Hopkins University in conformity with the requirements for the degree of Doctor of Philosophy

Baltimore, MD 21218
October 2018

ABSTRACT

Stability, interactions, and architectures of colloids with adsorbed zwitterionic and ethylene-oxide polymer coatings
Oct. 2018

Matthew G. Petroff, B.E., University of Delaware

Zwitterionic polymer coatings have recently gained attention as stabilizing materials in drug delivery, diagnostic, and other biomedical applications. However, claims of improved stabilization and antifouling properties over traditional polymer chemistries are somewhat inconsistent, and with an unclear mechanistic link between studies at the molecular (e.g. atomic) and macromolecular (e.g. polymer surface) levels.

This thesis uses single-particle, kT-scale measurements of colloidal interactions to probe the mechanics and colloidal stabilization of zwitterionic polymer coatings. Novel amphiphilic block copolymers form dense zwitterionic polymer layers through adsorption onto colloids. Adsorbed copolymers of sufficient repeat units stabilize colloids against deposition and aggregation in high-salt (0-3M NaCl) and physiological media (serum, cell media). Polymers of approximately 2-3 fold reduced contour lengths are needed to stabilize μm-sized colloids when using a common zwitterionic phosphorylcholine polymer (PMPC) than more conventional poly(ethylene oxide) (PEO) copolymers.

Colloidal interaction measurements show that, relative to PEO coatings of similar contour lengths, zwitterionic PMPC coatings exert repulsion over a 2-3-fold longer range. This increased repulsion length is a result of increased zwitterionic layer thickness caused by complete chain extension of the PMPC polymer away from the adsorbate surface. Colloids with PEO and PMPC layers of equivalent thicknesses also possess equivalent interactions and stability against a variety of model biomaterial surface chemistries, further

demonstrating the importance of layer thickness in stabilizing colloids against aggregation and deposition.

The molecular mechanisms for the highly extended zwitterionic brush architectures were studied by using dissolved salt to perturb layer properties and colloidal interactions. Measurements of two contrasting zwitterionic chemistries showed salt-dependent brush extension that is intricately linked to poly-zwitterion solution behavior. Layer architectures result from a balance between attractive dipole-dipole and repulsive solvation and excluded volume molecular interactions. However the relative importance of these attractive and repulsive contributions is dependent on both solution properties (e.g. ion composition) and specific molecular affects (e.g. monomer structure and solvation).

Ultimately, this thesis provides guidance regarding the design of effective polymer coatings for the stabilization of colloids. Polymer layers primarily impart stability through nonspecific macromolecular interactions, and must be of sufficient thickness and density to both screen attractive colloidal interactions and mitigate surfaces non-uniformities. Zwitterionic monomer chemistries only indirectly impact layer stability by influencing polymer layer extension. However zwitterionic chemistries may be useful for the engineering of additional layer properties, such as salt or pH - responsive layer thickness and stabilization.

Committee
Prof. Michael. Bevan (Chemical and Biomolecular Engineering, Advisor)
Prof. Joelle Frechette (Chemical and Biomolecular Engineering, Reader)
Prof. Honggang Cui (Chemical and Biomolecular Engineering, Reader)
Prof. Chao Wang (Chemical and Biomolecular Engineering, Alternate)
Prof. D. Howard Fairbrother (Chemistry, Chair)
Prof. Margarita Herrera-Alonso (Materials Science and Engineering, Reader)
Prof. Robert Leheny (Physics, Alternate)

To Una Kim, the vla ensemble, and the creatures.

ACKNOWLEDGEMENTS

I would like to thank my many friends, family, and coworkers for their emotional and intellectual support throughout graduate school. My parents have given me support in a breadth of personal (vla) and professional directions, always emphasizing the value of personal growth and learning over short-term but more tangible metrics such as money and grades. They have instilled a strong sense of integrity, and taught me to act in a way consistent with my values over the expectations of others. My friends at Redeemer, especially Tad Russo and Sherrill Prantle, have shown the value of an open mind in the search for understanding (and the importance of making time for music). Many friends at JHU, especially Chris, David, Nash, and Elena have shared inspiration and support with issues ranging from politics, science, and biking mishaps. My Merck friends and former coworkers, especially Mike, Jen, John, and Thomas encouraged and motivated me to take the leap into graduate school.

Many people have also impacted my work technically. Most importantly is my advisor, Dr. Bevan, who has been an unimaginably supportive mentor. He worked patiently to instill the technical understanding and persistence needed to forge a successful PhD. I have grown dramatically as a scientist by following his example, especially from his dedication and thorough pursuit of detailed understanding, and his open mind in asking questions. Prof. Herrera-Alonso and her student, Elena Garcia, have been fantastic collaborators, whose discussions and expertise in polymer synthesis were critical in all of the studies in this thesis. I am also very grateful to Prof. Herrera-Alonso for her support, helpful feedback, and encouragement.

My thesis committee members, especially prof Frechette, have extended helpful technical advice and support on issues ranging from project directions to technical

troubleshooting. The past and present Bevan group members have supported with science and professional advice, especially Yugyang, Anna, and Nikki who have been close friends with valuable insights, questions, and opinions. Many undergraduates worked diligently for meager-to-no wages, especially Ray, Hannah, and Jimmy whose work is included in this thesis (and who are all co-authors on manuscripts at various stages of submission).

Most importantly, my wife and companion of 14 years, Una Kim (aka Kabuki, TP, CC) has shown love and support I never dreamed possible and don't deserve. Your encouragement has given me the confidence to work on a PhD; your hard work has given me the freedom to work harder and finish quicker (and to be funemployed for a brief time); and your patience and love has set an example for me to aspire to. I look forward to more music, poetry, and adventures as we spend the rest of our lives together. LUTM

TABLE OF CONTENTS

LIST OF TABLES

LIST OF FIGURES

LIST OF SYMBOLS AND ABBREVIATIONS

POLYMER

PMPC	poly(2-methacryloyloxyethyl phosphorylcholine)
PMAPS	poly(3-(N-2-methacryloyloxyethyl-N,N-dimethyl) ammonatopropanesulfonate
PEO	poly(ethylene oxide)
PPO	poly(propylene oxide)
ARGET-ATRP	activator regenerated by electron transfer-atom transfer radical polymerization
M_n	number averaged polymer molecular weight
M_w	weight averaged polymer molecular weight
M_m	monomer molecular weight
PDI (polymer)	polydispersity index (Mw/Mn)
Lc	contour length ($L_M \times n$)
Lc_w	weight-averaged contour length ($L_M \times n_w$)
L_M	monomer repeat length
L_k	Kuhn length (twice the persistence length)
n_k	number of Kuhn segments (Lc/L_k)
f_0	uncompressed polymer brush free energy / area
L_0	uncompressed thickness
w	polymer excluded volume parameter
σ	graft density of polymer on a surface, chains/area
n	number of polymer repeat units (degree of polymerization)
n_w	number averaged degree of polymerization ($n \times M$w/Mn)
A_2	second osmotic virial coefficient
R_G	radius of gyration

L_0	uncompressed polymer brush steric thickness
L_h	hydrodynamic thickness of polymer
L_F	viscoelastic film thickness

COLLOID

U	interaction potential
U_G	gravitational interaction potential
U_p	polymer interaction potential
U_{vdW}	van der Waals interaction potential
h	surface separation between colloid and planar object
h_M	most probable separation
p_c	observed probability (theoretical probability corrupted by measurement noise)
p_T	theoretic probability
A_{132}	separation-dependent Hamaker function
A	Hamaker constant
d_h	hydrodynamic diameter, usually from DLS
a_h	hydrodynamic radius
σ_h	standard deviation of hydrodynamic diameter
PDI (colloids)	polydispersity (σ_h^2/a_h^2)

OTHER

BSA	bovine serum albumin (globular protein)
DLS	dynamic light scattering
-D	quartz crystal microbalance with dissipation
TIRM	interanal reflection microscopy

1 INTRODUCTION

1.1 Significance and Objective

Chemical functionalization of material surfaces is a common strategy to reduce the adhesion of foreign molecules.[1,2] Effective coatings are especially critical for surfaces in physiological and environmental applications, where materials must repel a wide variety of lipid, protein, and polysaccharide conjugates in high salinity environments and throughout an extended working lifetime. Coating design is especially of key interest in biosensor,[3] implantable medical device,[4,5] 'stealth' drug delivery,[6,7] and filtration[8,9] technologies. Each of these applications commonly requires the selective recognition of a narrow subset of molecules, chemistries, or properties-often at very low concentration-and must display an extremely high rejection of all other molecules. Surface coating design is an active area of research within each of these technologies, with recent publications including novel monomer chemistries[10,11] and functionalization approaches[12] to improve the rejection of off-target molecules.

Surface coatings reduce the adhesion of foreign molecules through two main mechanisms. A coating may reduce interfacial driving forces towards adsorption by lowering the free energy of an exposed surface, such as by rendering an aqueous-presenting hydrophobic surface hydrophilic.[1,13] Many studies have successfully used self-assembled monolayers (SAMs) of small molecules for this affect.[14–17] However, coatings of small-molecules are insufficient for applications involving the stabilization and/or rejection of large macromolecules and colloids, which can exert attractive interactions at 1-20 nanometer distances away from their surface (well beyond the range of typical small-molecule and SAM layer interactions).[1,18]

Further improvements in surface stabilization are obtained by functionalizing a surface with a solvated polymer, which may extend repulsion beyond the 1-20 nm range of typical attractive colloidal interactions.[19–21] In addition to changing surface hydrophobicity characteristics, polymer coatings exhibit a decaying monomer concentration profile away from the coated surface, creating an osmotic repulsion upon approach of foreign molecules to the coated surface.[22,23] The osmotic repulsion is especially pronounced under conditions where the mean polymer spacing, $\sigma^{-1/2}$, is less than the polymer's radius of gyration R_G. Such high surface crowding creates strong lateral interactions between neighboring chains, causing further extension of the polymer away from the graft surface.[24] This condition where $\sigma^{-1/2} < R_G$ is commonly known as the 'polymer brush' regime, and exhibits strong, long-range repulsion sufficient to stabilize micron-sized colloids in typical physiological environments.[24]

Polymer brushes have been the subject of extensive study, with many reviews of physical and chemical properties.[1,14,20,23] Effective brushes typically maximize the number of polymer repeat units n and graft density σ while minimizing surface heterogeneities. Polymerizing the polymer brush from the graft surface itself, the 'graft-from' strategy, is the most successful method at creating the preferred coating attributes of high surface density, thickness, and low spatial heterogeneity.[12] However graft-from brushes are hard to study and control. Formation is dependent on complex chemical kinetics, and characterization typically requires removal of polymer from the surface to determine basic properties such as the polymer molecular weight and polydispersity.[12,24]

A more common and facile alternative strategy is the 'graft-to' method which forms polymer in the solution and then tethers the polymer to the surface, typically by end

functionalization. While somewhat easier to perform and characterize, graft-to brushes are difficult to form above the polymer overlap concentration (the $\sigma^{-1/2} < R_G$ polymer brush condition).[24] Graft-to brushes thus typically form at low graft densities and with significant lateral heterogeneities, creating layers with poor and spatially-heterogeneous stabilization.

A much less common alternative for the formation of polymer brushes is physical adsorption, in which polymer spontaneously adheres to the surface. Effective physisorbed brushes are typically formed from copolymers with both a poorly soluble monomer chemistry with preference to the adsorbed surface and a well solvated monomer chemistry that extends into the solution.[25] Physisorbed brushes are relatively easy to use, with reliable batch-to-batch performance due to the thermodynamic nature of layer formation. However polymer adsorption is caused by a complex balance of polymer, solution, and surface properties. A-priori design of polymers that form dense and thick layers with minimal desorption during washing is thus difficult.

One common polymer class that forms effective physisorbed brush coatings is the Pluronic™ copolymer series.[26–28] Pluronics™ consist of a hydrophobic poly(propylene oxide) (PPO) block flanked by two poly(ethylene oxide) PEO blocks (PEO-b-PPO-b-PEO), and are commercially available in a series of PEO and PPO molecular weights. Pluronics™ adsorb onto hydrophobic surfaces in aqueous solution with the PPO block oriented with the surface and the PEO block extended into solution.[29] Adsorption density and layer thickness are controlled by the size of the PPO and PEO blocks.[26,30]

Along with the importance of formation strategy, monomer chemistry is another key parameter in determining polymer brush performance. Effective monomer chemistries are typically well solvated and uncharged, which enhances the osmotic repulsion of the

polymer layer while reducing interactions and adhesion to the polymer itself.[1,13,14,24] One historical favorite chemistry for physiological applications is PEO, with extensive usage in the stabilization of biosensors,[3] drug delivery systems,[31–33] and micelles.[34,35] PEO is widely studied, including polymer solution[36–38] and physical properties,[39,40] and the interactions and compression mechanics of PEO brush-modified surfaces.[41–44]

More recently, zwitterionic monomer chemistries have been suggested as alternatives to PEO.[13,45,46] Zwitterionic monomers possess equal amounts of positive and negative charge, typically consisting of a positive quaternary amine with one of either a negative phosphoric acid (phosphorylcholine), sulfopropyl (sulfobetaine), or carboxylic acid (carboxybetaine) group.[13] Like PEO, such materials are highly solvated in aqueous solutions and of a net neutral charge. Zwitterionic polymers overcome some of PEO's chief drawbacks, specifically limited chemical modification routes and chemical degradation in aqueous environments.[3] Some zwitterionic polymers are also sensitive to pH and ionic strength, which has led to the development of 'smart materials' whose properties change in response to changes in solution salt, temperature, or pH.[47–49]

Zwitterionic polymer brushes have also gained attention due to several claims of improved anti-fouling performance relative to PEO, including reduced adsorption of model proteins, reduced cell adhesion, and increased physiological circulation time in systematic administration.[4,16,50–55] Potentially enhanced stabilization properties are commonly explained in the literature as due to a 'super-hydrophilicity' of zwitterionic polymers,[13,56] i.e. increasingly favorable interactions with water relative to the already very hydrophilic PEO. Such 'super-hydrophilic' properties have some support with various molecular-level studies of zwitterionic polymer solution properties, including molecular simulation[45,57] and

spectroscopy.[58] Notably, some applications studies have reported equivalent[3,8,59–61] or reduced[8,62] stabilization for zwitterionic polymer coatings in comparison to PEO polymer coatings. This suggests that there is more to understand regarding the stabilization imparted by a zwitterionic coating than simply segment hydrophilicity.

One possible source of the varied findings for PEO and zwitterionic coating stabilization is variation in coating architectures and layer properties.[61] However, despite the extensive studies of zwitterionic polymer solution properties, fewer studies have studied the mechanisms and properties of zwitterionic polymer coatings. Several studies from the Takahara group, for example, have used neutron reflectometry to explore the impact of monomer chemistry and solution quality on the polymer brush architecture.[63–66] Several studies from the Klein group and others have used mechanical techniques (including the surface force apparatus and atomic force microscopy) to examined the mechanical and hydrodynamic interactions of zwitterionic polymer layers.[67–72] However, these studies have only probed a limited set of polymer architecture and chemistry conditions. Furthermore, the mechanical measurements are typically performed at high polymer compressions and applied forces. This characterization at high applied forces lend insight into lubrication and materials compression. However they are less useful for applications that depend on the onset of polymer, such as stabilization of colloids.[44] It is possible that further insight in the architectures and interactions of zwitterionic polymer coatings may explain their varied performance in antifouling and colloidal stabilization studies.

Importantly, due to the lack of study of surface stabilization and polymer interaction measurements, the current understanding of zwitterionic polymers does not

mechanistically connect the proposed molecular explanations (super-hydrophilicity) to the macromolecular brush-level polymer performance (supposedly improved non-specific surface stabilization). It thus remains unclear if the reported performance aspects of zwitterionic brushes are due to solution properties, monomer-monomer interactions, polymer stiffness, or heterogeneities introduced during polymer brush synthesis and formation. A greater understanding of the mechanisms and performance would empower the current research in surface coating and design, which remain largely empirical and performance-driven.

1.2 Thesis Overview

This thesis presents work using single-particle, kT measurements of colloidal interactions to characterize and understand the mechanical and interaction properties of polymer brush coatings. The thesis first studies the interactions and stability of colloids with adsorbed zwitterionic and PEO brushes. This approach is then applied to characterize the interactions and stability of polymer-coated colloids against model biomaterial surfaces of interest in drug delivery and diagnostic applications. Finally, the effects of NaCl on the interactions and architectures of two zwitterionic chemistries are studied to connect the performance mechanisms of polymers at the molecular and macromolecular-architecture levels.

This dissertation is organized as follows. Chapter 2 describes important theoretical aspects of colloid, surface, and polymer brush interactions. Chapter 3 describes the main experimental methods used in this dissertation. Chapters 4-7 discuss experimental findings, and will be individually published (Chapter 4 is currently under review at Macromolecules). Chapter 4 is a study of the interaction potentials and stability of colloids

with zwitterionic and PEO polymer brushes. Potentials are measured for colloids with a range of PEO and zwitterionic polymer brush thicknesses, and correlated to the colloid's deposition and aggregation behavior. Net interaction potentials closely describe the measured colloidal stability. Characterization of the adsorbed polymer layers shows that the interaction and performance differences between the zwitterionic and PEO brushes are due to greater extension of the zwitterionic brush into solution. The differing polymer chemistries, however, perform similarly when compared by thickness. Chapters 5-6 apply the polymers and insights from Chapter 4 towards several biomaterial systems of interest in the biomaterials community. They again show similar interactions and stability between zwitterionic and neutral polymer coatings when compared across solvated polymer brush thickness. Chapter 7 studies the influence of solution quality on polymer brush interactions and architectures. This uses measurements of polymer layer interactions to decipher mechanisms for the relationship between molecular interactions and macromolecular polymer architectures. Finally, the thesis findings are summarized in Chapter 8, with a discussion of future work to build on the insights of this thesis in Chapter 9.

2 THEORY

2.1 Equilibrium Colloidal Interactions

This thesis primarily utilizes single-particle measurements of colloidal diffusion to infer the interactions causing the measured behavior. The most basic interpretation uses an equilibrium analysis, treating each observation of position in a diffusion trajectory as an independent sampling of an equilibrium distribution. The micron-sized colloids in these measurements are Brownian objects, which sample a distribution of positions at equilibrium governed by the net potential energy of each position. The Boltzman distribution relates a position's sampling probability p and potential energy U,

$$\frac{U_{\mathrm{i}} - U_{\mathrm{M}}}{kT} = \ln\left(\frac{p_{\mathrm{i}}}{p_{\mathrm{M}}}\right) \tag{2.1}$$

where the subscripts i and M represent any given position and the most-probable position, respectively.

The equilibrium potential energy of a micron-sized colloid is governed by body forces that act on the volume of individual colloids, and surface forces that act between the colloid and adjacent colloidal surfaces. The net potential U_{net} of colloid i in a dispersion can be treated using a superposition of potentials,

$$U_{\mathrm{net,i}}(h_{\mathrm{i}}) = U_{\mathrm{G,i}}(h_i) + \sum_{\mathrm{j}} U_{\mathrm{ij}}(r_{\mathrm{ij}}) \tag{2.2}$$

$$U_{\mathrm{ij}}(r_{\mathrm{ij}}) = \sum_{\mathrm{j}} U_{\mathrm{E,ij}}(r_{\mathrm{ij}}) + U_{\mathrm{vdW,ij}}(r_{\mathrm{ij}}) + U_{\mathrm{P,ij}}(r_{\mathrm{ij}}) \tag{2.3}$$

Here U_{net} is dominated by the colloid's gravitational body potential (U_{G}), a function of the net height h; and the sum of pairwise surface potentials (U_{ij}) between colloids and surfaces

i, j, a function of the net surface-surface separation r_{ij}. This thesis focuses on measuring interactions of individual colloids interacting with a planar surface, under conditions where the surfaces forces are dominated by van der Waals (vdW) and polymer (P) contributions.

The gravitational potential for a spherical colloid is given by,

$$U_G(h) = \frac{4}{3}\pi a^3 \left(\rho_i - \rho_f\right) gh \tag{2.4}$$

where a is the colloid radius, g is the gravitational constant, ρ_i-ρ_f is the density difference between the colloid and fluid media, and h is a net colloid height (or surface separation above a plane).

2.1.1 Surface interactions

Electrostatic, van der Waals, and polymer interactions have all been analytically described for interactions between two symmetric flat plates. This description can be corrected to accommodate non-planar geometries using the Derjaguin approximation,[73]

$$U_{\text{eff}}(h) = 2\pi \frac{a_1 a_2}{a_1 + a_2} \int_h^\infty E(l)\, dl \tag{2.5}$$

Here U_{eff} is the effective interaction potential between curved surfaces 1 and 2 with radii of curvature a_1 and a_2, and $E(l)$ is the half-space interaction between flat plates.

The half-space van der Waals interaction is given by,[73]

$$E_{vdW}(l) = \frac{A_{132}(l)}{12\pi l^2} \tag{2.6}$$

in which A_{132} is the separation-dependent Hamaker function between surfaces 1, 2 and the medium 3. A_{132} is rigorously described by Lifshitz theory, which relates a material's optical

and dielectric properties. The materials in this work are well-characterized[74] with the Hamaker function following the form,[75]

$$A_{132}(l) = \frac{1}{2}\left[1+2\kappa l\right]\exp(-2\kappa l)A_0 + A_{1\infty}(l)$$
$$A_{1\infty}(l) = \frac{(a_f + b_f l)}{\left(1+c_f l + d_f l^2\right)} \qquad (2.7)$$

Eq. (2.7) includes the impact of electrostatic screening via the Debye length, κ^{-1}, which were negligible and ignored in all conditions of this work due to high solution ionic strength. Parameters a_f, b_f, c_f, and d_f are constants determined by fit to Lifshitz theory. For most cases this dissertation uses values fit to the dielectric properties of polystyrene and silicon oxide in water, as fit to Lifshitz theory and reported by Bitter and Duncan.[75] For ease of use, the final sphere-plate potential can be reasonably approximated for h/a>0.017 using a power law of the form,[74]

$$U_{vdW}(h) = 2\pi a\int_h^\infty -\frac{A_{132}(l)}{12\pi l^2}dl \cong -A_{eff}ah^{-2} \qquad (2.8)$$

The electric charge on a colloid surface recruits ions from the surrounding media to form an electric 'double layer'. Overlap between the double layers of adjacent surfaces creates an osmotic interaction between the surfaces, with half-space interaction ($E(l)$) given by,

$$E_E(l) = a\frac{B}{\kappa}\exp(-\kappa l) \qquad (2.9)$$

in which B is a constant determined by the material and solution properties. Electrostatic repulsion is the conventional method of stabilizing colloidal dispersions, but is only

effective at low solution ionic strengths (typically below ~1 mM) where κ^{-1}>10 nm. Electrostatic interactions are not suitable for stabilizing colloids in the physiological applications studied in this work, which possess much higher ionic strengths of ~0.15M with k^{-1}<1 nm.

2.1.2 Interactions of polymer brush coatings

As electrostatic interactions cannot stabilize colloidal surfaces in physiological media and ionic strengths, colloids are instead commonly covered with polymer layers to act as a steric barrier preventing foreign molecules from approaching the colloid surface.[24] Under conditions where the polymer's radius of gyration R_G exceeds the mean chain spacing $\sigma^{-1/2}$, lateral interactions between polymer chains cause the polymer to extend into solution. This is the polymer 'brush' regime, and creates a strong osmotic repulsion upon approach to the colloid surface. Layers formed from flexible, uncharged, and well solvated polymers (common properties of the more effective brushes) generally possess a quadratic monomer density profile away from the coated surface. The mechanics of such a polymer brush on a flat surface were first described self-consistently and analytically by Milner, Witten and Cates.[22] Milner's continuum description related the free energy per area f and thickness L of a compressed brush to the uncompressed free energy per area f_0 ($f_0 \leq f$) and thickness L_0 ($L \leq L_0$) as,

$$f(L) = \frac{5}{9} f_0 \left[\frac{L_0}{L} + \left(\frac{L}{L_0} \right)^2 - \frac{1}{5} \left(\frac{L}{L_0} \right)^5 \right] \qquad (2.10)$$

Using Eq. (2.5), the half-space interaction for surfaces with polymer coatings at separation l is given by the polymer potential $f(L)$-$f(L_0)$ for each surface,[76]

$$E(l) = f_1(L) - f_1(L_0) + f_2(L) - f_2(L_0) \tag{2.11}$$

The Derjaguin approximation has been shown to be generally valid for polymer brushes on colloids where $a > 10L_0$.[77–79] For overlapping surfaces with identical polymer coatings (i.e. $f_1(L)=f_2(L)$) and for sphere-plane geometry, the Derjaguin approximation can be solved directly,

$$\begin{aligned} U_{\mathrm{p}} &= 2\pi a \int_{h}^{2L_0} 2\left[f(l/2) - f_0 \right] dl \\ &= \frac{40}{9}\pi a f_0 L_0 \left[\ln\left(\frac{2L_0}{h}\right) + \frac{9}{5}\left(\frac{h}{2L_0}\right) - \frac{1}{3}\left(\frac{h}{2L_0}\right)^3 + \frac{1}{30}\left(\frac{h}{2L_0}\right)^6 - \frac{47}{30} \right] \end{aligned} \tag{2.12}$$

Here L_0 and f_0 are used as continuum parameters to describe the interactions of the polymer brush surface. However Milner also related them to the molecular-scale parameters of graft density σ (chains/area), Kuhn length L_{k}, excluded volume w, and number of Kuhn segments n_{k} ($n_{\mathrm{k}} = n\,b\,/\,L_{\mathrm{k}}$, where b is the monomer spacing)[22,76]

$$f_0 = kT\frac{9}{10}\left(\frac{\pi^2}{12}\right)^{1/3} n_k \left(\sigma^5 w^2 \frac{3}{l_k^{\,2}}\right)^{1/3} \tag{2.13}$$

$$L_0 = \frac{9}{10}\left(\frac{\pi^2}{12}\right)^{1/3} n_{\mathrm{k}} \left(\sigma w \frac{l_{\mathrm{k}}^{\,2}}{3}\right)^{1/3} \tag{2.14}$$

Of these parameters, w and L_{k} are commonly measured solution parameters with only a weak concentration dependence in the semi-flexible concentration regime of polymer brushes. n_k is easily determined for the well-characterized graft-to and physisorbed brushes in our studies when L_k, n, and the monomer chemistry is known. Only σ remains unknown for the majority of systems in this dissertation.

The description of interactions between identical brushes in Eq. (2.12) is inappropriate for many applications, which typically require a colloid to interact with an

exogenous surface of differing surface chemistry. The first step towards describing such interactions between asymmetric polymer layers is to approximate Eq. (2.10) as an exponential decay,[80]

$$f(h) \approx 16\pi a \frac{\Gamma f_0}{\gamma} \exp\left(-\frac{h\gamma}{2L_0}\right) \tag{2.15}$$

which is valid for moderate compressions of $L/L_0 > 0.5$. Γ and γ are constants that describe the decay profile of monomer concentration at the brush periphery, with values of 10.6 and 7.4 respectively for the quadratic concentration profile in Milner's theory.

Two polymer layers, p_1 and p_2, experience an identical compression force under contact. This allows solving for the net separation from the compressed polymer layer thickness L_i of each layer under compression force F,

$$\begin{aligned} F_{p1}\left(L_{p1}\right) &= -F_{p2}\left(L_{p2}\right) \\ L\left(F\right) &= L_{p1} + L_{p2} \end{aligned} \tag{2.16}$$

For sphere-plate geometry, the Derjaguin approximation is then solved for two asymmetric polymer brushes under compression as,[80]

$$U_{p,A}(h) = 8\pi a \Lambda_1^{\lambda_{0,1}/(\lambda_{0,1}+\lambda_{0,2})} \Lambda_2^{\lambda_{0,2}/(\lambda_{0,1}+\lambda_{0,2})} \left(\lambda_{0,1}+\lambda_{0,2}\right) \exp\left(-\frac{h\gamma}{\lambda_{0,1}+\lambda_{0,2}}\right) \tag{2.17}$$

in which $\lambda_i = L_{0,i} / \gamma_i$ and $\Lambda_i = \Gamma_i f_{0,i}$. This approach offers a tractable method for analyzing polymer brush interactions between surfaces of differing chemistries (e.g. 'asymmetric' surfaces).

2.1.3 Error in measured diffusion trajectories

The theory in Ch. 2.1.1-2.1.2 is sufficient to describe the theoretical colloidal potential, and can be used to accurately interpret particle diffusion if measured with perfect resolution. However, each individual position measurements along a diffusion trajectory have an error that distorts the measured profile. The contribution of this point measurement error is accommodated using convolution of noise $g(h, \zeta)$ into the theoretical probability distribution p_T

$$p_c = \int p_T(h)\, g(h-l, \zeta)\, dl \tag{2.18}$$

Here the noise is $g(l)$, with standard deviation, ξ is assumed to be Gaussian. ξ is used within a narrow range of 8-11 nm as estimated from independent characterization. The theoretical potential with measurement error is estimated from p_c using the Boltzman distribution, Eq. (2.1).

2.2 Nonequilibrium Colloidal Dynamics

The theories in the previous section are sufficient for analyzing colloid diffusion to extract interactions and behavior at equilibrium. This section extends that analysis with a non-equilibrium interpretation of diffusion that can infer information on a particle's hydrodynamics.

2.2.1 Langevin dynamics

A colloidal particle in a fluid is acted upon by (1) conservative forces, i.e. the positional derivative of the equilibrium interaction potentials described in section 2.1; (2) a random force due to asymmetric bombardment by surrounding solvent; and (3) a drag

force caused by displacement of solvent during particle movement.[81] Together, this is described using the Langevin equation,[82]

$$m\frac{d^2r}{dt^2} = -\gamma(r)\frac{dr}{dt} + R(t) + \nabla U(r) \tag{2.19}$$

in which m is the object mass, r is the position, γ is a drag coefficient, and R is a random force. The random force and drag are coupled for a system at equilibrium, with mean and covariance typically given by

$$\begin{aligned} &\langle R(t) \rangle = 0 \\ &\langle R(t)R(t') \rangle = q\delta(t-t') \\ &q = 2\gamma kT / m \end{aligned} \tag{2.20}$$

in which δ is the Dirac delta function.

Eq. (2.19) is a stochastic differential equation describing the equation of motion of an individual object over time. For an inviscid system $d^2r/dt^2=0$, and numerical integration over time (e.g. Brownian Dynamics, BD) can generate individual realizations of a colloidal trajectory. When solved for a statistically reliable duration and number of colloids, BD can generate information on the transitions between positions and states, as well as the evolution of probability in a stochastic system.

2.2.2 Smoluchowski dynamics

The Langevin description is a coarse-graining approach that describes the motion of individual stochastic objects over time. An alternative approach is to describe the

evolution of macroscopic characteristics over time. In one dimension, the evolution of probability in a stochastic system is given by the Fokker-Planck (FP) equation,[82]

$$\frac{\partial p(x,t)}{\partial t} = \left[\frac{\partial}{\partial x} D^1(x) + \frac{\partial^2}{\partial^2 x} D^2(x) \right] p \tag{2.21}$$

in which p is probability. D^1 and D^2 are known as the drift and diffusion coefficients, respectively, and capture the position-dependent mean and covariance of probability evolution in the system.

The random and drag forces are coupled for a system at equilibrium (Eq. (2.20), i.e. obeying detailed balance, $\partial p(\mathrm{x})/\partial t=0$). This simplifies Eq. (2.21) to the Smoluchowski equation,

$$\frac{\partial p}{\partial t} = \frac{1}{m\gamma} \left[\frac{\partial}{\partial x} \frac{\partial p(x)}{\partial x} + kT \frac{\partial^2}{\partial x^2} \right] p \tag{2.22}$$

2.2.3 Hydrodynamic colloidal interactions

The diffusivity of a sphere in an unbounded medium is given by the Stokes-Einstein equation,

$$D_0 = \frac{kT}{6\pi\mu a} \tag{2.23}$$

in which μ is the fluid viscosity. A particle near another object experiences drag, which can be represented by a drag coefficient,

$$D = c_d(r_{ij}) D_0 \tag{2.24}$$

Most cases in this work concern the diffusion of a particle adjacent to a flat plane (i.e.

above a glass slide). This problem has been solved exactly,[83] with rational fits to the exact solution of motion parallel (||) and normal (-|) to the wall as,[84]

$$f_{\parallel}(h)=\frac{12420\omega^2+5654\omega+100}{12420\omega^2+12233\omega+431} \tag{2.25}$$

$$f_{\dashv}(h)=\frac{6\omega^2+2\omega}{6\omega^2+9\omega+2} \tag{2.26}$$

in which $\omega=h/a_h$, the height of the colloid above the plane scaled by its hydrodynamic radius.

3 METHODS AND MATERIALS

This thesis uses various polymer and colloidal characterization tools to infer the properties and interactions between colloids, polymers, and biomaterials of interest. This chapter outlines the general experimental tools and procedures used, with detailed discussion of analysis and results in Chapters 4-7.

3.1 Materials

All materials and vendor information are listed in **Table 3.1**. Materials were used as received unless noted otherwise. Deionized water (DI) was obtained from a Milli-Q Nano system.

Table 3.1 Materials used in this study.

name	company	part #
1.6µm SiO2	Bangs Laboratories	SS03
2.3µm SiO2	Bangs Laboratories	SS04N
3.2µm SiO2	Bangs Laboratories	SS05N
4.1µm SiO2	Bangs Laboratories	SS05N
5.2µm SiO2	Bangs Laboratories	SS06N
0.4 µm Sulfate Latex (PS)	Thermofisher Invitrogen	S37491
0.12 µm Sulfate Latex (PS)	Thermofisher Invitrogen	S37204
mPEG NHS	Fisher Scientific	85973
100kDa Hyaluronan	R&D systems	GLR004
1000kDa Hyaluronan	R&D systems	GLR002
20kDa Hyaluronan	R&D systems	GLR001
Bovine serum albumin (BSA)	Sigma-Aldrich	A2058

Porcine-derived mucus	Sigma-Aldrich	M1778
N-(3-dimethylaminopropyl)-*N'*-ethylcarbodiimide hydrochloride (EDC)	Sigma-Aldrich	E6383-5G
N-hydroxysuccinimide (NHS)	Fisher Scientific	AC157270250
(3-aminopropyl)triethoxysilane (APTES)	Sigma-Aldrich	440140-100ML
tetraethyl orthosilicate (TEOS)	Sigma-Aldrich	131903-500ML
Phosphate buffered saline, pH 7.2 (PBS)	Fisher Scientific	20-012-043
NaCl	Sigma-Aldrich	S57653
dihydrogen sodium phosphate	Sigma-Aldrich	S3139
0.22µm cellulose acetate filter	Fisher Scientific	F7648-50EA
Sulfuric acid	Fisher Scientific	AC30207-0026
2,2,2-trifluoroethanol	Fisher Scientific	AAA107880B
nitrogen	Airgas	CGA-580
SiO_2 slides	Fisher Scientific	12-549-3
coverslips (VWR)	Fisher Scientific	21299
5mm viton o-ring	McMaster	9263k285
10mm viton o-ring	McMaster	9263K286
vacuum grease	Fisher Scientific	14-635-5D
Folded Capillary Zeta Cell	Malvern	DTS1070

3.1.1 Colloids

Silica (SiO_2) colloids of between 1.6-5.2µm nominal diameters were purchased from Bangs labs. SiO_2 colloids of between 50-1000nm diameter were synthesized using

the well-known Stober synthesis. Briefly, deionized water, methanol, ammonia, and tetraethyl orthosilicate (TEOS) were combined in ratios following published guidelines to synthesize particles of a given size.[85] The mixture was allowed to react for at least 4 hours, and purified by at least 5 cycles of centrifugation, removal of the supernatant, re-dispersion in ethanol, and storage at 4°C.

SiO_2 colloids were rendered hydrophobic via reaction with 1-octadecanol. Colloids were dispersed in DI (typically 1mL of 0.01-1% v/v). Particles were purified by 5 cycles of centrifugation and re-dispersion in DI, and at least 8 cycles of centrifugation and re-dispersion in 200 proof ethanol. The purified particles were transferred to a round-bottom flask with 50mL ethanol and 1 pellet of octadecanol (approximately 20mg). The flask was purged with N_2, and the mixture was heated to 80°C in an oil bath. Following dissolution of octadecanol and subsequent evaporation of the ethanol, the mixture was further heated to between 120-150°C and maintained for 3-4 hours. Particles were recovered in ethanol, with subsequent purification by (1) 5 cycles of (i) bath sonication and (ii) centrifugation and re-dispersion in chloroform, and (2) 8 cycles of (i) bath sonication and (ii) centrifugation and re-dispersion in ethanol. Particles typically displayed a slight polydispersity increase via DLS, from PDI ~0.05 before the reaction to PDI ~0.15 after the reaction. Care was taken to prevent fluid cavitation during the initial reaction stage, which dispersed particles to poorly heated areas of the vial and significantly decreased the coating quality.

Octadecanol-coated silica were unsuitable for dynamic light scattering due to the increase in PDI during the octadecanol reaction. Sulfopropyl-functionalized polystyrene latex of 100-400 nm diameter were instead used as monodisperse hydrophobic colloids.

Polystyrene particles were stored in ethanol, and transferred to DI before usage using centrifugation.

3.1.2 Glass slides

Glass slides were cleaned by sequential bath sonication (30 min each) in isopropyl alcohol, acetone, rinsed in DI, and soaked in NoCHromix for at least 1 hr. Slides were rinsed in DI and dried with N_2. To render hydrophobic, dried slides were spin coated with 3% w/w polystyrene in toluene at 3k RPM for 1 minute.

To present NH_2 for subsequent functionalization, dried slides or silica in ethanol were added to 2% v/v (3-Aminopropyl)triethoxysilane (APTES) in toluene at room temperature. After 16 hours, slides were sequentially rinsed with toluene, isopropyl alcohol, DI, dried with N_2, and baked at 80°C for 1 hour. Following the reaction, NH_2-presenting silica colloids were sonicated, centrifuged, and re-dispersed in ethanol 5 times. NH_2-coated colloids and slides were stored in EtOH for no more than 12 hours before usage due to limited chemical stability of the NH_2 group.

Slides were functionalized with 5mm ID Viton o-rings to make batch-cells to contain colloid dispersions for optical microscopy experiments. Liquid was added to the batch cells, which were then sealed with vacuum grease and coverslips prior to microscopy experiments.

3.1.3 Surface coatings on slides and colloids

Amphiphilic copolymers, porcine mucus, and bovine serum albumin (BSA) coatings were formed via adsorption onto hydrophobic colloids or glass slides. Polymer, mucus, and BSA were dissolved at 1 mg/mL. Mucus and BSA solutions were filtered

through a 0.22μm cellulose acetate filter to reduce bioburden (for BSA and mucus) and insoluble impurities (for mucus). Colloids were then added to the adsorbate solution, mixed with an orbital shaker for at least 2 hours, and purified using at least 5 cycles of centrifugation and re-dispersion in the solution of interest. For slides, adsorbate solution was added to batch cells in a humidified, protected container for at least 2 hours. After adsorption, the adsorbate was rinsed with at least 5 washes with the measurement solution of interest.

Hyaluronan coatings were formed by chemisorption and cross-linking using carbodiimide coupling. 100 kDa hyaluronan was dissolved at 10 mg/mL in 150 mM NaCl, 2 mM Hepes, pH 5.5, and filtered through a 0.22um filter. N-hydroxysuccinimide (NHS), and 1-(3-Dimethylaminopropyl)-3-ethylcarbodiimide (EDC) were quickly added to the hyaluronan solution to a final concentration of 0.05M EDC, 0.05M NHS, and 4 mg/mL hyaluronan. The mixture was quickly added to prepared batch cells on NH_2 presenting slides, or to dried NH_2-presenting colloids. The reaction was terminated after 4 hours, with washing of colloids or slides with the solution of interest for measurements.

3.1.4 Polymers

PEO-b-PPO-b-PEO Pluronic™ polymers were generously donated by BASF, and herein referred to as PEO copolymers. PEO copolymers were obtained with various molecular weight variants of the PEO and PPO blocks, which influence the adsorption and architectural properties of the polymers when adsorbed onto a hydrophobic surface. PEO copolymers have a well-documented history of usage as antifoaming, micellization, and stabilizing agents. Their relevant literature and characterization information for this thesis is given in **Table 3.2**.

Table 3.2 Properties of PEO-b-PPO-b-PEO polymers, generously donated by BASF Corporation

Polymer	M_w/M_n	σ (nm^{-2})[c]	R_G PEO (nm)
PEO_{141}-*b*-PPO_{51}-*b*-PEO_{141}	1.2[a]	0.12[a], 0.18[b]	4.3
PEO_{111}-b-PPO_{47}-b-PEO_{111}	1.1[a]	0.12[a]	3.9
PEO_{103}-b-PPO_{39}-b-PEO_{103}	1.1[a]	0.11[a]	3.7
PEO_{100}-b-PPO_{65}-b-PEO_{100}			
PEO_{76}-b-PPO_{29}-b-PEO_{76}	1.1[a]	0.13[a]	2.8
PEO_{62}-b-PPO_{40}-b-PEO_{62}	1.1[a]	0.17[a]	2.8
PEO_{37}-b-PPO_{56}-b-PEO_{37}		0.19[a], 0.24[b]	2.2
PEO_{27}-b-PPO_{61}-b-PEO_{27}		0.3[a]	2.1
PEO_{26}-b-PPO_{40}-b-PEO_{26}	1.2[a]	0.23[a]	
PEO_{17}-b-PPO_{60}-b-PEO_{17}			

a. Shar et al.
b. Brandani et al.
c. Adsorption density of copolymer onto a hydrophobic surface (copolymer chains / nm^2)

PMPC-b-PPO-b-PMPC and PMAPS-b-PPO-b-PMAPS (herein referred to as PMPC or PMAPS copolymer) variants of the PEO copolymers were synthesized by collaborators in the M. Herrera-Alonso lab. The synthesis procedure used activator regenerated by electron transfer-atom transfer radical polymerization (ARGET-ATRP) to polymerize MPC or MAPS monomer onto a Br-PPO_{49}-Br macroinitiator. Following polymerization, polymer was purified using precipitation of the copolymer, dialysis in DI, and lyophilization.

For PMPC copolymers, NMR was used to determine the number-averaged degree of polymerization (n), and generally agreed to within 5% of the gravimetrically determined yield. For PMAPS, yield only was used to determine the number-averaged degree of

polymerization due to NMR signal overlap between important PMAPS peaks and the NMR solvent. Static light scattering was used to determine the weight-averaged degree of polymerization (n_w) for both PMPC and PMAPS copolymers. The relevant characterization information of PMPC and PMAPS copolymers are listed in **Table 3.3**.

Table 3.3. Properties of PMPC and PMAPS copolymers.

polymer	referred to as	M_n[a]/kDa	M_n/M_w	A_2 / (mol mL g^{-2})[b]
$PMPC_{80}$-b-PPO_{49}-b-$PMPC_{80}$	$PMPC_{80}$	40.1	1.3	1.0×10^{-2}
$PMPC_{73}$-b-PPO_{49}-b-$PMPC_{73}$	$PMPC_{73}$	36.8	1.1	1.2×10^{-2}
$PMPC_{57}$-b-PPO_{49}-b-$PMPC_{57}$	$PMPC_{57}$	29.3	1.4	5.0×10^{-4}
$PMPC_{28}$-b-PPO_{49}-b-$PMPC_{28}$	$PMPC_{28}$	15.8	1.08	1.1×10^{-2}
$PMPC_{10}$-b-PPO_{49}-b-$PMPC_{10}$	$PMPC_{10}$	7.5		
$PMAPS_{90}$-b-PPO_{49}-b-$PMAPS_{90}$	$PMAPS_{90}$	60.2	1.3	
$PMAPS_{51}$-b-PPO_{49}-b-$PMAPS_{51}$	$PMAPS_{51}$	35.3		
$PMAPS_{29}$-b-PPO_{49}-b-$PMAPS_{29}$	$PMAPS_{29}$	21.3	1.4	

[a] 1H NMR (methanol-d4)
[b] SLS (TFE)
[c] M_w(SLS)/M_n(1H NMR)

In detail, Br-PPO-Br macroinitiator was prepared by dissolving PPO_{49} ($M_n \sim 2700$ g/mol, Sigma) in anhydrous toluene and distillation at 90 °C and 100 mTorr for 1 h to remove residual water. The flask was submerged in an ice bath with 4 molar equivalents of trimethylamine (TEA), followed by dropwise addition of 4 molar equivalents of 2-bromoisobutyryl bromide (BIBB). The reaction was run for 24 h at 20 °C, after which time the mixture was filtered to remove the insoluble hydrobromide salts. After filtration, the reaction mixture was stirred with activated carbon, filtered again and dried under vacuum. The crude product was mixed with pH 9 water (300 mL) and extracted several times with

dichloromethane (DCM). The organic layer was further backwashed with 0.5 M sodium bicarbonate, brine (5 M NaCl) and water, and then dried with $MgSO_4$ to remove traces of water. The organic mixture was then filtered to remove $MgSO_4$ and dried under vacuum. The degree of esterification was calculated to be 100% based on the disappearance of the hydroxyl peak at 4.41 ppm.

In detail, MPC and MAPS were polymerized onto the Br-PPO-Br macroinitiator by ARGET-ATRP. For this, PPO_{49} macroinitiator (Br-PPO_{49}-Br) (50 mg, 0.016 mmol) and MPC (953 mg, 3.23 mmol, 100 mol eq. to -Br) were dissolved in methanol (3 mL). Tris(2-pyridylmethyl)amine (TPMA) ligand and ascorbic Acid (reducing agent) were also prepared in methanol at 10 mg/mL each. Aliquots of the TPMA solution (187 µL, 6.5 µmol, 10 mol eq. to Cu) and ascorbic acid solutions (114 µL, 6.5 µmol, 10 mol eq. to Cu) were added to the flask that contained the macroinitiator and monomer, sealed, and bubbled with argon for 40 min at room temperature. Separately, a stock solution of $CuBr_2$ catalyst was prepared in methanol at 2 mg/mL and bubbled under nitrogen for 30 min. The flask containing macroinitiator, MPC, TMPA and ascorbic acid was immersed in an oil bath set at 40 °C and the reagents were allowed to homogenize under vigorous argon flow for ~2 min. Polymerization was started by the addition of $CuBr_2$ solution (72 µL, 0.65 µmol, 200 ppm relative to MPC) via a degassed gastight syringe. Polymerization was carried out at 40 °C for 18 hour and stopped by immersing the flask in an ice bath and opening it to atmosphere. The product was purified by dialysis against first methanol and then against nanopure water and recovered by lyophilization.

3.2 Characterization Methods

3.2.1 Total internal reflection microscopy

Total internal reflection microscopy (TIRM) recorded the diffusion of micron-sized colloids across planar surfaces. Videos were collected using an optical microscope (Axioplan 2, Zeiss) equipped with a 40× optical objective (LD Plan-NEOFLUAR) and a charge coupled device (CCD) camera (ORCA-ER, Hamamatsu). Images were recorded at 4 binning and 30 ms recording rate. Samples were illuminated by using a 633 nm HeNe laser (Melles Griot) to excite an evanescent wave onto a 68° dovetail prism optically coupled to a glass slide. The evanescent wave was excited at the interface between the glass slide and liquid in batch cell, scattering light off of colloids near the slide-liquid interface. A schematic of the TIRM setup is given in **Fig. 3.1**.

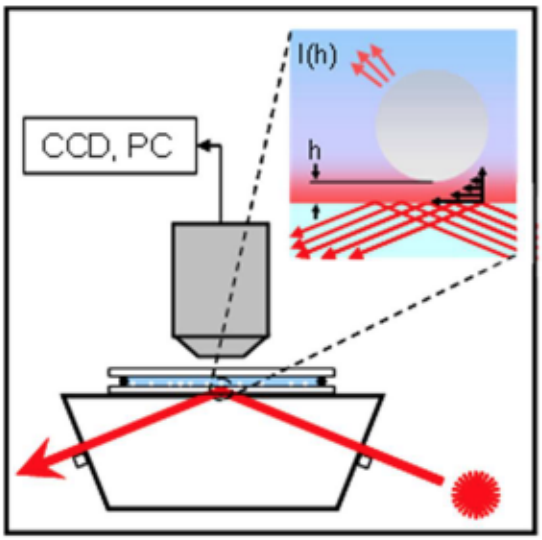

Fig. 3.1 Schematic of TIRM setup. An evanescent wave is excited along the liquid-solid interface of a slide optically coupled to a dove-tail prism. Colloids in the liquid scatter light with intensity *I* dependent on their separation *h* from the solid-liquid interface.

The separation h between each colloid and the slide was determined from the colloid's scattering intensity I with ~1 nm resolution using,

$$I(h) = I_0 \exp\left(-\beta^{-1} h(t)\right) \tag{3.1}$$

where I_0 is the scattering intensity at colloid-slide contact (at $h = 0$), and β is the evanescent wave decay length. Values of β for solutions of 0.01-3M [NaCl] are reported in **Table 3.4**.

Table 3.4. Dependence of the evanescent wave decay length on [NaCl] in TIRM experiments

β / nm	112.9	113.67	125.99	126.19
[NaCl] / M	0.01	0.15	1	3

TIRM measurements recorded videos of between 5-15 min duration. For measurements of colloidal interactions, ensemble-average interactions were typically composed of at least 10-20 particles. Interaction potentials of individual colloids were determined using the Boltzman relation (Eq. (2.1)). Stability against deposition was determined through analysis of colloidal deposition, with a detailed discussion in Chapter 5.

3.2.2 Dynamic light scattering

Dynamic light scattering (DLS) was used to measure the size and polydispersity of dispersions of polymers and colloid. DLS was conducted on a Malvern Instruments Nano-ZS ZetaSizer equipped with a 4 mW He-Ne laser operating at 633 nm. All measurements were performed at 25 °C at a scattering angle of 173°. The mean and standard deviation in hydrodynamic diameter (d_h, σ_h respectively) of measured dispersions were determined using the method of cumulants, and only used quantitatively when polydispersity index was below 0.1 (PDI = d_h^2 / σ_h^2).

Hydrodynamic thickness L_h of adsorbed polymers or biomaterials was inferred by DLS. Polymers or biomaterials were adsorbed onto 100nm PS in DI. The coating hydrodynamic thickness was then estimated from measurements of bare and coated polystyrene particles using $L_h = (d_{h,coated}-d_{h,bare})/2$.

DLS was also used to assess the stability of particles with various coatings and in various solution conditions. Polymers were adsorbed onto 100 nm and 400 nm PS latex particles at a high colloid concentration (typically 0.01-0.1% v/v). The polymer-coated colloids were then rapidly diluted into the measurement solution of interest, and measured by DLS at specific time intervals over at least 24 hours. Aggregation of colloids was inferred by an increase in the size and polydispersity of dispersions.

3.2.3 Quartz crystal microbalance with dissipation

Quartz crystal microbalance with dissipation (QCM-D) was used to estimate the thickness and viscoelastic properties of an adsorbed polymer thin-film. QCM-D measurements used a QSense instrument equipped with SiO_2 sensors with a 5 mHz fundamental (Biolin Scientific). Sensors were cleaned through sonication in a series of solvents (toluene, isopropanol, acetone, and finally deionized water), dried under N_2, exposed to oxygen plasma for 5 min, and spin-coated with 1% w/w polystyrene (M_w=192kDa) in toluene at 3k rpm for 1 min. During use, sensors were equilibrated with deionized water for ~2 h, contacted with 1 mg/mL polymer solution for a minimum of 1 h (or until equilibration), and washed with deionized water (DI) for a minimum of 1 h. Frequency and dissipation data were interpreted using a Kelvin-Voigt viscoelastic model of the polymer layer as implemented in the QSense software and previously reported.[86]

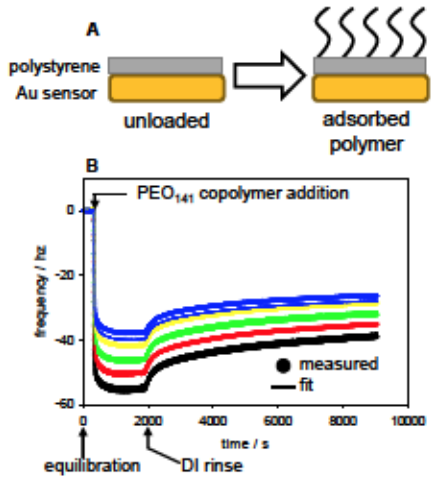

Fig. 3.2. Overview of Quartz Crystal Microbalance with Dissipation. (**A**) Measurement of polymer adsorption onto polystyrene-coated Au sensors. (**B**) Frequency change of Au sensor caused by polymer adsorption. Sequential steps of equilibration with DI, addition of 1mg/mL PEO_{141} in DI, and rinsing with DI. Measured (circle) and fit (lines) with an extended Voigt viscoelastic model. 3rd, 5th, 7th, 9th, 11th sensor overtones are blue, yellow, green, red, and black respectively. 2 hours of equilibration in DI prior to the experiment are not shown.

3.2.4 Nuclear magnetic resonance

Hydrogen nuclear magnetic resonance (^{1}H NMR) spectra were recorded on a Bruker AV 400 MHz spectrometer in either DMSO-d_6 or methanol-d_4. Spectra were referenced to DMSO (2.50 ppm) or CD_3OD (3.31 ppm). Example NMR spectra for the Br-PPO-Br macroinitiator and PMPC-b-PPO-b-PMPC copolymer are given in **Fig. 3.3**.

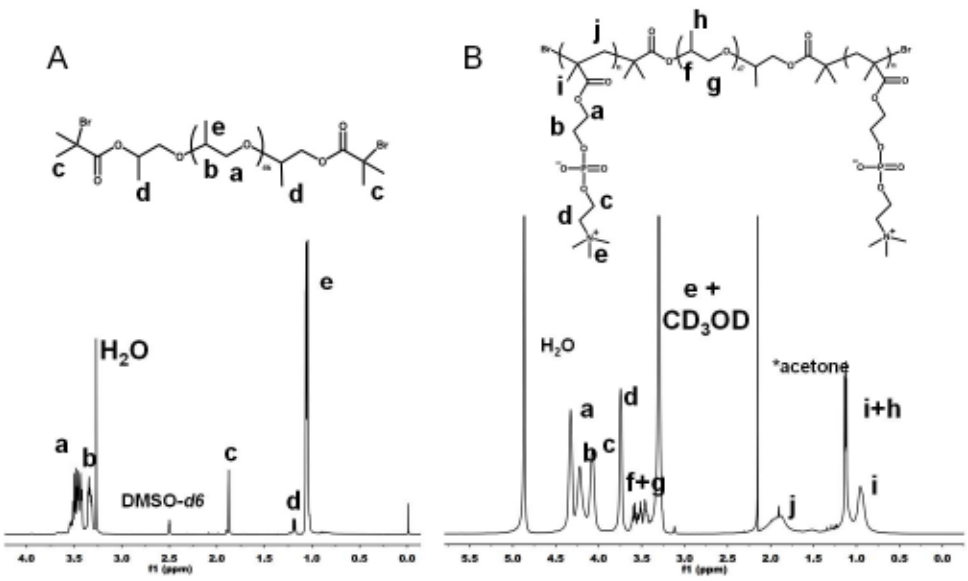

Fig. 3.3. Example ^{1}H NMR characterization of PMPC-*b*-PPO-*b*-PMPC copolymers. (**A**) Spectrum and peak assignments of PPO_{49} functionalized with 2-bromoisobutyryl bromide. (**B**) Spectrum and peak assignments of $PMPC_{57}$-*b*-PPO_{49}-*b*-$PMPC_{57}$ copolymer after purification to remove unreacted MPC monomer.

3.2.5 Static light scattering

Static light scattering (SLS) was performed by collaborators in the M. Herrera-Alonso lab, and used to measure the weight-averaged molecular weight (M_w) of polymer solutions. Copolymers were dissolved in trifluoroethanol (a good solvent for PPO, PMPC, and PMAPS blocks) at concentrations between 0.05 to 2.5 mg/mL and filtered through 0.45 μm PVDF syringe filters (Genesee Scientific). Polymer solutions were injected with a syringe pump (New Era Pump System, NE-1000) at 0.2 mL/min and 25 °C. Methoxypolyethylene glycol (5 kDa, Sigma-Aldrich; 5 mg/mL solution in trifluoroethanol) was used as a normalization standard, with R_G set to 2 nm. dn/dc values were used to determine polymer absolute molecular weight. dn/dc was measured for each polymer using an Optilab-rEX refractive index detector (Wyatt Technology) at a wavelength of 658 nm, and analyzed using Astra 6.1 software.

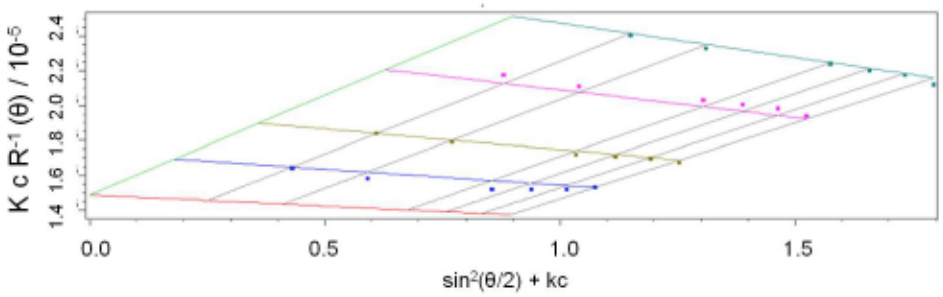

Fig. 3.4. Example static light scattering measurement of $PMPC_{57}$-*b*-PPO_{49}-*b*-$PMPC_{57}$ polymers in trifluoroethanol. Characterization information is reported in **Table 3.3**

3.2.6 Critical micelle concentration

Critical micelle concentration (C_{cmc}) of the triblock copolymers were measured by collaborators in the M. Herrera-Alonso lab. C_{cmc} was determined using the pyrene assay, using fluorescence spectroscopy. For each sample, 50 µL of pyrene solution (6.0×10^{-5}M in acetone) was added to a 5 mL scintillation vial and the solvent was allowed to evaporate completely. After 1 hour of evaporation, 50 µL of polymer solution of known concentration (0.001 – 50 mg/mL in MeOH) was added to each vial containing pyrene, immediately followed by the addition of 1 mL of DI. The samples were vigorously stirred with a vortex mixer for 1 min and left uncovered overnight to allow for complete evaporation of methanol. The final concentration of polymer ranged from 0.05 µg/mL to 2.5 mg/mL. Pyrene concentration in each sample was kept constant at 3.0×10^{-6} M. Pyrene excitation was recorded from 300 to 360 nm with the bandwidth set at 2 nm. The intensity ratio from signals at 336 nm and 334 nm (I_{336}/I_{334}) were plotted against polymer concentration. C_{cmc} values were read from the intersection between curve tangents at low and high concentrations. An example of C_{cmc} determination is shown in **Fig. 3.5**.

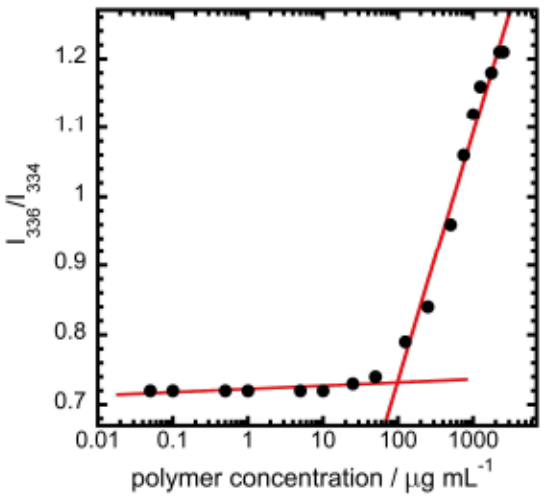

Fig. 3.5 Example determination of C_{cmc} for PMPC and PMAPS copolymers. Fluorescence response curve for the pyrene assay of the $PMPC_{57}$ copolymer.

4 INTERACTIONS AND ARCHITECTURES OF ADSORBED ETHYLENE-OXIDE AND PHOSPHORYLCHOLINE POLYMERS

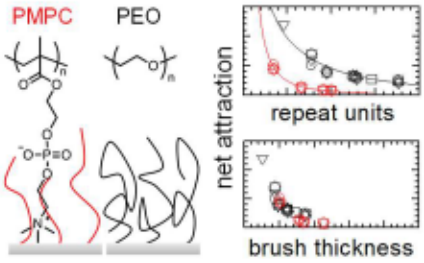

4.1 Introduction

Prevention of particle aggregation and deposition in physiological media is critical to applications involving biosensors,[61,87] drug delivery,[88,89] and filtration.[90] Addition of a solvated polymer coating to colloidal particles and surfaces is a common strategy to stabilize colloids against aggregation and prevent their deposition onto surfaces. Polymer layers that are effective at stabilizing colloidal particles against aggregation and deposition must generate repulsion of sufficient range and magnitude to overcome attractive interactions.[1,20,23,91] The range and magnitude of repulsion is enhanced for layers with "polymer brush" architectures, where lateral crowding causes chains to extend away from surfaces.[1,20] Polymer chemistries that have been found to be most favorable for generating repulsion are often well solvated and uncharged, presumably to minimize attractive segment interactions.[1,20,92] Poly(ethylene oxide) (PEO) satisfies many of the cited physical and chemical constraints and is widely considered as the benchmark for colloidal stabilization in physiological ionic strength aqueous media.[32,88,93,94]

Zwitterionic polymer chemistries have gained attention as potential alternatives to PEO.[13,45] Zwitterionic polymers are composed of a hydrocarbon backbone with

zwitterionic moieties, which consist of positive and negative functional groups with a net neutral charge and significant dipole moments. Several studies have demonstrated zwitterionic polymer surface layers to reduce adhesion of proteins[95] and cells,[61] increase colloidal stability,[96] and increase drug circulation time.[54] Apparently enhanced antifouling of zwitterionic polymer coatings is often attributed to "super-hydrophilicity" of zwitterionic polymers[13,45] (*i.e.*, highly favorable water-monomer interactions; inferred from simulations[45,97] and spectroscopy[58]). However, several conflicting studies have reported either equivalent[3,8,59–61] or inferior[8,62] antifouling behavior or colloidal stabilization by zwitterionic polymers relative to PEO. This suggests there is more to understand in the net interactions of zwitterionic and PEO copolymers than simply segment "hydrophilicity."

Varied findings in comparative studies of zwitterionic and EO polymers may partly arise from limitations on controlling or characterizing layer architectures. Many studies investigate either "graft-to" layers, which often produce lower surface concentrations, or "graft-from" layers, which are more difficult to characterize (since chains must be removed for analysis).[12,20,98] Another strategy is to use physisorbed copolymers, which are straightforward to process and characterize prior to adsorption. First-principles design of copolymer compositions and architectures is not trivial based on a complex balance of segment, solvent, and surface interactions. However, copolymers capable of forming thick, dense layers via physisorption have been identified.[42,99] A notable example is PEO-b-PPO-b-PEO triblock copolymers, which are well established for stabilizing hydrophobic colloids in aqueous media.[26,29,99] While a number of studies have investigated zwitterionic copolymer phase behavior and as emulsion stabilizers,[100–103] fewer have explored their use

as colloidal stabilizers.[52,104] Many studies have focused on synthesis of novel polymers to reduce protein adsorption, but none have systematically studied connections between layer properties, interactions, or their effects on colloidal aggregation and deposition.

Although the interactions of polymer coatings determine all of their behaviors and properties, a limited number of studies have directly measured or modeled such interactions.[67,68,105,106] Several studies have measured polymer layers interactions, typically at high applied normal forces that produce significant compression. High normal forces and layer deformation are important to adhesion, friction, and lubrication between adsorbed layers, but are less relevant to colloidal stability. Colloidal stability is determined by the net balance of competing colloidal interactions at the very onset of repulsion between adsorbed layers.[44,107] In particular, colloidal stabilization is highly sensitive to kT-scale repulsion between adsorbed polymer layers for weak interpenetration and compression of adsorbed layers at the periphery of the adsorbed layer architecture where their density profile vanishes.[23,44] The authors are unaware of measurements of zwitterionic copolymer interactions in the regimes relevant to colloidal stability, as well as any systematic studies of how block chemistries, molecular weights, and adsorbed layer architectures are related to interactions critical to colloidal stability.

This chapter reports measured interactions between PEO and zwitterionic copolymers adsorbed to hydrophobic colloids and surfaces. Measurements are reported for commercial PEO-b-PPO-b-PEO copolymers as well as novel zwitterionic copolymers of PMPC-b-PPO-b-PMPC (**Fig. 4.1**). Ensemble total internal reflection microscopy (TIRM)[108] is used to measure potential energy profiles with kT and nanometer scale resolution between adsorbed triblock copolymer layers with varying molecular weights of

the PEO and PMPC end blocks. Additional characterization of adsorbed layers by dynamic light scattering and quartz-crystal microbalance in conjunction with theoretical models is used to compare and contrast PEO and PMPC copolymer layer properties, architecture, and interactions. Finally, measured interactions are connected to colloidal stability against deposition and aggregation for a range of colloid diameters and copolymer molecular weights. Findings show important differences in PEO and PMPC copolymer interactions and architectures that determine colloidal stability in physiological media.

4.2 Theory

Ensemble TIRM was used to monitor the motion of spherical colloidal particles above a glass microscope slide. This allowed direct determination of the colloid's relative height distribution, $p(h)$, and calculation of the potential energy profile, $U(h)$, using the Boltzmann relation,

$$\frac{U(h)-U_{\mathrm{M}}(h_{\mathrm{M}})}{\mathrm{k}T}=\ln\left(\frac{p_{\mathrm{i}}}{p_{\mathrm{M}}}\right) \tag{4.1}$$

in which "i" and "M" are indexes for any height bin and the most probable height bin respectively, k is Boltzmann's constant, and T is absolute temperature. Net colloidal potential energy profiles were modeled as a function of height h above the planar surface as a superposition of gravitational (G), van der Waals (vdW), and polymer compression (P) potentials,

$$U(h)=U_{\mathrm{G}}(h)+U_{\mathrm{vdW}}(h)+U_{\mathrm{P}}(h) \tag{4.2}$$

Electrostatic interactions were ignored as insignificant due to the high solution ionic strength (150mM) media and low colloid surface charge (1±4mV). The gravitational potential energy is given by,

$$U_G(h) = \frac{4}{3}\pi a^3 \left(\rho_p - \rho_f\right) g h \tag{4.3}$$

in which a is particle radius, ρ_p-ρ_f is the difference in particle and fluid densities, and g is the gravitational constant. The gravitational contribution to the net interactions was used to fit the colloid radius, and since it is a body force with simple linear dependence, it was then subtracted to leave only colloidal-surface interactions (*i.e.*, van der Waals, polymer). The van der Waals and polymer contributions to the net colloidal interaction were both modeled using interactions between flat plates in the Derjaguin approximation to obtain sphere-plate potentials as,

$$U(h) = 2\pi a \int_h^\infty E(l)dl \tag{4.4}$$

in which $E(l)$ the energy per unit area between flat plates at a separation, l, for the interaction of interest. For van der Waals, the interaction between flat plates is given by,

$$E(l) = \frac{A_{132}(l)}{12\pi l^2} \tag{4.5}$$

where A_{132} is the separation-dependent Hamaker function between surfaces of materials 1 and 2 separated by a medium of material 3, which can be computed using the Lifshitz theory and accurately represented for the materials in this work by,[75]

$$A_{132}(l) = \frac{1}{2}\left[1+2\kappa l\right]\exp(-2\kappa l)A_0 + A_{1\infty}(l)$$
$$A_{1\infty}(l) = \frac{(a_f + b_f l)}{\left(1+c_f l + d_f l^2\right)} \tag{4.6}$$

This form includes the impact of electrostatic screening via the Debye length, $\kappa^{-1} = 0.8$ nm, for all conditions. For ease of use, the final sphere-plate potential can be reasonably approximated for $h/a>0.017$ as a power law of the form,[108]

$$U_{vdW}(h) = 2\pi a\int_h^\infty -\frac{A_{132}(l)}{12\pi l^2}dl \cong -Aah^{-2} \tag{4.7}$$

For compression of polymer layers adsorbed to two flat plates, the energy per area can be represented as[76]

$$E(l) = f_1(l/2) - f_1(L_0) + f_2(l/2) - f_2(L_0) = 2\left[f(l/2) - f_0\right] \tag{4.8}$$

in which $f(L)$ is the free energy per area of the polymer layer at compressed thickness L, L_0 is the uncompressed polymer layer thickness, and subscripts 1 and 2 refer to the polymers brushes on surfaces 1 and 2. The free energy of a well solvated, flexible polymer brush layer under compression is given by Milner as,[22]

$$f(L) = \frac{5}{9}f_0\left[\frac{L_0}{L} + \left(\frac{L}{L_0}\right)^2 - \frac{1}{5}\left(\frac{L}{L_0}\right)^5\right] \tag{4.9}$$

where f_0 and L_0 are given by,

$$f_0 = kT\frac{9}{10}\left(\frac{\pi^2}{12}\right)^{1/3} n_k\left(\sigma^5 w^2 \frac{3}{L_k^2}\right)^{1/3} \tag{4.10}$$

$$L_0 = \left(1+\sqrt{M_w/M_n - 1}\right)\frac{9}{10}\left(\frac{\pi^2}{12}\right)^{1/3} n_k\left(\sigma w\frac{L_k^2}{3}\right)^{1/3} \tag{4.11}$$

Here ω is excluded volume, σ is polymer surface coverage, L_k is the polymer's Kuhn length, and n_k is the number of Kuhn segments ($n_k = nL_m/L_k$ where L_m the segments chain spacing). Inserting the interaction between flat plates into the Derjaguin approximation yields the sphere-wall potential as,

$$\begin{aligned} U_p &= 2\pi a \int_h^{2L_0} 2\left[f(l/2) - f_0 \right] dl \\ &= \frac{40}{9}\pi a f_0 L_0 \left[\ln\left(\frac{2L_0}{h}\right) + \frac{9}{5}\left(\frac{h}{2L_0}\right) - \frac{1}{3}\left(\frac{h}{2L_0}\right)^3 + \frac{1}{30}\left(\frac{h}{2L_0}\right)^6 - \frac{47}{30} \right] \end{aligned} \quad (4.12)$$

For ease of use, the final sphere-plate potential can be reasonably approximated for moderate compression ($L > 0.5L_0$) as an exponential of the form,[80]

$$U_p(h) \cong 4\pi a \frac{\alpha}{\beta} f_0 L_0 \exp\left(\frac{-\beta h}{2L_0}\right) \quad (4.13)$$

where the constants α, β are 21.2 and 7.38 respectively (i.e. by fitting Eq. (4.13) to Eq. (4.12)).

Constants and parameters used in the calculations of Eq. (4.2) - (4.13) are reported in **Table 4.1** and **Table 4.2**.

Table 4.1 Parameters used in polymer modeling and calculations. (a) estimated from R_G measurements in Kalasin et al[52]

name	parameter (units)	PEO	PMPC	used in Eq.
Kuhn length	L_k (nm)	0.72[39]	4[109]-10[a]	(4.10), (4.11)
monomer molecular weight	M_m (g/mol)	44.1	295.3	
excluded volume	w (nm3)	0.49[36]		(4.10), (4.11)

Table 4.2 Constants used in the modeling and calculations of colloidal potential energy interactions

parameter (units)	value	equation
a_f (kT)	1.962	(4.6)
b_f (kT nm^{-1})	0.0281	(4.6)
c_f (nm^{-1})	0.0593	(4.6)
d_f (nm^{-1})	0.0033	(4.6)
k (nm^{-1})	1.25	(4.6)
A_0 (kT)	1.501	(4.6)
ρ_p (g/cm^3)	1.96	(4.3)
ρ_f (g/cm^3)	1	(4.3)
T (K)	295	(4.1), (4.10)
A (kT nm)	1488	(4.7)

4.3 Experimental

This section describes the specific methods used in the measurement and analysis of information in this Chapter 4. Further details are available in Chapter 3.

4.3.1 Polymers

PEO-b-PPO-b-PEO copolymers were generously donated by BASF. Polymer synthesis was performed by collaborators in the M. Herrera-Alonso lab. PMPC-b-PPO-b-PMPC copolymers were synthesized by polymerization of MPC monomer onto Br-PPO_{49}-Br using activator regenerated by electron transfer-atom transfer radical polymerization (ARGET-ATRP). Polymers were purified by crystallization and subsequent dialysis in DI. Purified polymer was characterized using NMR and SLS for M_n and M_w respectively. **Table 4.3** summarizes the properties of polymers used in this study.

Table 4.3 Characterization information for PMPC copolymers. Notes: (a) [a] ^{1}H NMR (methanol-d_4), (b) SLS (TFE), (c) M_w(SLS)/M_n(^{1}H NMR).

Polymer	M_n[a] (g/mol)	M_w[b] (g/mol)	M_n/M_w[c]	A_2 (mol mL g^{-2})[b]
$PMPC_{80}$-b-PPO_{49}-b-$PMPC_{80}$	50300	67200	1.33	1.1×10^{-2}
$PMPC_{73}$-b-PPO_{49}-b-$PMPC_{73}$	46200	52300	1.13	1.2×10^{-2}
$PMPC_{57}$-b-PPO_{49}-b-$PMPC_{57}$	36800	50200	1.37	5.0×10^{-4}
$PMPC_{28}$-b-PPO_{49}-b-$PMPC_{28}$	19600	21300	1.08	1.1×10^{-2}
$PMPC_{10}$-b-PPO_{49}-b-$PMPC_{10}$	9000		not determined	

Table 4.4 PEO copolymer properties. PEO copolymers generously donated from BASF. n_k reported for PEO blocks only. (a) Shar et al,[26] (b) Brandani et al[30]

polymer	M_w/M_n	number Kuhn segments n_k	adsorbed amount σ (nm^{-2})	spacing $\sigma^{-1/2}$
PEO_{141}-*b*-PPO_{51}-*b*-PEO_{141}	1.2[a]	64	0.12[a], 0.18[b]	2.9
PEO_{111}-b-PPO_{47}-b-PEO_{111}	1.1[a]	50	0.12[a]	2.8
PEO_{103}-b-PPO_{39}-b-PEO_{103}	1.1[a]	47	0.11[a]	3.0
PEO_{100}-b-PPO_{65}-b-PEO_{100}		45		
PEO_{76}-b-PPO_{29}-b-PEO_{76}	1.1[a]	34	0.13[a]	2.8
PEO_{62}-b-PPO_{40}-b-PEO_{62}	1.1[a]	28	0.17[a]	2.4
PEO_{37}-b-PPO_{56}-b-PEO_{37}		17	0.19[a], 0.24[b]	2.3
PEO_{27}-b-PPO_{61}-b-PEO_{27}		12	0.3[a]	
PEO_{26}-b-PPO_{40}-b-PEO_{26}	1.2[a]	11	0.23[a]	2.1
PEO_{17}-b-PPO_{60}-b-PEO_{17}		7		
used in Eq.	(4.11)	(4.10), (4.11)	(4.10), (4.11)	

4.3.2 Colloids and slides

Microscope slides (Fisher 12-549-3) were cleaned before use and dried with N_2. Clean slides were rendered hydrophobic by spin-coating (3000 RPM, 1 min) with a 3% w/w solution of polystyrene. Silica colloids of nominal 2.3 µm, 3.3 µm, 4.1 µm, and 5.0 µm diameter (Bangs Laboratories) were rendered hydrophobic by reactive coating with octadecanol (Sigma-Aldrich CAS 112-92-5). 120 nm nominal diameter polystyrene sulfate latex (Thermo Fisher Invitrogen S37391) was used for DLS measurements of polymer size and stability. Polymer brushes were formed onto hydrophobic silica and polystyrene particles by dissolving PMPC and PMAPS copolymers in DI, and contacting polymer

solutions with hydrophobic colloids or slides for a minimum of 4 hours. Free polymer was removed by at least 5 cycles of centrifugation and re-dispersion in the measurement solution (colloids), and 5 cycles of removing and replacing the liquid (slides).

4.3.3 Total internal reflection microscopy

Total internal reflection microscopy (TIRM) was used to measure the interactions and deposition of polymer-coated colloids onto glass slides. Briefly, an evanescent wave was excited along a SiO_2-DI interface using a 633 nm HeNe laser (Melles Griot). Images were captured using a 40× objective (LD Plan-NEOFLUAR), using a 12-bit CCD Camera (Hamamatsu Orca-ER) at 4 binning, 4 ms exposure, and a frame rate of 30 ms/frame. Custom software analyzed each image to estimate colloid scattering intensity. Relative height was calculated from

$$\frac{h}{h_m} = \beta^{-1} \ln\left(\frac{I}{I_m}\right) \tag{4.14}$$

in which I and h are the scattering intensity and colloid height, respectively, and the subscript m is the most probable observation bin. The decay length of the evanescent wave, β, was 113.67 nm.

TIRM monitored each combination of colloid and polymer for at least 2 hours. Deposition rates were qualitatively determined by recording the fraction of stable and deposited colloids over each measurement window. A deposition time constant $t_{1/2}$ was determined from the time at which approximately 50% of colloids were found to be deposited.

4.3.4 *Dynamic light scattering*

Dynamic light scattering (DLS) was conducted using a Malvern Instruments Nano-ZS ZetaSizer. The mean d_h and standard deviation σ_h of measured hydrodynamic diameter were calculated using the method of cumulants. The hydrodynamic thickness (L_h) of adsorbed polymer brushes on colloids was estimated from measurements of bare and coated polystyrene particles ($L_h = d_{h,brush} - d_{h,bare})/2$. Hydrodynamic brush thickness was only reported for monodisperse colloidal dispersions with polydispersity index (PDI = σ_h^2/d_h^2) less than 0.08. Increases in PDI and d_h were used to infer aggregation of colloids. Aggregation rates were judged relative to the aggregation of uncoated colloids. 'Fast' aggregation was within 10% of the uncoated colloid's aggregation rate; 'slow' aggregation was any slower aggregation that was statistically significant over the course of 24 hours.

4.3.5 *Quartz crystal microbalance with dissipation*

Quartz crystal microbalance with dissipation (QCM-D) was used to measure the thin-film properties of adsorbed polymer layers. A Qsense (Biolin Scientific) was operated with 5mhz SiO_2 crystals coated with ~1μm thick polystyrene layer. During signal recording, the sensors were first equilibrated with DI for approximately 2 hours. 1mg/mL polymer was injected under flow for at least 30 minutes or until signal equilibration. The sensors were then washed with DI for at least 2 hours. Layer properties during the polymer adsorption and washing steps were analyzed using a Kelvin-Voigt model of viscoelastic film properties provided by Biolin Scientific.[110]

4.4 Results & Discussion

4.4.1 Copolymer synthesis and steric stabilization of colloids

PMPC-b-PPO-b-PMPC triblock copolymers (hereafter referred to as PMPC copolymers) were synthesized by polymerization of PMPC monomer onto a Br-PPO$_{49}$-Br macroinitiator (**Fig. 4.1**). Stoichiometric control of reagents varied the degree of polymerization, n, of each PMPC block between n=10-80. PMPC copolymers were moderately polydisperse with M_w/M_n = 1.1-1.4 (**Table 4.3**). For comparison with PMPC copolymers, commercial PEO-b-PPO-b-PEO copolymers (hereafter referred to as PEO copolymers) were obtained with a range of PEO and PPO repeat unit configurations, with copolymer polydispersities between M_w/M_n = 1.1-1.2 as determined from literature studies.[29] **Table 4.3** and **Table 4.4** report the details of polymers studied in this chapter.

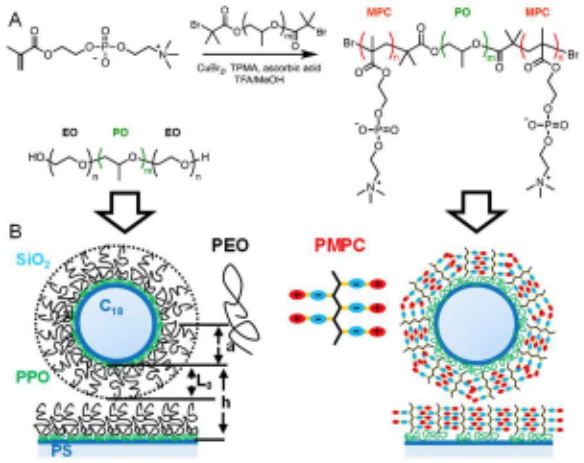

Fig. 4.1. Synthesis of PMPC triblock copolymers and adsorption onto hydrophobic colloids and surfaces. (**A**) Synthesis of PMPC-PPO-PMPC by ARGET-ATRP from a Br-PPO$_{49}$-Br macroinitiator. (**B**) Configuration for adsorption and schematic architecture of commercial PEO-PPO-PEO and synthesized PMPC-PPO-PMPC on hydrophobically modified (silane) silica colloids and glass microscope slides. The sphere-wall geometry is used to measure interaction potentials and deposition behavior. PMPC and PEO triblock copolymer molecular weights and number of repeat units are reported in **Table 4.3** and **Table 4.4**

Table 4.4

PMPC and PEO copolymers were adsorbed to hydrophobic silica colloids and glass microscope slides. The adsorbed copolymers are oriented with PPO blocks adsorbed onto the hydrophobic surfaces, and PEO or PMPC blocks extended into solution forming dense PEO or PMPC brush architectures.[26,29,30] Using this approach, silica colloids of diameter $2a$=100-400 nm were stabilized against aggregation using copolymers with PEO blocks of $n \geq 62$ and PMPC blocks of $n \geq 28$ (**Fig. 4.11**). Likewise, silica colloids of diameter $2a$=1.6-4.8μm were stabilized against deposition using copolymers with PEO blocks of $n>76$ and PMPC blocks of $n>28$ (**Fig. 4.12**). These results are consistent with expectations in that smaller colloids (with shorter range van der Waals attraction) and higher molecular weight PEO and PMPC blocks (with longer range repulsion) result in the greatest stability. However, the surprising result is that PEO blocks must have 2-3 times as many repeat units as PMPC blocks to impart the same degree of stability. This suggests important differences in layer architectures that we aim to understand via direct measurements of the colloidal interactions.

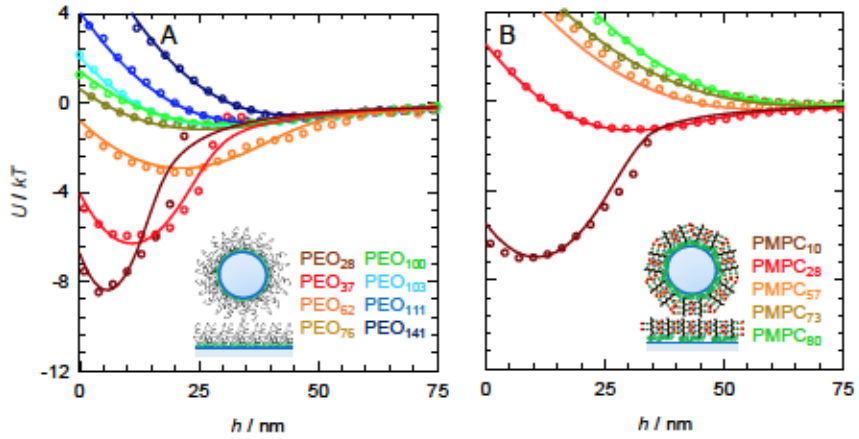

Fig. 4.2 Potential energy profiles (energy vs. separation) for molecular weight series of PEO and PMPC copolymers adsorbed to hydrophobic colloids and surfaces. Ensemble total internal reflection microscopy (TIRM) measurements in physiological ionic strength media of 3.2 micron silica colloids and glass surfaces hydrophobically modified with octadecyl chains and adsorbed copolymers of: (**A**) PEO-PPO-PEO with number of PEO repeat units reported in the legend, and (**B**) PMPC-PPO-PMPC with the number of PMPC repeat units reported in the legend (and n=49 for all PPO blocks). Points are ensemble averages of single particle measurements and lines are given by Eq. (4.15) using parameters reported in the main text.

4.4.2 Interaction potentials between adsorbed copolymers

Interaction potentials with nanometer and *kT*-scale resolution were directly measured between colloids and planar surfaces with adsorbed PEO and PMPC copolymers using ensemble TIRM.[74,108,111] Measured ensemble averaged potentials for copolymer coated silica colloids ($2a$=2.8um) are reported for varying PEO block repeat units (n=27-141) in **Fig. 4.2A** and varying PMPC block repeat units (n=28-80) in **Fig. 4.2B**. Single particle potentials are similar to each other and the ensemble average interaction (**Fig. 4.7**) indicating the uniformity of the adsorbed layers on particles and microscope slide, consistent with previous ensemble TIRM measurements.[43,112] For both copolymers, decreasing n decreases the range of repulsion between adsorbed polymer layers. As a result, the net potential varies from purely repulsive to having an attractive well due to van der Waals attraction between the silica particles and glass microscope slides. The PEO

copolymer results also show that varying PPO block sizes appear to have no role (*e.g.*, overlap of PEO_{103}-PPO_{39}-PEO_{103} and PEO_{100}-PPO_{65}-PEO_{100} profiles).

To model the measured interaction potentials, the net potential is considered as the superposition of van der Waals (vdW) and adsorbed polymer (P) interactions as,

$$U(h,a,f_0,L_0) = U_{vdW}(h,a) + U_P(h,a,f_0,L_0) \tag{4.15}$$

$$U_{vdW}(h,a) \cong -Aah^{-2} \tag{4.16}$$

$$U_P(h,a,f_0,L_0) \cong 4\pi a f_0 L_0 \frac{\alpha}{\beta} \exp\left[-(h\beta/2L_0)\right] \tag{4.17}$$

where A is the Hamaker constant for silica and polystyrene interacting across water,[75] f_0 and L_0 are the uncompressed layer free energy per area and layer thickness,[76,80] and α and β are semi-empirical constants[80] (details of derivations and fit parameter in Ch. 4.2). The polymer interaction potential (Eq.(4.17)) was originally developed for flexible polymers with short range monomer-solvent interactions,[22] and should be suitable for PEO (but less so for PMPC layers; this is explored in the following sections). Because the values a and A are known independently, and f_0 approaches a near hard-wall limit on the kT-scale of our measurements (further discussion in SI), L_0 is the only adjustable parameter. The theoretical fits in **Fig. 4.2** using Eqs. (4.15)-(4.17) accurately capture the net potentials and the adsorbed layer thicknesses vs. molecular weight.

Interaction potentials for fixed copolymer molecular weights and varying colloid radius were also directly measured (**Fig. 4.3**). By varying colloid radius for a fixed copolymer molecular weights, the well-established size-dependent silica van der Waals potential[75] can be used as a "ruler" to measure layer thickness. Using five different silica colloid sizes with radii from a=0.75-2.4 μm, measured potentials are reported for adsorbed

copolymers having PEO blocks with n=76 (**Fig. 4.3A**) and PMPC blocks with n=28 (**Fig. 4.3B**). These copolymers have similar thicknesses for the same colloid size in **Fig. 4.2**, and now show nearly similar potentials for different colloid sizes in **Fig. 4.3**. The potential minimum location is approximately independent of colloid radius, consistent with the Derjaguin approximation and potentials in Eqs. (4.16)-(4.17).[77] In the following sections, we further analyze the potentials in **Fig. 4.2** and **Fig. 4.3** to estimate how layer thicknesses scale with number of repeat units for both copolymers.

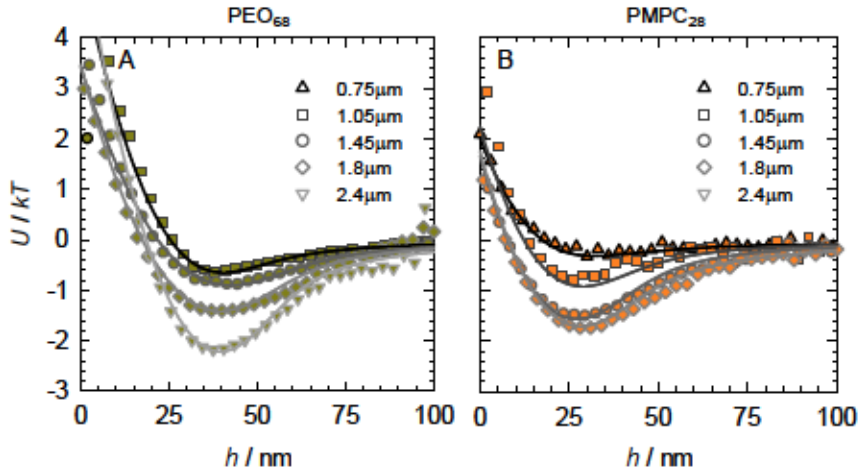

Fig. 4.3 Potential energy profiles (energy vs. separation) for different sized colloids and fixed molecular weights of adsorbed PEO and PMPC copolymers. Interaction potentials measured for same conditions as in **Fig. 4.2** but for silica colloids with diameters 2a=1.5, 2.1, 2.9, and 4.8 microns and adsorbed layers of: (**A**) PEO_{76}-PPO_{29}-PEO_{76} and (**B**) $PMPC_{28}$-PPO_{49}-$PMPC_{28}$. Points are ensemble averages of single particle measurements and lines are given by Eq. (4.15) using parameters reported in the main text.

4.4.3 Adsorbed copolymer thickness

Here, analysis of potentials in **Fig. 4.2** and **Fig. 4.3** estimated the scaling of the uncompressed layer thickness, L_0 with number of repeat units, n, for both PMPC and PEO copolymers. Plots in **Fig. 4.4** show as points L_0 values obtained from fits to the potentials in **Figs. 4.2** and 4.3 vs. repeat unit number for each PEO (**Fig. 4.4A**) and PMPC (**Fig. 4.4B**) block. Points are also shown for each adsorbed copolymer's hydrodynamic thickness L_h

(from dynamic light scattering) and effective mechanical film thickness L_F (from quart crystal microbalance). A series of lines are also reported in **Fig. 4.4** including: (1) the radius of gyration, $(n_k/6)^{0.5}L_k$, (2) the number average molecular weight contour length, $nL_M=(M_n/M_m)L_M$, (3) the weight average molecular weight contour length, $nL_M=(M_w/M_m)L_M$, (4) a theoretical thickness shown only for PEO (Eq. (4.11)), and (5) a fit $L_0(n)$ constrained to the form $L_0=c1n^{c2}$ ($c1$, $c2$ reported in SI, form chosen based on Eq. (4.18)).

All thicknesses increase with increasing number of repeat units, as expected. For both copolymers, the thickness for a given number of repeat units inferred from measured interactions is greater than other measures. This can be expected as the onset of repulsion between layers may depend more on chains at the adsorbed layer periphery than measurements of layer hydrodynamics or thin-film mechanics.[23,113,114]. When comparing PEO and PMPC copolymer layers at a given number of repeat units, the PMPC layers thicknesses are 2-3x greater than the PEO layer thicknesses. This indicates a clear difference between the two adsorbed triblock layer architectures.

Various reference polymer dimensions are plotted as lines in **Fig. 4.4** to understand differences between PEO and PMPC copolymer layer thicknesses and architectures. For the PEO copolymers, the layer thickness falls well within the range bound by the radius of gyration (R_G) and contour length Lc, and is quite close to predictions (Eq. (4.11)) with no adjustable parameters. In contrast, PMPC layers are highly extended, with the L_h near the number average contour length (Lc), and the thicknesses from potential energy fits very close to the weight average contour length (Lc_w). Such high PMPC chain extensions are observed in neutron scattering studies[64,115] and simulations of semi-flexible brushes when

the Kuhn length approaches the contour length[116–118] (which may correspond to the PMPC conditions here). PMPC polydispersity (M_w/M_n≈1.1-1.4; see **Table 4.3**) can also be expected to influence layer thickness.[119,120] Such polydispersity effects are not obvious for PEO layers, however, due to their moderate chain extension and lower polydispersities (M_w/M_n≈1.1-1.2; see **Table 4.4**). The authors are unaware of previous measurements or models of polymer layer interactions of varying Kuhn length or polydispersity, particularly for adsorbed polymer layer interactions approaching where $Lc_w \sim L_k$.

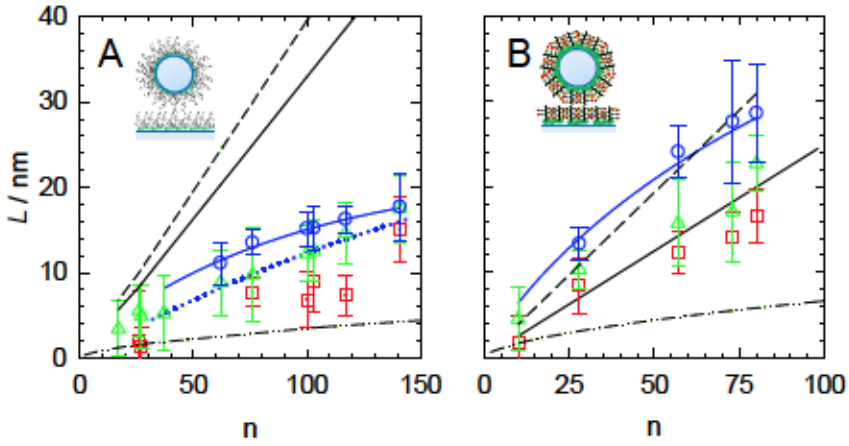

Fig. 4.4. Layer thicknesses vs. block repeat units from measurements and model fits for PEO and PMPC copolymers adsorbed to hydrophobic substrates. Measurements are reported as points for (**A**) PEO and (**B**) PMPC copolymers from (blue circles) uncompressed layer thicknesses from fits to TIRM measurements in Figs. 4.2-4.3, (green triangles) hydrodynamic thicknesses from DLS measurements, and (red squares) film thicknesses from QCMD. Models and reference dimensions are reported as lines for (blue line) power law fit ($C1n^{C2}$), (dotted blue line) polymer brush theory Eq. 4.15, and end block (black dash-dot) radius of gyration ($(n_K/6)^{0.5}L_K$), (black solid) contour length ($(M_n/M_m)L_M$), and (black dashed) weight-averaged molecular weight contour length ($(M_w/M_m)L_M$).

Other mechanisms could lead to thicker than expected PMPC layers, which we address here for completeness, but consider unlikely for cited reasons. For example, surface roughness can influence the range of van der Waals, and hence estimates of adsorbed layer thickness from fits to measured potential energy profiles; however, this has been shown not to be the case for adsorbed PEO copolymers both in the present work and previous

studies.[44] Adsorption is performed above the copolymer critical micelle concentrations (at 1mg/mL; C_{cmc} between 1-50μg/mL all copolymers) such that micelles could adsorb; however, layers are much thinner (5-30nm) than micelle dimensions (50-200nm), and micelle extrusion through 80nm pore membranes did not change measured interactions (see *SI*). Finally, multilayers or sequential adsorption is unlikely as shown in prior studies of zwitterionic polymers[121,122] and based on the observation of repulsive interactions between adjacent PMPC layers in the present work.

4.4.4 Energy minima vs. colloid and polymer dimensions

To better quantify how net attraction depends on layer and particle properties, **Fig. 4.5** summarizes how the potential energy minimum depth, U_M/kT, scales with both particle size and PEO and PMPC copolymer molecular weights. In particular, U_M/kT is reported for PEO and PMPC copolymers vs. colloid radius (**Fig. 4.5A,B**) and number of repeat units (**Fig. 4.5C,D**). Points are obtained from U_M/kT values fit to the measured potential energy profiles in **Figs. 2** and **3**. Lines were plotted by numerically determining $U_M(a)/kT$ and $U_M(n)/kT$ from Eq. (4.19) using the fit L_0 curves reported in **Fig. 4.4** (with no other adjustable parameters, see *SI*).

As seen in **Fig. 4.5A,B**, the measured U_M/kT points for both PEO and PMPC brushes are linear with a and well captured by the lines, which are linear in a via the Derjaguin approximation. Increasing n results in a decrease in the slope of U_M/kT versus a in **Figs. 5A,B** for both PEO and PMPC brushes. This n dependence is also accurately captured by in the slopes in **Fig. 4.5A,B** as well as the lines in **Fig. 4.5C,D**. When comparing the PEO and PMPC results in **Fig. 4.5C,D**, it is clear that less attraction is observed for the same colloid radius and number of repeat units of PMPC compared to

PEO stabilized colloids. This is again a consequence of the PMPC layers being ~2-3x thicker than PEO layers with the same number of repeat units.

The effectiveness of the model is further demonstrated in the **Fig. 4.5E,F**, which shows $(U_M/kT)/a$ vs. n and $(U_M/kT)/a$ vs. L_0. By plotting $(U_M/kT)/a$ vs. n in **Fig. 4.5E**, the data and model from **Fig. 4.5C,D** collapse onto one curve for PEO copolymer and one curve for PMPC copolymer. Practically, dividing the potentials by the colloid radius effectively removes the particle size dependence of the attractive energy minimum (*i.e.*, dividing both sides by a), but it does not remove the unique n dependence for the two copolymer types. By plotting $(U_M/kT)/a$ vs. L_0 in **Fig. 4.5F**, all data and models collapse onto a single curve for all particles sizes and PEO and PMPC molecular weights. Because **Fig. 4.5F** is effectively a plot of $U_M(n)/kT)/a$ from **Fig. 4.5E** vs. $L_0(n)$ from **Fig. 4.4A,B**, it shows how the model of the colloidal interactions and the layer dimensions together accurately capture all of the measurements in this work. It should also be noted that $0.8L_0$ accurately captures the L_h from DLS in **Fig. 4.4** (and could be used to predict layer thicknesses important for lubrication[68]). This suggests that the curve in **Fig. 4.5F** could be generated from DLS thicknesses by dividing by 0.8 (when direct measurements of interactions are not possible), and practically suggests that the more easily obtainable DLS thickness with a correction factor can be used for predicting interactions.

The results in **Fig. 4.5E,F** together show PEO and PMPC copolymers allow different amounts of attraction between colloids for the same number of repeat units, but the two copolymers yield the same level of attraction for the same layer thickness. As a result, differences in the ability of the two copolymers to stabilize colloids are unimportant once the two copolymers are compared for conditions that lead to the same layer thickness.

In other words, while the extended PMPC layer architecture appears to produce enhanced stability on the basis of comparing contour lengths, in the end it produces the same repulsion as a PEO copolymer layer of the same thickness. Ultimately, the fits using Eq. (4.15) in **Fig. 4.2**-**Fig. 4.4** accurately capture a diverse set of data in terms of potential energy profiles, uncompressed layer thicknesses, particle sizes, molecular weights, and copolymer compositions.

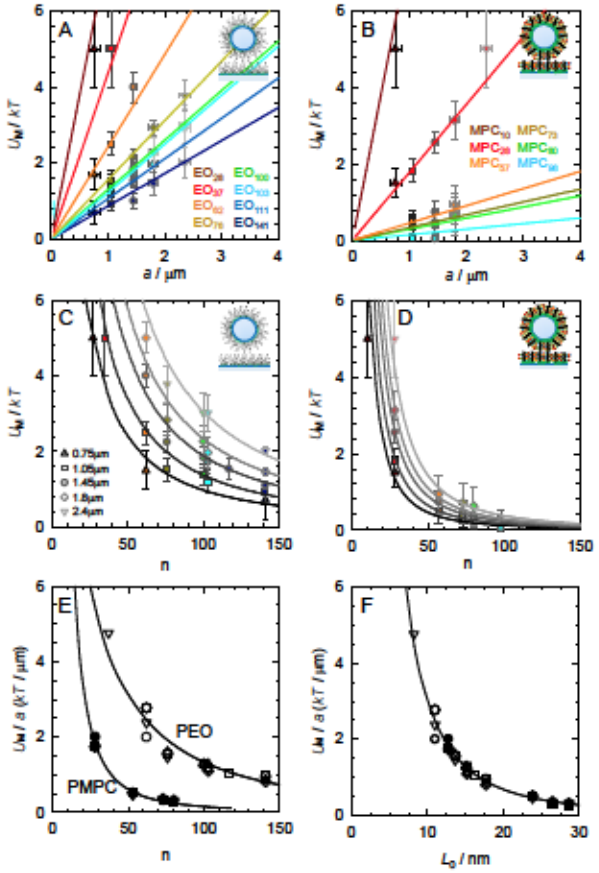

Fig. 4.5 Attractive potential energy minimum well depth vs. colloid size and PEO and PMPC block repeat units. Points from measurements in **Fig. 4.2-Fig. 4.3** and lines from Eq. (4.15). for potential energy minimum well depth, U_M/kT, vs. colloid radius, a, for (**A**) PEO copolymers and (**B**) PMPC copolymers and vs. block repeat units, n, for (**C**) PEO copolymers and (**D**) PMPC copolymers. Error bars are 95% confidence intervals from fits. Dividing U_M/kT by a produces (**E**) two unique curves for (black) PEO and (red) PMPC trends vs. n, and (**F**) a single universal curve when plotted against the uncompressed layer thickness, which shows equivalence of PEO and PMPC adsorbed copolymer repulsion for same layer thickness.

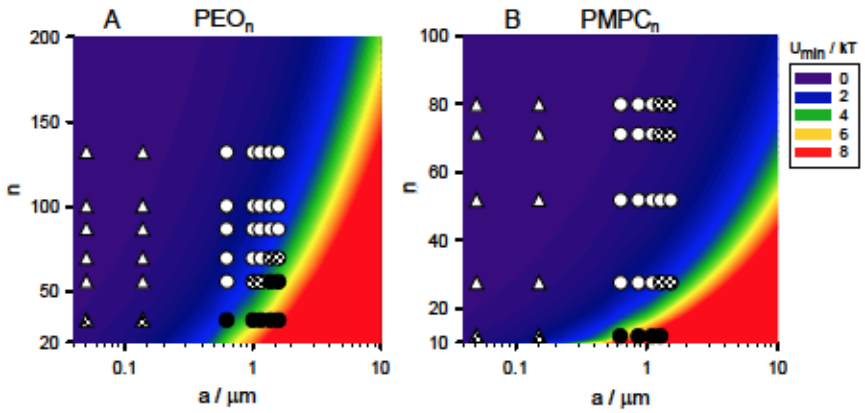

Fig. 4.6 Aggregation and deposition data for PEO and PMPC coated colloids compared to model for energy minimum vs. particle radius and number of block repeat units. Data reported for (**A**) PEO and (**B**) PMPC copolymers using symbol shape to indicate (triangles) DLS aggregation measurements and (circles) TIRM deposition measurements,[123] and symbol fill patterns to indicate (white) stable, (hatch) slow aggregation or deposition, and (black) rapid aggregation or deposition. $U_M(a,n)/kT$ obtained from Eq. (4.15) to show how attraction correlates with colloidal stability.

4.4.5 Copolymer mediated stability against aggregation & deposition

The ability of adsorbed copolymers to mediate attraction between colloids and surfaces practically determines whether particles aggregate or deposit on surfaces. All of the data in **Fig. 4.2**-**Fig. 4.5** show that adsorbed PMPC copolymers generate longer range repulsion than adsorbed PEO copolymers with the same n, which results in less attraction between colloids and surfaces. **Fig. 4.5C**-**E** perhaps show most clearly that, for the same n, PMPC copolymers results in less attraction than PEO copolymers. In the following, we report aggregation and deposition behavior of PMPC and PEO colloids in physiological media to unambiguously and quantitatively connect measurements and models of interactions to colloidal stability.

Fig. 4.6 shows points from aggregation (triangles) and deposition (circles) measurements using light scattering and optical microscopy (details in *SI*). Points are filled to indicate either stability or slow or rapid aggregation/deposition, where "rapid" indicates

aggregation/deposition on first contact, and "slow" indicates kinetics where multiple collisions are required for aggregation/deposition. To connect the deposition behavior to the measured and modeled interactions, contour plots are also shown in **Fig. 4.6** for $U_M(a, n)/kT$ from Eq. (4.15). There is a clear correspondence between a transition in the data from stable to unstable in the vicinity of the energy contours where $|U_M(a, n)/kT| \approx 4kT$. The measured interaction potentials and the model fit in Eq. (4.15) provide quantitative guidance for predicting deposition and aggregation behavior across a wide range PEO and PMPC copolymer molecular weights as well as colloidal particle radii.

Several points in **Fig. 4.6** are not well captured by the underlying model for attraction, which tend to occur in limiting cases of molecular weight and particle size. Copolymers having PEO blocks with $n<28$ and PMPC blocks with $n<10$ on colloids with $a<200$nm exhibit slow aggregation when the model predicts little to no attraction. This discrepancy could arise from extrapolation of modeled interactions that correspond to measurements of larger a and n. Several mechanisms that could lead to lower stability for small a and n include: (1) lower adsorbed amounts that lead to thinner than expected layers, (2) particle curvature reducing lateral crowding to produce thinner layers (for $L_0/a>0.1$), which would be significant for lower n,[77–79,124] (3) the Derjaguin approximation becomes less valid for scaling potentials for small a.[125] Slow deposition was also observed for PMPC copolymers with $n>73$ when adsorbed to colloids with $a>1\mu$m. Because these particles were stable in the presence of 20ppm free solution copolymer (**Fig. 4.11**-**Fig. 4.12**), and QCM-D measurements indicated partial desorption for these higher molecular weight PMPC copolymers (**Fig. 4.10**), it seems likely that PMPC desorption destabilized these

particles. Smaller particles with the same adsorbed polymers are likely more tolerant of some desorption given their shorter range van der Waals attraction.

Finally, when comparing the PEO and PMPC copolymer stabilization results in **Fig. 4.6**, the behaviors are practically identical (as in **Fig. 4.5F**) when PEO copolymers are compared to PMPC copolymers with half as many repeat units, which produces the same layer thicknesses. Although PMPC copolymers can desorbed for high molecular weights, a small bulk concentration appears to suppress desorption and stability issues. Given the similar performance of PEO and PMPC copolymers at stabilizing colloids in physiological ionic strength media, it is not clear that one polymer is inherently better than the other one. Future work is in progress to test other performance criteria for PEO and PMPC triblock copolymers including stability in the presence of solution additives, temperature changes, and interactions with various biomaterials.

4.5 Conclusion

This chapter reports the interactions and colloidal stabilization of adsorbed PMPC copolymers and PEO analogues. Adsorption of copolymers to both hydrophobic colloids and surfaces produces thick layers that stabilize colloids against aggregation and deposition in physiological ionic strength media. Direct measurements of interaction potentials vs. colloid size and copolymer molecular weights, in conjunction with a theoretical model, provide a sensitive measure of adsorbed copolymer layer thickness vs. number of block repeat units. This model also captures aggregation/deposition behavior vs. particle size, block molecular weight, and copolymer compositions.

Adsorbed PMPC copolymers were found to produce extended architectures with layer thicknesses comparable to PMPC block contour lengths. For the same number of

block repeat units, PMPC layers were ~2-3 fold thicker than adsorbed PEO copolymer layers, which had thicknesses that were well described by standard polymer brush theory. However, adsorbed PEO copolymer layers with the same thickness as PMPC layers produced the same repulsion and degree of stability. These results provide a rigorous explanation for some observations of enhanced PMPC stabilization via extended layers. However, the findings also show that when PEO and PMPC layers of the same thickness are compared, their performance is identical. Ultimately, careful, direct measurements of colloid interactions show that adsorbed PMPC brushes perform as well as analogous PEO copolymers for stabilizing nano- and micro- colloidal particles in physiological media.

4.6 Supplemental

4.6.1 Measurement and fit of interaction parameters

Particle-substrate interaction potentials were measured as shown in **Fig. 4.7**. Potentials were determined individually for each single particle, and combined to form an ensemble average potential. The ensemble average of the measured potential ($U+U_G$, inset) was fit to Eq. (4.2) to determine the parameters a and L_0. Although f_0 was also used as a fitting parameter, its determination did not have a significant effect on the fit potentials as discussed later. The gravitational contribution (U_G) was subtracted, as shown in the main figures, to better compare the polymer and van der Waals surface interactions that determine colloid stability and behavior.

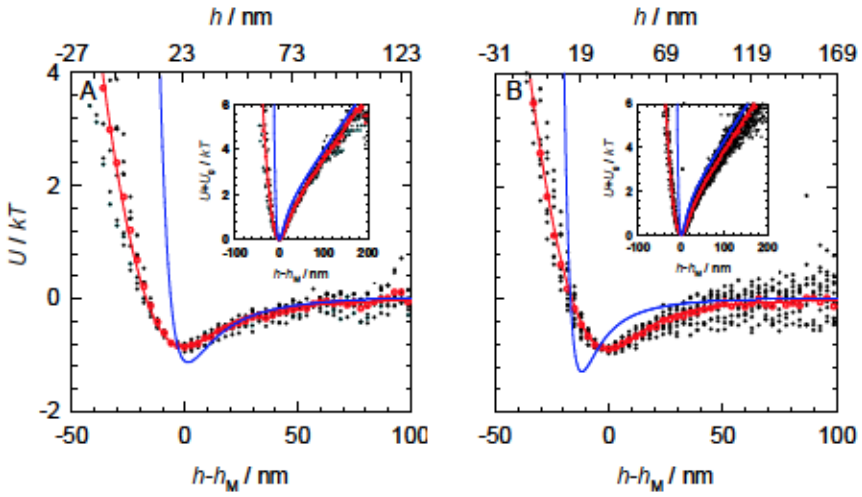

Fig. 4.7 Interaction profiles between brush-coated colloids and planar substrates. Colloids with adsorbed (**A**) PEO (n = 76) and (**B**) PMPC (n = 28) copolymer. In both panels: single particle profiles (black circles), ensemble average (red circles), fit to ensemble average (red line), and fit to measurement with noise removed (blue line). Insets depict the measured interaction potential before the subtraction of gravity.

The uncompressed polymer layer free energy (f_0) was not an important fitting parameter for either PMPC or PEO. f_0 from fits to profiles are shown in **Fig. 4.8**, for adsorbed PEO (black circles) and PMPC (red circles). All f_0 for adsorbed PEO and PMPC copolymers are very large ($f_0 > 10^6\ kT/\mu m^2$), with large 95% confidence intervals reflecting the parameter unimportance on fit quality. Using the measured adsorption of adsorbed PEO copolymer (**Table 4.4**) this corresponds to a free energy cost between 8-15 kT per polymer chain, which is reasonable for copolymer adsorption driven by the PPO block deposition onto a hydrophobic surface. The measured f_0 of adsorbed PEO is also compared to calculations using Eq. (4.11) and measured polymer parameters in **Table 4.2**-**Table 4.4**. As shown in **Fig. 4.8**, f_0 is predicted to be between 1-3x10^6 kT μm^{-2} using adsorption information from Stroeve et al.[30] (stars) and Shar et al.[26] (triangles), which is similar to the fit f_0 values. f_0 was not calculated for adsorbed PMPC which does not satisfy the flexible polymer assumption in Eq. (4.10)-(4.11). Simulations of semiflexible polymers suggest

several kT per chain under similar conditions as this work, which is lower than our measurements of between 10-20 kT per chain. This discrepancy is reasonable and within the hard-wall regime discussed next.

The measured and estimated $f_0 > 10^6$ for all studied conditions approaches the hard wall limit (incompressible polymer) in the kT interaction regime. This is shown in **Fig. 4.8B**, which shows the effective potential well depth (U_M) for $a = 1$ μm colloid interaction surface with van der Waals and polymer interactions. U_M is within 5% of the hard-wall (incompressible) polymer limit for $f_0 \geq 10^5\ kT\ \mu m^{-1}$ for all $L_0 \geq 10$ nm. Significant deviation from the hard wall U_M is only observed for very low $f_0 < 10^4\ kT/\mu m^2$ and $L_0 < 15$ μm. Large variations in f_0 around our fitted values thus have a small impact on the overall colloidal interactions on the kT scale, explaining the observed insensitivity of our measured interactions to f_0.

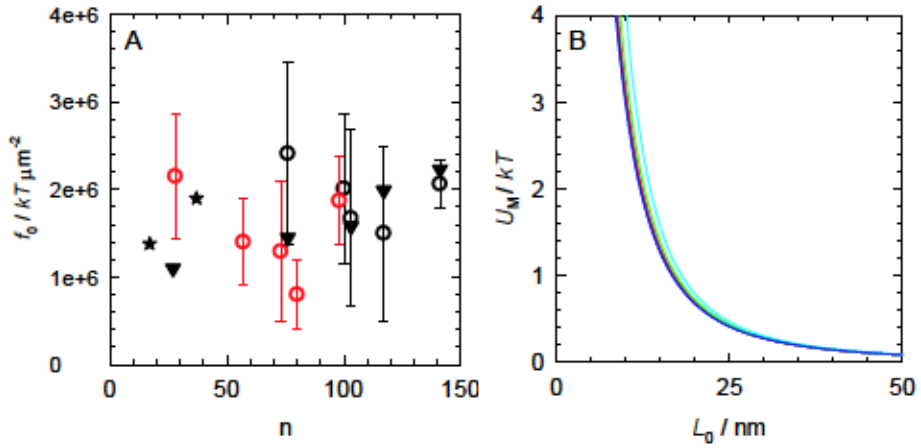

Fig. 4.8 Impact of f_0 on interpretations of colloidal behavior at the kT scale. (**A**) Uncompressed free energy / area (f_0) of the polymer brush for PEO (black) or PMPC (red). Fits of measured potentials to Eq. (4.17) (open circles), with 95% interval of estimation. Filled symbols are calculated from theory[76] (Eq. (4.10)) using polymer interaction parameters in **Table 4.2-Table 4.4**, and measured adsorption information from Brandani et al[30] (stars) and Shar et al[26] (triangles). (**B**) Dependence of the attractive well depth U_M on f_0 and L_0 for a = 1 μm. Plots are U_M, the minimum of $U_{vdW}+U_P$ for f_0 of 10^3 (cyan), 10^4 (green), 10^5 (red), 10^6 (blue) $kT/\mu m^2$, and ∞ (hard wall, black).

4.6.2 Analysis of polymer layer thickness

The polymer-mediated colloidal potentials were measured for colloids between 2-5μm diameter. This determined L_0 across a wide range of polymer molecular weight, where L_0 was expressed across copolymers in **Fig. 4.4** using,

$$L_0(\mathrm{N}) = CN\sigma(\mathrm{N})^{1/3} \tag{4.18}$$

This is a simplification of Eq. (4.11) that ignores any dependence of ω or Lk on the polymer size and local polymer concentration at the adsorbed surface. For power-law adsorption, which is a suitable assumption for a narrow range of polymer molecular weights, this can further simplify to,

$$L_0(\mathrm{N}) = C_1 N^{C_2} \tag{4.19}$$

The constants C_1, C_2 were separately fitted for PMPC and PEO L_0 to create a unified description of colloidal attraction across a wide range of polymer and colloid sizes, e.g. $U_M(N,a)$. The semi-empirical nature of Eq. (4.19) is necessary for PMPC copolymers, as (1) the PMPC L_k has several conflicting measurements, complicating its use in predictions and (2) we were unable to measure the adsorbed mass of PMPC copolymers to a high enough resolution for prediction. Estimates of Eq. (4.18) are possible for PEO copolymers, however, as several studies have characterized the adsorption of the PEO copolymers onto hydrophobic surfaces and the solution properties of PEO homopolymer are well studied. We expressed the adsorbed amount using a simple linear relation in **Fig. 4.9**. The estimation is approximately 20-30% smaller than the measured values. This reduction is reasonable as simulations suggest brush models under-predict extension of the polymer periphery, especially for polydisperse polymers. The agreement is very good given the number of parameters (M_n, M_w, ω, L_k, σ) necessary to make the predictions.

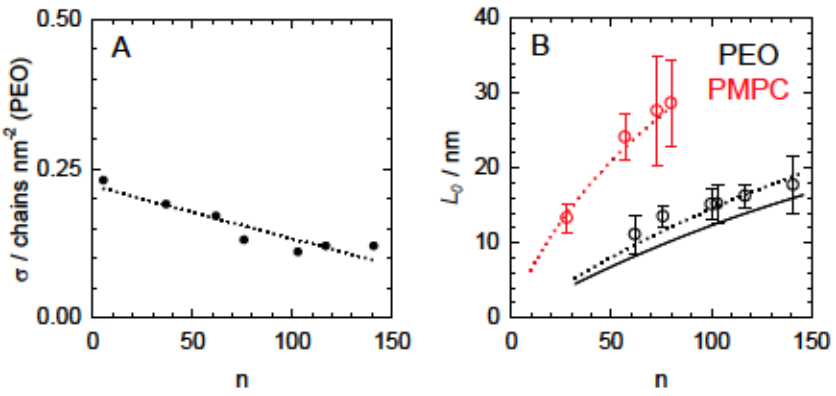

Fig. 4.9 Fit and prediction of steric thickness (L_0) across PEO and PMPC copolymer molecular weights series. (**A**) Adsorption of PEO copolymers used in (4.11) and (4.18) from literature (circles)[1] with linear fit, for estimation in **Fig. 4.4A** (dashed-blue line). (**B**) Estimation of $L_0(N)$ for PMPC (red) and PEO (black). Circles and error bars are the average and 3 standard deviations from fits of L_0 to interaction measurements. Dotted lines are two parameter fit to (4.19). Solid line is prediction with no adjustable parameters using data in panel A and in **Table 4.4**.

Layer thickness during adsorption and desorption of copolymer onto polystyrene was observed using QCM-D. The mechanical film thickness of an equivalent viscoelastic layer is shown in **Fig. 4.10**. Adsorption (black) represents the layer thickness after approximately 90 min of contact with polymer, and desorption (white) represents layer thickness after approximately 90 min of subsequent washing with deionized water. In general, most adsorbed PEO and PMPC layers demonstrate between a 10-20% reduction in layer thickness during washing. Adsorbed PMPC (n = 73,80) however display a much greater ~30% decrease in length.

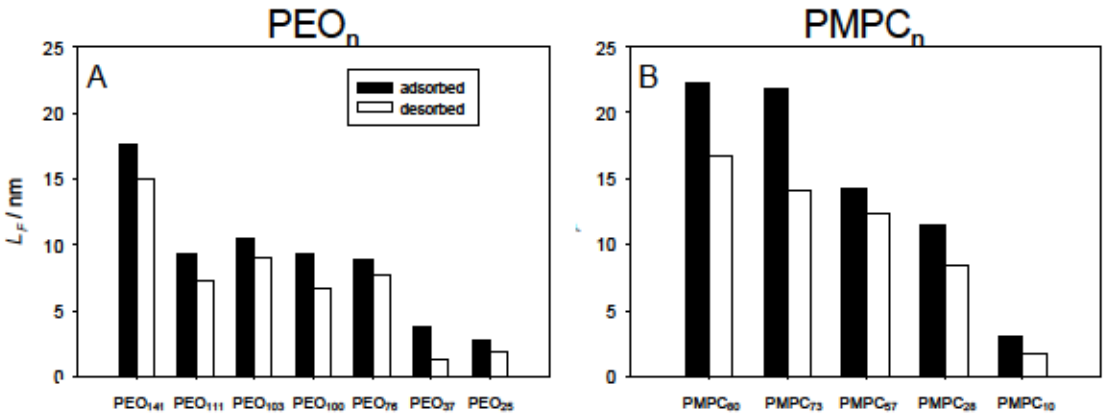

Fig. 4.10 Film thickness L_F of the adsorbed polymer layer determined from QCM-D. Adsorption of PEO (A) and PMPC (B) copolymers onto polystyrene. Layer thickness during adsorption (black); layer thickness after a 1 hour wash with deionized water (white).

4.6.3 Colloid deposition & aggregation

The stability of polymer-coated colloids was determined by monitoring aggregation in solution and deposition onto glass slides. Phosphate buffered saline (~150mM NaCl, pH 7.2) was used in all deposition and aggregation experiments to screen any residual charge after polymer adsorption. Aggregation and deposition rates were assessed as rapid, slow, or stable (not aggregating/depositing).

Aggregation of 100 nm and 400 nm diameter polystyrene colloids with adsorbed PEO and PMPC brushes was monitored over 24 hours using dynamic light scattering. Example results for brushes on 100 nm polystyrene are shown in **Fig. 4.11**, with similar behavior observed for 400 nm colloids. **Fig. 4.11** reports the polydispersity, PDI = α^2_h / a^2_h with α^2_h and a_h the variance and mean of the hydrodynamic size distribution. Significant changes in size and polydispersity were not observed for colloids with most adsorbed copolymers. Aggregation was not observed for colloids with all adsorbed PEO copolymers studied. Colloids with PMPC (n = 10) slowly aggregated, with a small polydispersity of

0.12 over one hour and high polydispersity of ~0.8 after 24 hr. Colloids with adsorbed PMPC (n = 73,80) aggregated slowly, with a large increase in polydispersity after 24 hours but insignificant changes in polydispersity after 1 hour. Notably, the colloids with adsorbed PMPC (n = 73, 80) did not aggregate when 30 ppm polymer was included in the PBS solution during aggregation experiments. This suggests the aggregation was due to polymer desorption rather than the adsorbed polymer architectures.

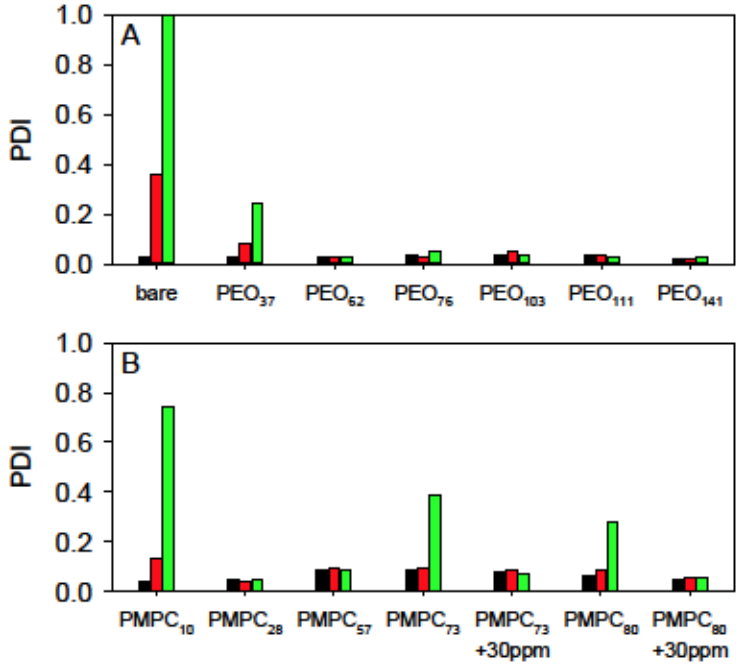

Fig. 4.11 Aggregation of 100nm PS colloids monitored by DLS. Polydispersity (PDI) of colloids with adsorbed (**A**) PEO and (**B**) PMPC copolymer. PDI = α_h^2 / a_h^2 in which α_h and a_h are the standard deviation and mean of the measured size distribution. Polydispersity increases with colloidal aggregation, with PDI < 0.1 typically considered monodisperse

Deposition experiments monitored colloids diffusing across slides over 24 hours using video microscopy. This analysis estimated a $t_{1/2}$ as the time when approximately 50% of colloids were deposited. Deposition rates are reported using $t_{1/2}$ for 0.8-2.4 μm radius colloids with PEO (in **Fig. 4.12A**) and PMPC (**Fig. 4.12B**) brushes. The colloids showed three distinct deposition behaviors for the different adsorbed brushes. (i) Colloids with PEO

(n = 17-37) and $PMPC_{10}$ brushes rapidly and irreversibly deposited. These systems have small $t_{1/2}$ with a strong net attractive potential ($U_M > 4kT$ in **Fig. 4.5**) that causes rapid, irreversible binding. (ii) Colloids with PEO (n = 100-141) and PMPC (n = 28-57) brushes did not significantly deposit over the course of monitoring. These systems have large $t_{1/2} >$ 100 h, with either very weakly attractive or repulsive potentials ($U_M < 2kT$) that do not associate. (iii) Lastly, colloids with PEO (n = 68,76) and PMPC (n = 73,80) brushes slowly deposit over the course of experiments, and possess intermediate $t_{1/2}$ values.

For PEO (n = 68, 76), slow deposition is likely caused by intermediate attraction strengths (U_M of 2-4kT). Such weak attraction should produce reversible binding, perhaps unless the particle encounters local surface heterogeneity where binding is stronger. Unlike PEO (n = 68,76), PMPC (n = 73,80) did not deposit when 30 ppm of the adsorbed copolymer was present in the liquid solution during deposition measurements. This together with the high desorption amounts measured for the PMPC (n = 73,80) brushes using QCM-D (**Fig. 4.10**), suggests that deposition of colloids with adsorbed PMPC is not due to attractive colloidal interactions, but is more likely the result of significant surface heterogeneities created during polymer desorption. This behavior is not seen for the PMPC copolymers with smaller blocks, and is likely a result of the increased affinity of the copolymer for the liquid solution caused by the increased hydrophilic block size.

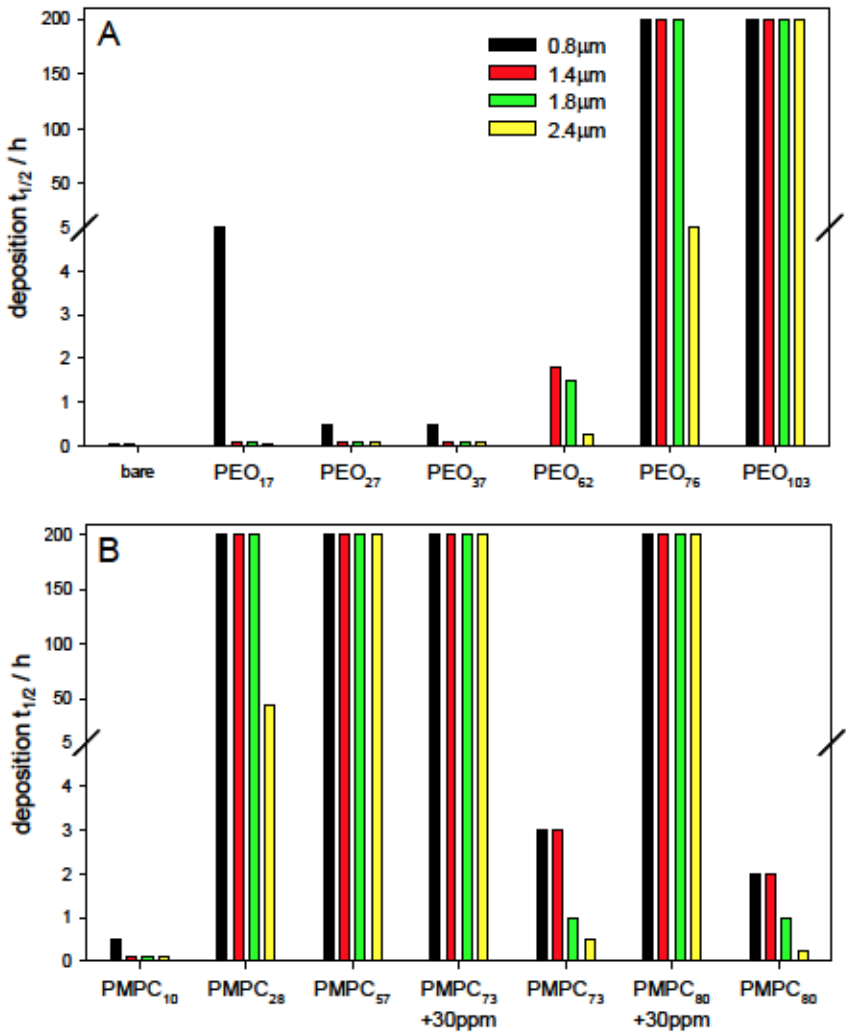

Fig. 4.12 Deposition half-lives of colloids during single-particle microscopy experiments. Deposition time, $t_{1/2}$, the time for 50% of particles in an experiment to deposit. Colors indicate measured colloid radius a. $t_{1/2}$ = 20 h indicates no time-dependent deposition over the observation time. Values of $t_{1/2}$ < 1 indicate very rapid deposition. Deposition of colloids with PMPC (n = 73, 80) brushes was not observed for experiments when 30 ppm of the polymer was included in the free solution.

5 DEPOSITION OF COLLOIDS WITH ADSORBED ETHYLENE-OXIDE AND PHOSPHORYLCHOLINE POLYMERS ONTO BIOMATERIALS

5.1 Introduction

The previous chapter demonstrated that polymer layer thickness is a key parameter in the determination of colloidal interactions and stability. However studies were performed in a model system with identical polymer coatings on opposing colloidal surfaces. Understanding such 'symmetric' polymer interactions is appropriate for unambiguous interpretation of polymer layer mechanics, and relevant towards applications such as the formulation of colloidal dispersions. For well-solvated polymer layers with net polymer-polymer repulsion (as was the case in Ch 4), the stability of colloids with symmetric layers is influenced solely by non-specific colloidal interactions (e.g. van der Waals and polymer layer compression).[73]

Importantly, symmetric layer interactions are somewhat abstracted from common applications in physiological and environmental settings, where a polymer layer must repel a wide range of foreign materials such as proteins, polysaccharide, lipids, and tissue linings.[13] Such foreign materials may destabilize a system by changing not only the non-specific colloidal interactions, but also by the addition of attractive specific interactions with the colloid's polymer layer. Notably, colloidal stability (i.e. resistance to deposition or aggregation) in biological environments is a chief in-vitro surrogate of a drug delivery system's performance.[54,89]

The stability of zwitterionic (ZW) polymer-coated surfaces in biological and environmental applications has largely been studied through measurement of protein adsorption.[11,52,90,126,127] Such anti-fouling studies are largely the source of the 'improved

performance' claims of ZW polymers relative to traditional anti-fouling polymer chemistries.[15,128] However, protein adsorption is typically studied using techniques that measure total adsorbed protein mass onto a surface, and most studies compare a limited set of poorly-characterized polymer architectures when comparing various polymer chemistries. It is thus unclear if the reported performance improvements from ZW polymer layers are due to differences in layer chemistry, architecture, or surface heterogeneities. In addition, except for immunological clearance mechanisms (that are typically initiated by protein adsorption),[6] resistance to protein adsorption is at best an indirect indicator of a colloid's stability in a biological environment.

Comparatively fewer studies, however, have directly probed the aggregation and deposition of ZW-coated colloids in biological environments. Notable works include the stabilization of ZW-coated Au,[96] SiO_2,[129,130] and quantum dot[104] nanoparticles against aggregation in high-salt and protein solutions. Yang et al[54] demonstrated both an improved stability in serum and increased circulation times during systematic administration in rodents of colloids with poly(carboxybetaine) vs. PEO coatings. However none of these studies engaged in a systematic variation of both coating architecture and monomer chemistry, and thus did not reveal the important layer properties and interactions that impart colloidal stability. These studies also did not directly study stabilization against deposition, one of the two major mechanisms for particle clearance and loss of function in vivo.[7]

A further understanding of colloidal stabilization against common biomaterial chemistries and environments would facilitate improved design of drug delivery and diagnostic materials, which have largely been focused on polymer chemistry as the main

vehicle towards improving material performance. This chapter studies the impact of a polymer coating's chemistry and thickness on the stability of colloids diffusing across biomaterial surfaces. Colloids are coated with a molecular weight series of adsorbed amphiphilic copolymers, creating PEO and ZW poly(2-methacryloyloxyethyl phosphorylcholine) (PMPC) coatings of 13-21nm thickness. The diffusion of polymer-coated colloids across protein, hyaluronan, and mucus biomaterial surfaces, chosen for relevance to common drug delivery obstacles, is monitored with total internal reflection microscopy (TIRM) at nanometer and millisecond precision. Binding characteristics chiefly depend on polymer and biomaterial coating thickness, revealing the importance of non-specific interactions in stabilizing colloids. The single-particle level of analysis also reveals the role of coating heterogeneities in determining colloid stability. Together, findings show important aspects of polymer coatings and architectures that determine stability in biomaterial environments and applications.

5.2 Materials and Methods

5.2.1 Polymer synthesis and characterization

PEO-b-PPO-b-PEO block copolymers (herein 'PEO copolymers') were generously donated from BASF. PMPC-b-PPO_{49}-b-PMPC block copolymers (herein 'PMPC copolymers') were synthesized using activator regenerated by electron transfer-atom transfer radical polymerization (ARGET-ATRP).[131] PMPC copolymer synthesis and characterization were described in detail in a previous paper. Briefly, MPC monomer (Sigma, 67881-98-5) was polymerized onto a Br-PPO_{49}-Br macroinitiator in dry methanol and under Argon at 40°C using a $CuCl_2$ catalyst. Unreacted MPC monomer was purified

by crystallization in methanol. M_n and M_w of PMPC-PPO-PMPC copolymer were estimated using NMR and static light scattering as described in SI. Details of PEO and PMPC copolymers are reported in **Table 5.1**. The length of steric interactions from the polymer layer (L_0) was determined from measurement of colloidal interaction potentials with adsorbed polymer, as reported previously.

Table 5.1. Amphiphilic triblock copolymers used to form PMPC and PEO adsorbed brushes.

polymer	layer thickness L_0 / nm	polydispersity M_w/M_n
PEO_{76}-PPO_{29}-PEO_{76}	14	1.1[a]
PEO_{141}-PPO_{51}-PEO_{141}	20	1.2[a]
$PMPC_{28}$-PPO_{49}-$PMPC_{28}$	13	1.1[b]
$PMPC_{57}$-PPO_{49}-$PMPC_{57}$	21	1.4[b]

a Brandani et al[30]
b M_n H1 NMR (methanol-d4); M_w SLS (tetraflouroethanol)

Table 5.2. Overview of biomaterial surfaces and surface properties

biomaterial	model of	layer thickness L_0 / nm
bovine serum albumin (BSA)	protein surface, serum	8
100kDa hyaluranon	extracellular matrix	120
porcine intestine mucus	mucosal linings (lung, vaginal, intestinal)	570

5.2.2 Colloid surface preparation

PEO and PMPC copolymers were adsorbed onto hydrophobic colloids to form PEO and PMPC polymer brush coatings. 3.2µm silica colloids (Bangs Laboratories, SS05N)

were rendered hydrophobic by coating with octadecyl as described previously[132] and stored in ethanol. For adsorption, 2μL of 0.1% v/v hydrophobic silica in ethanol was added to 1mL of 1mg/mL copolymer in deionized water (DI) and mixed. After 4 hours, unadsorbed polymer was removed by at least 5 cycles of centrifugation and re-dispersion in phosphate buffered saline (Fisher, 20-012-043).

5.2.3 Biomaterial surface preparation

Glass slides (Fisher, 12-549-3) were cleaned with sequential sonication in acetone, isopropanol, and DI for 30 minute each. Slides were then soaked in NoChromix (Godax Laboratories, 19-010) for at least 1 hour, rinsed with DI, and dried with N_2. To render hydrophobic, dried slides were spin coated with 2% w/w polystyrene in toluene at 3k RPM for 1 minute. To present NH_2, dried slides were added to solution of 2% v/v 3-aminopropyl triethoxysilane (APTES, Sigma, 440140) in toluene for 16 hours at room temperature. After APTES reaction, the NH_2-presenting slides were sequentially rinsed with toluene, isopropanol, and DI, dried with N_2, and baked at 80°C for 1 hour. Batch cells for microscopy were prepared on polystyrene or NH_2 slides by addition of 0.5mm viton orings sealed with vacuum grease.

Bovine Serum Albumin (BSA, Sigma-Aldritch, A2058) and porcine mucus (Sigma-Aldrich, M1778) were physisorbed onto hydrophobic polystyrene glass slides. BSA and mucus solution were dissolved at 1mg/mL in PBS and filtered through a 0.22μm cellulose acetate syringe filter (Fisher, CAS022550). Filtered BSA or mucus solution was then added to the batch cells on polystyrene slides for adsorption over at least 4 hours. 100 kDa hyaluronan (R&D Systems, GLR004) was chemisorbed onto dried NH_2-presenting slides using carbodiimide chemistry. 3mg/mL hyaluronan, 0.5M N-hydroxysuccinimide

(NHS, Fisher, AC157270250) and 0.5M *N*-(3-Dimethylaminopropyl)-*N'*-ethylcarbodiimide hydrochloride (EDC, Sigma-Aldrich, E6383) were prepared in 150mM NaCl, 10mM HEPES, pH 6.0 buffer. The hyaluronan-EDC-NHS solution was then immediately added batch cells on NH_2-presenting slides for reaction with the amine and crosslinking. Unbound BSA, mucus, or hyaluronan were removed by washing batch cells with filtered PBS, and sealed with a glass coverslip after particle addition. The BSA, mucus, and hyaluronan surface properties are listed in **Table 5.2**. Coating of colloids with BSA, mucus, and hyaluronan followed the same protocols as slide coverage.

5.2.4 TIRM Microscopy

Total internal reflection microscopy (TIRM) recorded ensembles of colloids diffusing across biomaterial surfaces. Details are described in previous publications.[44,108,133] Briefly, videos of diffusing colloids were collected using an optical microscope (Axioplan 2, Zwiss) equipped with a 40× optical objective (LD Plan-NEOFLUAR) and charge coupled device (CCD) camera (ORCA-ER, Hamamatsu) at 4 binning and 30 millisecond recording rate. Samples were illuminated by exciting an evanescent wave with 113 nm decay length on a 68° dovetail prism using a 633 nm HeNe laser (Melles Griot). The biomaterial surface was optically coupled to the dovetail prism, with colloids dispersed in solution above the biomaterial surface scattering light from the evanescent wave. Video images of colloids scattering were analyzed with custom Fortran software to determine lateral position (~100 nm resolution) and scattering intensity of each colloid over time. The separation of each colloid from the slide h was determined from the colloid's scattering intensity I with ~1 nm resolution using

$$I(h) = I_0 \exp\left(-\beta^{-1} h(t)\right) \tag{5.1}$$

where h is the height of the particle above the slide, I_0 is the scattering intensity at colloid-slide contact (at $h = 0$), and β is the evanescent wave decay length (113 nm).

TIRM measurements recorded videos of between 5-15 min duration across a total timespan of at least 2 hours. Trajectories of at least 40 colloids were recorded for each combination of polymer chemistry, polymer thickness, and biomaterial surface.

5.2.5 Diffusion analysis and binding lifetime

The diffusion trajectories of colloids were analyzed to determine the distribution of lifetimes for which each colloid was deposited to a surface, following previous approaches.[112,123,134] The mean lifetime t_D that a colloid remains deposited to a surface is given by,[81]

$$t_D \propto t_{FD} \exp\left(U_M / kT\right) \tag{5.2}$$

in which $t_{FD} = l^2 / \langle D \rangle$ is the mean time for the diffusing object to traverse the length scale l with mean diffusivity $\langle D \rangle$, U_M is the potential energy barrier between the bound and unbound states, and kT is thermal energy. Eq. (5.2) is a particular solution to the Smoluchowski equation (Eq (2.22)) describing the mean first passage time of a Brownian object trapped by a potential barrier of height U_M (Kramer's escape problem).[82] $\langle D \rangle$ is estimated from the Stokes-Einstein equation multiplied by a drag coefficient c_d for diffusion normal to a planar surface,

$$\langle D \rangle = c_d \left(L_{0,B} + L_{0,P}\right) \frac{kT}{6\pi\eta a} \tag{5.3}$$

Colloids were determined to be deposited over the time interval t_{FD} when the variance in motion was less than the characteristic diffusion length,

$$\mathrm{var}\left(h_i, h_{i+1} \ldots h_j\right) t_{FD} < 2l^2 \tag{5.4}$$

Measurements used l = 8 nm which was approximately twice the standard deviation of signal of a motionless particle in our setup. Fluctuations in normal motion were used to determine bound and unbound states, as the greater spatial precision in determining normal vs. lateral position from TIRM allows greater temporal precision in determining t_D.

c_d and thus t_d can be rigorously estimated from hydrodynamic models of colloids with adsorbed polymer. However accurate estimation requires a quantitative understanding of attributes such as polymer layer thickness, layer surface density, and chain penetration between opposing polymer layers. Instead, c_d was used empirically as an adjustable parameter to maximize the ability of automated analysis to correctly identify control stable and unstable colloids for each material system of interest (i.e. chose c_d to set the t_{FD} that maximized particle classification in Eq. (5.4)).

Finally, a nondimensional, logarithmically-spaced deposition lifetime θ_d was used for comparison across measurement conditions as,

$$\theta_d = \frac{\ln\left(t_d / t_{FD}\right)}{\ln\left(t_O / t_{FD}\right)} \tag{5.5}$$

in which t_O is the observation time of 5 minutes for all measurements.

5.3 Results & Discussion

The following assesses the role of a polymer coating's chemistry and architecture on the stabilization of particles against deposition onto various model biomaterials. This

section first discusses the determination and quantification of deposition across both single particles and ensembles of colloids. This analyses is then implemented to assess the deposition and stability of colloids with PEO and PMPC coatings of systematically varied thicknesses.

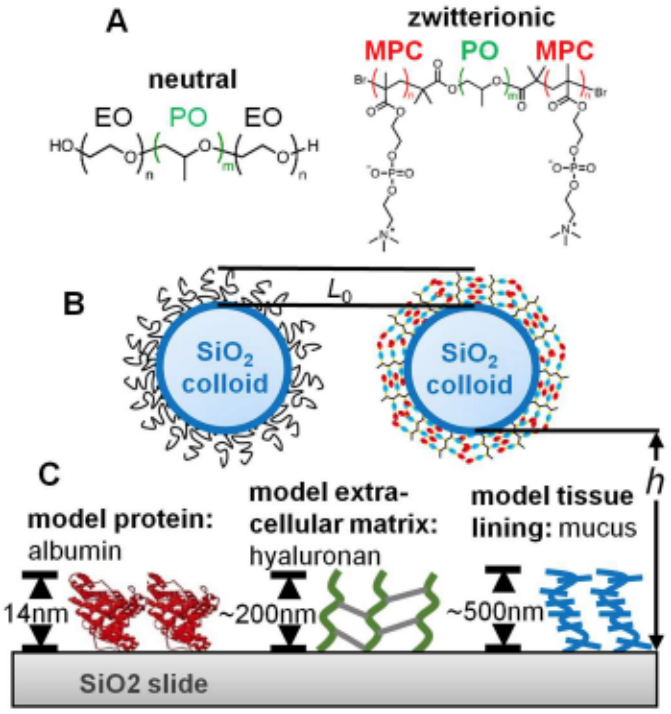

Fig. 5.1 System for studying colloidal stability and interactions between PEO and PMPC coated colloids and biomaterial surfaces. (**A**) PEO-b-PPO-b-PEO and PMPC-b-PPO-b-PMPC block copolymers. (B) Formation of PEO and PMPC coatings from adsorption of block copolymers onto hydrophobic 3.2μm silica colloids. Polymer coating thickness (L_0) was controlled by adsorption of copolymers with varied PEO and PMPC blocks size (n). (**C**) Formation of biomaterial surfaces onto glass slides using bovine serum albumin (BSA), cross-linked hyaluronan, and mucus as model protein, extra-cellular matrix, and mucus surfaces.

5.3.1 Adsorbed polymer coatings

As shown in **Fig. 5.1A-B**, polymer coatings were created from adsorption of amphiphilic block copolymers onto hydrophobic colloids. The copolymers consisted of a hydrophobic poly(propylene oxide) (PPO) block flanked by two PEO or PMPC blocks. PEO copolymers were industrial copolymers generously donated by BASF. PMPC

copolymers were synthesized by collaborators in the Herrera-Alonso lab, with detailed characterization in a previous study.

Both PEO and PMPC copolymers adsorb onto hydrophobic surfaces at high density, adopting a conformation with PPO blocks oriented towards the surface and PEO or PMPC blocks extended into solution as a polymer brush.[49,131,135] The thickness of the adsorbed PEO or PMPC layer increases with increasing molecular weight of the PEO or PMPC blocks (details in **Table 5.1**).[30,131] This strategy thus evaluates the relative impact of non-specific surface interactions (e.g. van der Waals between substrates and compression of polymer or biomaterials) and specific molecular interactions (e.g. enthalpic polymer-biomaterial attraction) on the stability of polymer-coated colloids. In particular, the non-specific colloidal interactions depend chiefly on polymer thickness and colloid radius,[23,24] whereas specific colloidal interactions would depend only on colloidal radius (i.e. surface area of overlap).

The deposition of polymer-coated colloids was tested against model biomaterial surfaces (**Fig. 5.1C**). These biomaterial surfaces consisted of glass slides decorated with either bovine serum albumin (BSA), cross-linked 100kDa hyaluronan, or porcine intestinal mucus, chosen as models of protein, extra-cellular matrix,[136] and mucosal lining[137] surfaces of interest in drug delivery and diagnostic applications.[138] Together, these biomaterial surfaces represent an important variation in not just coating chemistry, but also thickness (L_0) as determined from previous studies in our group.[80,131,139]

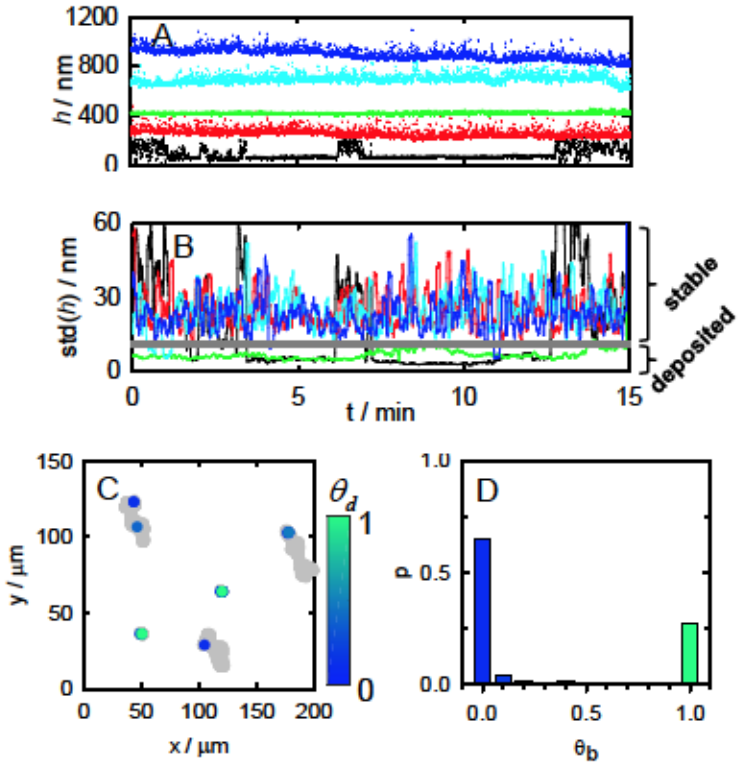

Fig. 5.2 Example determination of binding lifetimes from measured diffusion trajectories. In this example, 21nm PMPC-coated colloids diffusing across BSA-coated glass slides. (**A**) Diffusion trajectories of select colloids normal to the biomaterial surface. The trajectories of each colloid are offset by 200nm for visual clarity. (**B**) Interpretation of deposited or freely diffusing behaviors from diffusion trajectories using a local standard deviation of position h. Standard deviation <12nm was considered deposited. (**C**) Lateral diffusion of the colloids in panels **A**, **B**. Circles indicate stable (gray) and deposited (colored) behaviors. The normalized deposited lifetimes θ_d are color-coded from blue (0.1) to green (1). (**D**) Probability observing a normalized binding lifetime θ_d of all colloids in panels A-C. Histogram bin at θ_d=0 indicates stable diffusion.

5.3.2 Measurement of colloid deposition behavior

Deposition of colloids was assessed by monitoring the diffusion of ensembles of colloids across a biomaterial surface using TIRM. **Fig. 5.2A** shows an example of the normal position (h) over time, i.e. the separation between the colloid and surface, for 5 individual colloids. The profiles for each colloid are offset by 200nm for visual clarity. Three colloids (blue, red, cyan) are freely diffusing, with rapid 20-50nm Brownian fluctuations around their most probable position (h_M). One colloid (green) is permanently

deposited across the 15-min observation, with small fluctuations <5nm around h_M due to measurement error. The last colloid (black) is intermittently deposited, with periods of both large fluctuations (freely diffusing) and also small fluctuations (deposited).

Fig. 5.2B shows quantitative assessment of stable and deposited diffusion behaviors. This plots the local standard deviation in h for each colloid. Stable vs. deposited behavior was assessed using a 12nm cutoff (Eq. (5.4)), which accurately distinguishes between stable (blue, red, cyan), permanently deposited (green), and intermittently deposited (black) colloids.

The analyzed diffusion and deposition behavior is shown qualitatively using lateral diffusion maps in **Fig. 5.2C**. These plot the lateral position of colloids undergoing stable diffusion in gray, with deposition in color from blue (short deposition, θ_d=0.1) to green (permanent deposition, θ_d=1). **Fig. 5.2C** clearly illustrates the qualitative stability of individual colloids, with stable, intermittently deposited, and permanently deposited colloids sampling large, moderate, and small surface areas respectively. The distribution of binding lifetimes for this ensemble of colloids is shown quantitatively in **Fig. 5.2D**, as the probability of observing a scaled deposition lifetime θ_d for all colloids in a measurement. The histogram bin at $\theta_d = 0$ represents the probability of observing stable diffusion. This histogram is highly bimodal, with most observations of either very stable (θ_d~0) or strongly deposited (θ_d~1) behavior, reflecting the polydisperse set of observed behaviors (stable vs. deposited) in **Fig. 5.2B**.

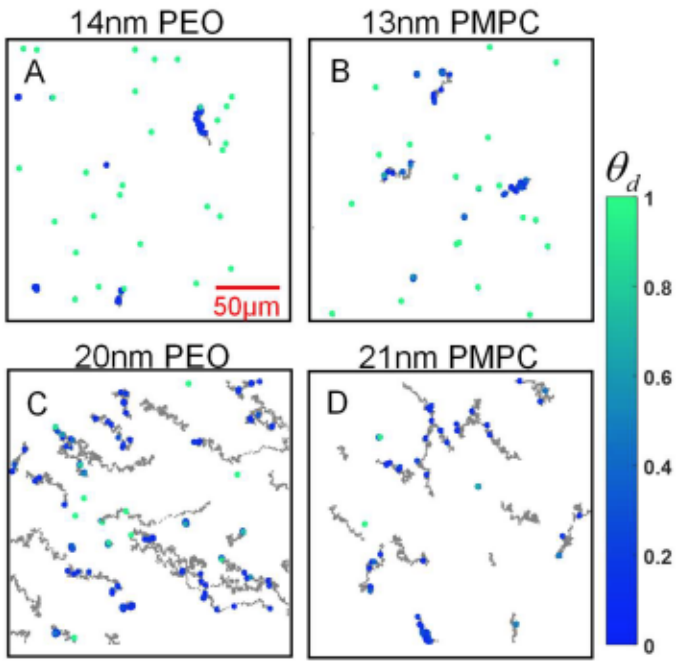

Fig. 5.3 Lateral diffusion trajectories and binding lifetimes of colloids with PEO and PMPC coatings diffusing across a BSA-coated surface. As in Fig. 2C, gray circles indicate stable diffusion, blue-green circles indicate normalized binding lifetimes θ_d. Coating solvated thickness is controlled by varying the PEO or PMPC repeat units of the adsorbed copolymer. (**A**) 13nm-thick PEO (**B**) 12nm-thick PMPC (**C**) 20nm-thick PEO (D) 21nm-thick PMPC.

Fig. 5.3 is a qualitative example that illustrates the impact of the polymer coating's chemistry and thickness on colloidal stability. This plots the lateral diffusion maps of colloids with 13nm or 20nm thick PEO or PMPC against a BSA-coated surface. Again lateral position indicate stable (gray) and bound (colored) diffusion. Colloidal stability is highly dependent on coating thickness, but not polymer chemistry, as colloids with 13-14nm PEO and PMPC are nearly all permanently deposited, and colloids with 20-21nm PEO and PMPC are generally stable.

The dependence of deposition on coating thickness indicates that nonspecific colloidal interactions (e.g. van der Waals substrate interactions, polymer and BSA layer compression) and not specific coating interactions (e.g. BSA-polymer attraction) determine stability. This is evident from several aspects of the deposition behavior. (1)

Specific macromolecular interactions between the protein and polymer would be dependent on polymer chemistry and area of overlap only, and not polymer thickness as observed here. (2) Polymer thicknesses of ~13nm and ~20nm correspond to colloidal van der Waals attractions at BSA-polymer contact of ~3 and ~2kT, which is reasonable for the observed permanently deposited and intermittently deposited behavior. (3) Smaller 1.6μm colloids with a reduced van der Waals attraction of 1kT but equivalent ~20nm polymer thickness demonstrated increased stability.

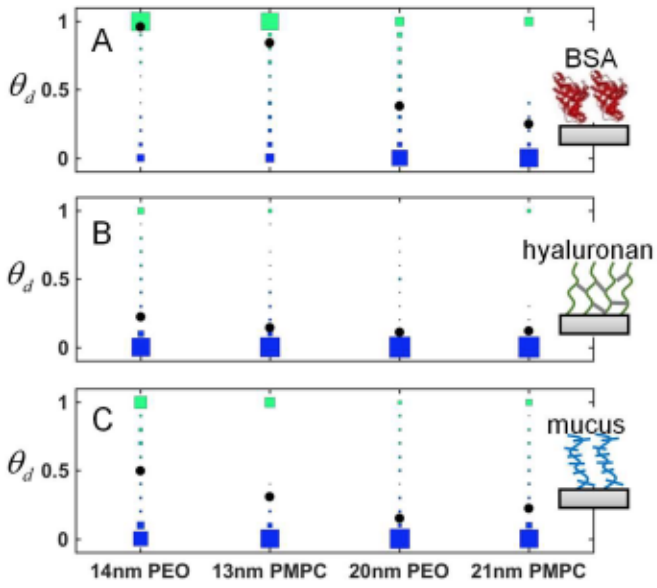

Fig. 5.4 Probability distributions of observing a binding time between 3.2μm diameter colloids with PEO or PMPC coatings and biomaterial coatings. In all plots, the relative probability is indicated by the box area. The normalized binding lifetime θ_d=zero indicates stable diffusion (e.g. an unbound colloid). Black circles indicate the distribution average, $<\theta_d>$. Panels indicate surfaces with (**A**) adsorbed BSA (**B**) grafted hyaluronan (**C**) adsorbed mucus.

5.3.3 Comparison of deposition lifetime distributions

The process of measuring colloid stability, illustrated in **Fig. 5.2-3**, was undertaken for colloids with each polymer coating (PEO or PMPC of L_0 ~13 nm and ~20 nm) against each biomaterial surface (BSA, hyaluronan, mucus). The distribution of measured binding

lifetimes θ_d is shown quantitatively in **Fig. 5.4** for each polymer coating (x axis) and BSA, hyaluronan, and mucus surfaces in panels A, B, and C respectively. Marker areas are proportional to the probability of observing a given binding lifetime for each polymer coating, with the mean binding lifetime of the colloidal ensemble, $<\theta_d>$ indicated by the solid black circles.

As seen in **Fig. 5.4**, θ_d is chiefly influenced by the thicknesses of both the biomaterial and the polymer coating. For diffusion across a given biomaterial, colloids with similar PEO and PMPC layer thicknesses have a similar distribution of binding lifetimes and mean binding lifetime. The influence of polymer layer thickness is greatest for the BSA surface, with generally stable and unstable colloids for layers of ~20nm and ~13nm thickness, respectively.

The dependence of θ_d on polymer and biomaterial thickness again indicates the importance of non-specific colloidal interactions at determining stability. Intermittently deposited states likely occur for net colloid-biomaterial attractions of at least 2kT, which corresponds to net colloid-surface separations of 29nm for the colloids in this study. For the BSA-colloid interactions, this corresponds to strongly deposited behavior for 13nm polymer coatings (~23nm separation, ~4kT) and weakly deposited behavior for the 20nm coatings (~30nm separation, ~2kT), as observed. The hyaluronan and mucus coatings are significantly thicker than BSA, resulting in improved stability. Notably the somewhat improved stability of colloids with hyaluronan (L_0=110nm) relative to mucus (L_0~570nm) is still explained by the dominance of non-specific colloidal interactions, as the cross-linked hyaluronan layer possesses far greater mechanical rigidity than the adsorbed mucus.

Notably, **Fig. 5.4** displays a bimodal distribution of deposition behavior for all combinations of polymer coatings and biomaterial surfaces. This was due to polydisperse colloidal stability at the single-particle level, with colloids that were (1) permanently deposited and (2) either stable or intermittently deposited for each combination of polymer chemistry, polymer thickness, and biomaterial coating.

The polydispersity in colloidal stability is largely attributable to surface heterogeneities in the surface coatings, likely reduced local coating densities and/or thicknesses. Such imperfections would allow colloids further approach to the biomaterial surface when oriented proximal to a local surface defect, and thus experience a greater net attraction and longer potential deposition time. As seen in **Table 5.3**, a significantly higher fraction of single particles were unstable in control experiments of biomaterial-coated colloids diffusing across biomaterial-coated slides than in control experiments of polymer-coated colloids diffusing across polymer-coated slides. Local heterogeneities are thus thought to be primarily caused by heterogeneities in the biomaterial surface coatings. Local surface heterogeneities are the most likely explanation for the colloidal instability of mucus and hyaluronan controls, as (a) the materials are sufficiently thick to otherwise screen the non-specific colloidal attractions and (b) hyaluronan-hyaluronan and mucus-mucus interactions are net-repulsive in 150mM NaCl.

Table 5.3 Stability of colloids diffusing across slides in control experiments with identical coatings on polymers and slides

particle and slide coating	BSA	hyaluronan	mucus	13nm PMPC	21nm PMPC	20nm PEO
% stable colloids	0	76	61	72	92	87

The influence of lateral surface heterogeneities may be mitigated by increased density and thickness of polymer layers, which would have more ability to extend into areas of low monomer density. This may explain the small increases in stability with increasing polymer layer thickness observed against the HA and mucus biomaterials, which are thick enough to otherwise effectively screen the colloidal attractions and provide effective stability. Local defects would also be less problematic for smaller colloids with a reduced van der Waals attraction for the same-size defect. Together, this suggests that, in addition to control of layer thickness to screen non-specific colloidal interactions, effective polymer coatings in biomedical applications must sufficiently robust to provide stability across polydispersity and defects on the various target biological surfaces.

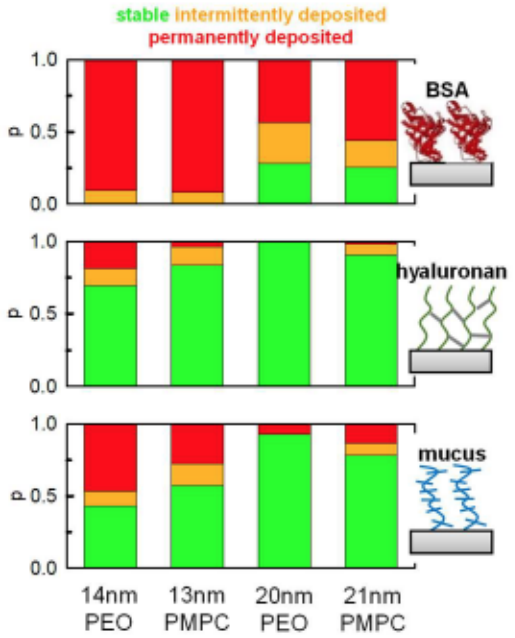

Fig. 5.5 Overall stability of colloids with PEO and PMPC coatings diffusing across biomaterial surfaces. In all panels, the fraction of colloids that are: permanently deposited (red, max(θ_d) for the particle >0.9); intermittently deposited (yellow, max(θ_d) between 0.4-0.9); and stable (green, max(θ_d) <0.4). As indicated, panels are surfaces with adsorbed BSA, grafted hyaluronan, and adsorbed mucus.

5.3.4 Summary of overall colloidal stability

The overall stability of polymer-coated colloids diffusing against biomaterial surfaces is shown in **Fig. 5.5**. Here, individual particles are categorized from their maximum determined binding lifetime $\theta_{d,max}$ as (1) stable, $\theta_{d,max} \leq 0.4$ (green); permanently deposited, $\theta_{d,max} > 0.9$ (red); and intermittently deposited, θ_d between 0.4 and 0.9 (orange). While error bars are not indicated in **Fig. 5.5**, the standard error in determining each probability was between 4-9% as estimated by the binomial distribution.

For diffusion across all biomaterials, the thicker 20-21nm PEO and PMPC coatings have a greater fraction of stable colloids than the 13-14nm coatings. The fraction of stable colloids is also significantly greater for the longer hyaluronan and mucus coatings than for BSA, with equivalent single-particle stability for PEO and PMPC coatings of similar thickness. This is consistent with a dominance of non-specific colloidal interactions, as discussed earlier.

Importantly, the stability in **Fig. 5.5** illustrate significant polydispersity in behavior at the single-particle level. This reflects a fundamentally heterogeneous nature of biological materials and interactions, likely due to both physical heterogeneities in polymer and material architectures (grafting density, polymer molecular weights) as well chemical heterogeneities at a molecular biological level (e.g. glycosylation, charge polydispersities, etc). While the magnitude and impact of such heterogeneities is likely material dependent, polydispersity in biomaterial surface interactions and behavior is likely to increase in a biological setting due the increased variety of material chemistries, properties, and architectures. This illustrates the necessity of using single-particle measurements to understand behavior during engineering and optimization, as colloidal performance in

biomedical applications is typically a non-linear function of the distribution of colloidal behaviors.

5.4 Conclusion

This work evaluated the stability of polymer-coated colloids diffusing across model protein, extracellular matrix, and mucus biomaterial surfaces. Colloids were coated with adsorbed PEO (neutral) and PMPC (zwitterionic) polymers of between 13-21nm thickness to study the relative impact of polymer architecture and polymer chemistry on colloidal behavior. Quantitative interpretation of diffusion trajectories in lateral (across the biomaterial) and normal (separation from the biomaterial) spatial dimensions determined the distribution of colloidal deposition lifetimes at both single-particle and ensemble levels.

For each biomaterial, colloids with PEO and PMPC coatings of equivalent thickness had equivalent deposition and stability. Polydispersity in single-particle colloidal behavior was significant for all polymer and biomaterial coatings, indicating the importance of spatial surface defects at reducing the overall colloidal stability. This demonstrates that, for the well-solvated coatings in this study, non-specific colloidal interactions (which are polymer-thickness dependent) are dominant in determining colloidal stability. The polydisperse colloidal behaviors also reveals the importance in single-particle characterization and understanding of material interactions, especially during performance engineering of materials and devices intended for biomedical settings. Together, the data offer fundamental insights towards colloid and polymer design across a wide range of colloidal stabilization applications including particle-based drug delivery and diagnostics materials.

6 INTERACTION POTENTIALS BETWEEN BIOMATERIAL SURFACES AND COLLOIDS WITH ADSORBED ETHYLENE-OXIDE AND PHOSPHORYLCHOLINE POLYMERS

6.1 Introduction

Materials in physiological and environmental applications are often stabilized against aggregation, deposition, and adsorption by the addition of a solvated polymer 'brush' coating.[1,20,24] Traditionally, poly(ethylene oxide) (PEO) coatings have been favored in physiological settings. More recently researchers have been exploring zwitterionic (ZW) polymers, i.e. those with monomers containing both positive and negative moieties, as bio-inspired alternatives to PEO.[13,56,140] ZW polymer chemistries possess benefits over PEO including enhanced chemical functionality, improved stability against degradation, and salt or pH–dependent behavior (for engineering of solution-responsive 'smart' materials).[49,60,90,141]

Many studies have also reported enhanced stabilization and anti-fouling of ZW surfaces relative to PEO. [4,16,52,53] Such enhanced performance is often attributed to 'super-hydrophilic' properties,[58,97,142] e.g. additionally favorable interactions of ZW monomers with water. However several comparative studies of ZW coatings have reported mixed results,[3,6,60–62] suggesting that there is more to understand than simply segment hydrophilicity. Chapters 4 and 5 of this thesis suggested that the varied findings may be explained by macromolecular-scale architectural differences between conventional and ZW coatings, specifically high extension of ZW layer polymers away from the coated surface. If so, polymer architecture (e.g. thickness, compression mechanics, lateral coating heterogeneities) needs to be studied in conjunction with monomer chemistry to gain an

improved understanding of the stabilization mechanisms of high-performance polymer coatings.

While many physiological applications of colloids require stabilization against aggregation and deposition, much of the understanding of ZW material properties derives from studies of protein adsorption.[11,52,90,126,127] Fewer studies have measured interactions between ZW and biomolecule-based materials, which would provide a more direct probe of interaction mechanisms. For example, Kutnyanszky and Vansco showed similar compression and Young's moduli of a poly-sulfobetaine (ZW) and arginyl-glycyl-aspartic acid (RGD) functionalized poly(methyl methacrylate) under similar grafting conditions.[143] Sakata et al and Schon et al showed a correlation between protein adsorption to polymer surfaces and an atomic microscopy measured pull-off force.[70,144] However none of the studies of biomaterial-polymer interactions that we are aware of have engaged in a systematic variation of both coating architecture and monomer chemistry, and thus did not reveal the important layer properties and interactions that impart stability.[9,55,70,144] Furthermore, studies of polymer-coating interactions are generally mechanical measurements performed at large applied forces.[41,67,69,143] Such mechanical studies lend limited insight into colloidal stability, which is largely determined by the kT-scale interactions between two surfaces.[44,145] A further understanding of the interactions and stability of polymer-coated colloids with biomaterials would aid design of drug delivery and diagnostic materials, as stability (i.e. resistance to deposition or aggregation)- and not just protein adsorption- is a chief in-vitro surrogate of device performance.[54,89]

This chapter reports the interactions of ZW and PEO coated colloids with model biomaterial surfaces to understand the polymer and biomaterial properties that influence

colloidal stability. Colloids are coated with PEO or ZW poly(2-methacryloyloxyethyl phosphorylcholine) (PMPC) coatings of 13-21nm thickness. Biomaterials are created from protein, mucus, and extra cellular matrix components of interest to common drug delivery, diagnostic, and other biomedical device applications. Together, this varies both coating chemistry and architecture (thickness) to probe the relative impact of polymer chemistry (e.g. specific molecular interactions) and architecture (e.g. nonspecific macromolecular compression) on measured interactions. Interactions of stable particles depend chiefly on polymer and biomaterial coating thickness, revealing the importance of non-specific interactions in stabilizing colloids. Single particle analysis reveals a significant role of surface heterogeneity in destabilizing colloids, with polydisperse interactions and stability across all materials and coatings. Together, findings show important aspects of polymer coatings that determine colloidal stability in biomaterial environments and applications.

6.2 Materials and Methods

6.2.1 Polymer synthesis and characterization

PEO and PMPC polymer coatings were formed through adsorption of amphiphilic block copolymers consisting of a polypropylene (PPO) block flanked by hydrophilic PEO or PMPC blocks. Polymers and relevant information are indicated in **Table 6.1**. PEO-b-PPO-b-PEO block copolymers (herein referred to as 'PEO copolymers') were generously donated from BASF. PMPC-b-PPO_{49}-b-PMPC block copolymers (herein referred to as 'PMPC copolymers') were synthesized using activator regenerated by electron transfer-atom transfer radical polymerization (ARGET-ATRP) using a copper catalyst, reported in a previous paper.[131] The thickness (L_0) of the adsorbed PMPC and PEO layers was

determined from measurements of colloidal interaction potentials as previously reported.[131] The free energy / area (f_0) of PMPC and PEO layers was in a hard-wall regime at the kT scale, between 5-10×10^5kT/μm^2.

Table 6.1. Properties of amphiphilic triblock copolymers and their adsorbed polymer brushes on hydrophobic surfaces.

polymer	polydispersity M_w/M_n	coating thickness L_0 / nm
PEO_{76}-PPO_{29}-PEO_{76}	1.1[a]	14
PEO_{141}-PPO_{51}-PEO_{141}	1.2[a]	20
$PMPC_{28}$-PPO_{49}-$PMPC_{28}$	1.1[b]	13
$PMPC_{57}$-PPO_{49}-$PMPC_{57}$	1.4[b]	21

6.2.2 Colloid surface preparation

PEO and PMPC copolymers were adsorbed onto hydrophobic silica colloids. 3.2μm silica colloids (Bangs Laboratories, SS05N) were rendered hydrophobic by coating with octadecyl groups as described previously[132] and stored in ethanol. For adsorption, 2μL of 0.1% v/v hydrophobic silica in ethanol was added to 1mL of 1mg/mL copolymer in deionized water (DI) and mixed for at least 4 hours. Unadsorbed polymer was then removed by at least 5 cycles of centrifugation and re-dispersion in phosphate buffered saline (Fisher, 20-012-043).

Table 6.2. Overview of biomaterial surfaces and surface properties

biomaterial	model of	layer thickness L_0 / nm
bovine serum albumin (BSA)	protein surface, serum	8
100kDa hyaluranon	extracellular matrix (ECM)	110
porcine intestine mucus	mucosal linings (lung, vaginal, intestinal)	570

6.2.3 Biomaterial surface preparation

Glass slides (Fisher, 12-549-3) were cleaned and dried with N_2 as previously reported. To render hydrophobic, dried slides were spin coated with 3% w/w polystyrene in toluene at 3k RPM for 1 minute. To present NH_2, dried slides were added to 2% v/v 3-aminopropyl triethoxysilane (APTES, Sigma, 440140) in toluene for 16 hours at room temperature. After APTES reaction, the NH_2-presenting slides were sequentially rinsed with toluene, isopropanol, DI, dried with N_2, and baked at 80°C for 1 hour. Batch cells for microscopy were prepared on polystyrene or NH_2 slides by addition of 0.5mm viton orings sealed with vacuum grease.

Bovine Serum Albumin (BSA, Sigma-Aldrich, A2058) and porcine mucus (Sigma-Aldrich, M1778) were physisorbed onto hydrophobic polystyrene glass slides. BSA and mucus solution were dissolved at 1mg/mL in PBS and filtered through a 0.22μm cellulose acetate syringe filter (Fisher, CAS022550). Filtered BSA or mucus solution was then added to the batch cells on polystyrene slides for adsorption over at least 4 hours. 100 kDa hyaluronan (R&D Systems, GLR004) was chemisorbed onto dried NH_2-presenting slides using carbodiimide chemistry. 3mg/mL hyaluronan, 0.05M N-hydroxysuccinimide (NHS,

Fisher, AC157270250) and 0.05M *N*-(3-Dimethylaminopropyl)-*N'*-ethylcarbodiimide hydrochloride (EDC, Sigma-Aldrich, E6383) were prepared in 150mM NaCl, 10mM HEPES, pH 6.0 buffer. The hyaluronan-EDC-NHS solution was then immediately added to batch cells on NH_2-presenting slides for reaction with the amine and crosslinking. Unbound BSA, mucus, or hyaluronan were removed by washing batch cells with filtered PBS, and sealed with a glass coverslip after particle addition. The BSA, mucus, and hyaluronan surface properties are listed in **Table 5.2**, with coating thickness and free energy per area (L_0 and f_0 in Eq.s (6.9)-(6.10)) determined from colloidal interaction measurements in SI.

6.2.4 TIRM Microscopy

Total internal reflection microscopy (TIRM) recorded ensembles of colloids diffusing across biomaterial surfaces. Details are described in previous publications.[44,108,133] Briefly, videos of diffusing colloids were collected using an optical microscope (Axioplan 2, Zwiss) equipped with a 40× optical objective (LD Plan-NEOFLUAR) and charge coupled device (CCD) camera (ORCA-ER, Hamamatsu) at 4 binning and 30 millisecond recording rate. Samples were illuminated by exciting an evanescent wave with 113 nm decay length on a 68° dovetail prism using a 633 nm HeNe laser (Melles Griot). The biomaterial surface was optically coupled to the dovetail prism, with colloids dispersed in solution above the biomaterial surface scattering light from the evanescent wave. Video images of colloidal scattering were analyzed with custom Fortran software to determine lateral position (~100 nm resolution) and scattering intensity of each colloid over time. The relative separation of each colloid from the slide, h-h_M was determined from the colloid's scattering intensity I with ~1 nm resolution using

$$I(h) = I_0 \exp\left[-\beta^{-1}\left(h(t) - h_M\right)\right] \quad (6.1)$$

where h is the height of the particle above the slide, I_0 is the most-probable scattering intensity at colloid-slide contact (at $h = h_M$), and β is the evanescent wave decay length (113 nm).

6.2.5 Diffusion analysis and binding lifetime

The diffusion trajectories of colloids were analyzed to determine the distribution of lifetimes for which each colloid was deposited to a surface, following previous approaches.[112,123,134] This measured the variance in height fluctuations for a given colloid across every 100 height measurements, and labelled the colloid as 'deposited' when the variance was less than a given length,

$$\mathrm{var}\left(h_i, h_{i+1} \ldots h_{i+100}\right) t_{FD} < 2l^2 \quad (6.2)$$

Measurements used l = 8 nm, approximately twice the standard deviation of signal of a motionless particle (i.e. a particle with height fluctuations attributable only to noise). Colloids were determined to be freely diffusing, reversibly deposited, or permanently deposited if the longest observed deposition occurred over less than 3seconds, between 3 and 60 seconds, or greater than 60 seconds respectively (see Ch. 5.2.5 for determination).

6.3 Theory

Ensemble TIRM measured nm-scale diffusion of colloids adjacent to biomaterial surfaces. Brownian fluctuations in colloidal-surface separation were interpreted to build a height probability distribution, $p(h)$. The potential energy profile, $U(h)$, was estimated using the Boltzmann relation,

$$\frac{U(h)-U_{\mathrm{M}}(h_{\mathrm{M}})}{kT}=\ln\left(\frac{p_{\mathrm{i}}}{p_{\mathrm{M}}}\right) \tag{6.3}$$

where indexes "i" and "M" represent any bin and the most probable bin respectively, k is Boltzmann's constant, and T is absolute temperature. Potential energy profiles of colloids were modeled as a function of relative height h-h_{M} above the planar surface using a superposition of gravitational (G), van der Waals (vdW), and polymer compression (P) potentials as,

$$U(h)+U_{\mathrm{G}}(h)=U_{\mathrm{G}}(h)+U_{\mathrm{vdW}}(h)+U_{\mathrm{p}}(h) \tag{6.4}$$

Contributions from electrostatic double layers were negligible due to the high solution ionic strength (150mM) media and low surface charge of colloids (-1±4mV). The gravitational potential energy is given by,

$$U_{\mathrm{G}}(h)=\frac{4}{3}\pi a^{3}\left(\rho_{\mathrm{p}}-\rho_{\mathrm{f}}\right)gh \tag{6.5}$$

where a is particle radius, ρ_{p}-ρ_{f} is the difference in particle and fluid densities, and g is the gravitational constant. The gravitational contribution to the net interactions was used to fit the colloid radius. van der Waals and polymer contributions to the net colloidal interaction were modeled using the Derjaguin approximation to obtain sphere-plate potentials from flat-plate interactions,

$$U(h)=2\pi a\int_{h}^{\infty}E(l)dl \tag{6.6}$$

where $E(l)$ the energy per unit area between flat plates at a separation, l, for the interaction of interest.

Van der Waals interactions between a sphere and flat surface, Eq. (6.6) is well approximated by a power-law expression,

$$U_{\mathrm{vdW}}(h) = 2\pi a \int_{h}^{\infty} \frac{A_{132}(l)}{12\pi l^2} \cong Aah^{-2} \tag{6.7}$$

where A is an effective Hamaker constant between silica-water-polystyrene, and fit to Lifshitz theory calculations of the Hamaker function $A_{132}(l)$ by Bitter et al.[75]

The energy per area for interactions between polymer layers coating on two flat plates can be represented as,

$$E(l) = f_1(L_1) - f_1(L_0) + f_2(L_2) - f_2(L_0) \tag{6.8}$$

where $f_i(L)$ is the free energy per area of the polymer layer on surface i at compressed thickness L, and L_0 is the uncompressed polymer layer thickness (so that $f_{0,i}=f_i(L_0)$). At small compressions ($L/L_0>0.5$) and minimal interpenetration between polymer layers, a rigorous expression for $f(L)$ from Milner et al[22] can be expressed as an exponential decay.[80] For the case of interactions between identical polymer coatings ('symmetric polymer interactions', i.e. $L_{0,1}=L_{0,2}$ and $f_1(L)=f_2(L)$) the polymer-polymer potential is given by,

$$U_{\mathrm{p}}(h) \cong 16\pi a \frac{\alpha}{\beta} f_0 L_0 \exp\left(\frac{-\beta h}{2L_0}\right) \tag{6.9}$$

where the constants α, β are 10.6 and 7.38 respectively for the parabolic monomer concentration profile from Milner et al.[22] For the case of different polymer coatings on the adjacent surfaces (asymmetric polymer interactions), the net potential is given by,

$$U_{p,A}(h) = 8\pi a \Lambda_1^{\lambda_{0,1}/(\lambda_{0,1}+\lambda_{0,2})} \Lambda_2^{\lambda_{0,2}/(\lambda_{0,1}+\lambda_{0,2})} \left(\lambda_{0,1}+\lambda_{0,2}\right) \exp\left(-\frac{h\gamma}{\lambda_{0,1}+\lambda_{0,2}}\right) \tag{6.10}$$

in which $\lambda_i = L_{0,i} / \beta$ and $\Lambda_i = \alpha f_{0,i}$.

Finally, individual height measurements each have an error which distorts the measured histogram. The contribution of this point measurement error on the theoretical

height distribution was accommodated using convolution of a Gaussian probability, $g(l)$, with standard deviation, ξ, with the Boltzmann height distribution as,

$$p_c = \int p_T(h)\, g(h-l,\zeta)\, dl \tag{6.11}$$

where ζ is used within a narrow range of 8-11 nm as estimated from intensity fluctuations of deposited particles (that should yield a delta function without measurement error). The theoretical potential with measurement error is then calculated from the convoluted probability distribution (p_c) using Eq. (6.3).

6.4 Results & Discussion

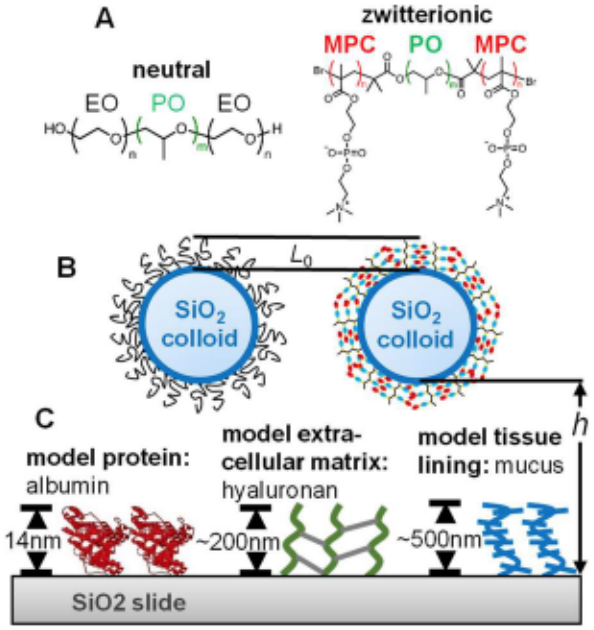

Fig. 6.1. System for measurement of interactions biomaterial surfaces and colloids with PEO or PMPC polymer coatings. (**A**) PEO-b-PPO-b-PEO and PMPC-b-PPO-b-PMPC triblock copolymers. (**B**) PEO and PMPC coatings formed by copolymer adsorption onto hydrophobic silica. Polymer layer thickness L_0 is controlled by adsorption of copolymers with varied PEO and PMPC blocks size as characterized previously and reported in **Table 6.1**.[131] (**C**) Colloidal interactions are measured with adsorbed bovine serum albumin (BSA), cross-linked hyaluronan, and adsorbed mucus biomaterials surfaces on glass slides. Biomaterial layer parameters are reported in **Table 6.2**, with determination of biomaterial parameter discussed in SI.

6.4.1 Polymer interaction measurements

This work measured the interactions between biomaterial surfaces and colloids with adsorbed PEO and PMPC polymer coatings. As indicated in **Fig. 6.1A-B**, polymer coatings were formed from adsorption of ABA triblock copolymers onto hydrophobic surfaces. Polymers consisted of a hydrophobic polypropylene (PPO) block flanked by hydrophilic PEO (neutral) or PMPC (zwitterionic), and adsorbed onto hydrophobic surfaces with PEO or PMPC extended to form brush architectures. Polymer layers of 13-21 nm thicknesses were formed by adsorbing copolymers of varied PEO and PMPC block molecular weights, as studied in Chater 4.[131] Interactions were measured of polymer-coated colloids against model biomaterial surfaces (**Fig. 6.1C**) that consisted of physisorbed bovine serum albumin (BSA), chemisorbed 100kDa hyaluronan, or physisorbed porcine intestinal mucus. BSA, hyaluronan, and mucus were chosen as they are major components of plasma proteins, extra-cellular matrix, [136] and mucosal tissue linings,[137] which are of interest in drug delivery and diagnostic applications. The biomaterial coatings represent thicknesses of 8-570nm (**Table 6.2**), as characterized by measurements of interaction potentials (details in SI).

Together, the polymer and biomaterial surface coatings represent an important variation in not just molecular chemistry but also macromolecular layer thickness (L_0) and compression mechanics (f_0).[80,131,139] Varying both layer chemistry and mechanical properties allows interrogation of the relative contribution of both specific molecular and non-specific colloidal interactions. In particular, the specific molecular-scale polymer-biomolecule interactions should be dependent only on the area of overlap between a colloid and biomaterials surface (e.g. the colloid's radius). In contrast, the non-specific colloidal interactions (van der Waals and polymer compression and overlap) should depend on

polymer and biomaterial thickness (with increasing thickness stabilizing the colloids by screening van der Waals interactions) as well as colloid radius (via the Derjaguin approximation, Eq. (6.6)).[22,73]

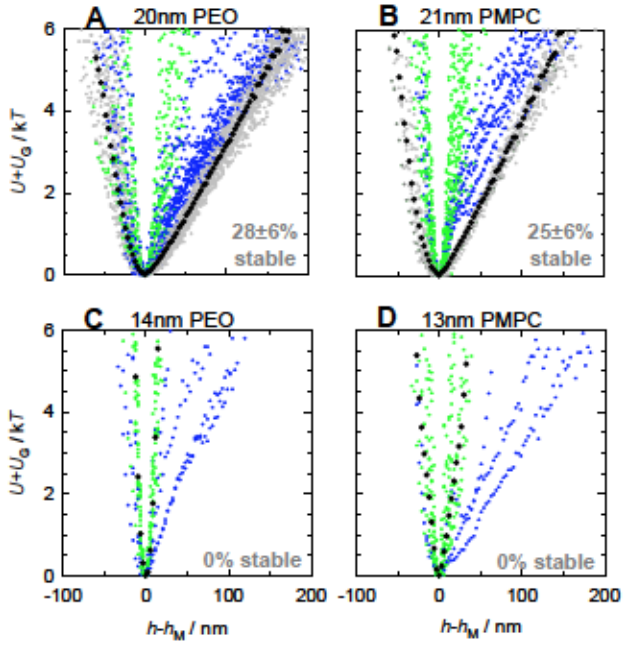

Fig. 6.2 Interaction measurements between PEO and PMPC-coated 3μm silica colloids and BSA-coated slide. In all panels, net interaction potential $U+U_G$ versus relative height $h-h_M$. Single particle interaction are coded gray, blue, and green to represent colloids that were freely diffusing (stable), reversibly deposited, and permanently deposited respectively. Black circles are the average interaction of the most representative particles. Text reflects the percent of particles determined to be stable, with standard deviation estimated from the binomial distribution. (**A**) 20nm PEO coating vs. BSA. (**B**) 21nm PMPC coating vs. BSA. (**C**) 14nm PEO coating vs. BSA. (**D**) 13nm PMPC coating vs. BSA.

6.4.2 Single-particle interactions with BSA

Interaction measurements of polymer-coated colloids with BSA-coated slides are depicted in **Fig. 6.2**. Panels represent colloids with polymer coatings of 20nm PEO, 21nm PMPC, 14nm PEO, and 13nm PMPC. A variety of behaviors are observed across individual colloids, including free diffusion (gray), reversible deposition (blue), and permanent deposition (green). Particles with the thicker 21nm PMPC and 20nm PEO

coatings have equivalent stability (15±4/59 vs. 18±3/64 freely diffusing with standard error estimated from the binomial distribution). Particles with thinner 13-14nm coatings are much less stable, with no freely diffusing particles and only 3/32 (13nm PMPC) and 2/25 (14nm PEO) colloids reversibly deposited.

The freely diffusing, reversibly deposited, and permanently deposited colloidal behaviors reflect colloids with increasing net attraction respectively to the BSA surface, as is evident from the measured potentials. Freely diffusing particles have generally broad potentials that indicate sampling of a wide range of heights normal to the BSA surface, and a sharp repulsive contribution from polymer-BSA overlap and compression at negative h-h_M. At the other extreme in behavior, permanently deposited colloids are observed that exhibit very narrow energy wells. This reflect Brownian excursions within a narrow and strongly-attractive energy well, as expected for permanently deposited particles. The reversibly deposited colloids have a range of polydisperse potentials in between the two extremes of free diffusion and permanent deposition, reflecting mild but reversible attraction.

The improved stability of colloids with the thicker polymer coatings is an indication of a reduced net colloid-surface attraction. Estimates of the polymer interaction parameters (L_0 and f_0 in Eq. (6.9)-(6.10)) were obtained by fitting the symmetric interaction potentials (i.e. separately fitting interactions for BSA coated slides and colloids, and 20nm PEO coated slides and colloids) as shown in the SI (Fig S6.1). Using layer parameters to estimate the asymmetric polymers interactions (using Eq. (6.7) and (6.10)) indicates approximately 2kT vs 3kT net attractive wells for the 20-21nm and 13-14nm polymer layers, respectively, upon polymer-BSA contact. The 2kT surface attraction for colloids with the 20-21nm

layers may be expected to cause very short and reversible deposition over the 15 min time scales of our experiments, as is generally observed. The 3kT attraction for the 13-14nm coatings would lead to longer deposition lifetimes relative to the 20-21nm coatings, as is also observed. However the 3kT attraction should likely cause reversible deposition, whereas permanently deposited colloids are generally observed for the 13-14nm coatings.

The deposition behaviors of the individual colloids in **Fig. 6.2** correspond to generally increased attraction than predicted using Eq. (6.7) and (6.10). One explanation is that significant polymer interpenetration and compression leads to colloids approaching the surface at reduced separations than estimated using Eq. (6.10). However chain-chain interpenetration is typically considered to be inconsequential for the dense, well solvated polymer layers in our study.[146,147] Furthermore, independent measurements of symmetric interactions indicate that the PEO, PMPC, and BSA layers only reach between 5-10% compression in the kT scale of our measurements, which would have a small effect on the net measured colloidal attraction.

Another explanation for increased colloidal attraction with the BSA surface is the presence of specific molecular BSA-polymer attractions that would increase the net colloidal attraction during BSA-PEO and BSA-PMPC overlap. However such interactions would be expected to depend on polymer chemistry, and not thickness, whereas the measured single-particle stability depends on polymer thickness but not chemistry. In addition, both PEO and PMPC surfaces have been shown to reject the serum proteins during adsorption studies.[144,148]

A more likely explanation is the presence of significant lateral heterogeneities in the BSA and/or polymer layers. Lateral heterogeneities may be expected to cause spatially-

localized reductions in polymer or biomolecule size and density, reducing the local repulsion of the BSA or polymer layer and increasing the net attraction for colloids oriented proximal to such defects. Such defects would also increase the polydispersity of observed interactions at the single-particle level, explaining the highly polydisperse single-particle behaviors in **Fig. 6.2A-D**. Control experiments of symmetric PEO-PEO and PMPC-PMPC interactions generated between 76-88% freely diffusing particles depending on polymer thickness. We thus expect particle destabilization to be caused by surface defects in all of the BSA, PEO, and PMPC polymer layers.

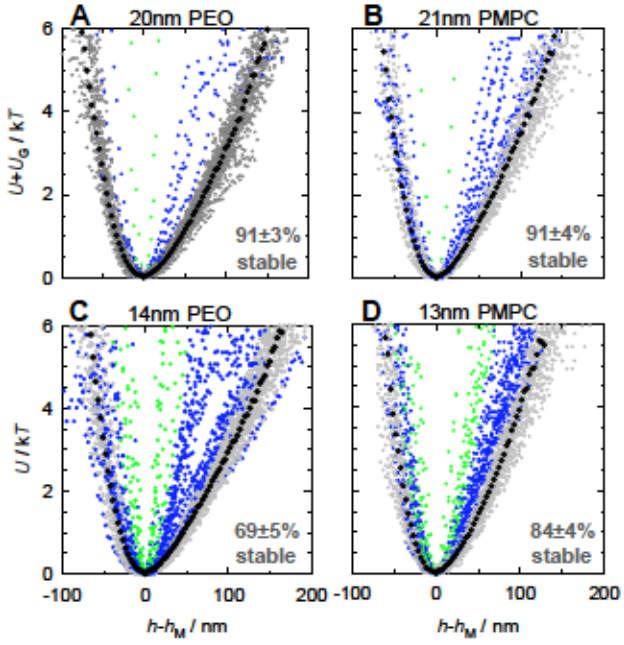

Fig. 6.3 Interaction measurements between PEO and PMPC-coated 3μm silica colloids and a hyaluronan-coated slide. In all panels, net interaction potential $U+U_G$ versus relative height $h-h_M$. Single particle interaction are coded gray, blue, and green to represent colloids that were freely diffusing (stable), reversibly deposited, and permanently deposited respectively. Black circles are the average interaction of the most representative particles. Text reflects the percent of particles determined to be stable, with standard deviation estimated from the binomial distribution. (**A**) 20nm PEO coating. (**B**) 21nm PMPC coating. (**C**) 14nm PEO coating. (**D**) 13nm PMPC coating.

6.4.3 Single-particle interactions with hyaluronan and mucus

The interactions of PEO and PMPC coated colloids with hyaluronan are depicted in **Fig. 6.3**. Single-particle behaviors are also polydisperse, including freely-diffusing (gray), reversibly deposited (blue), and permanently deposited (green) behaviors. However the distribution of single-particles exhibits less polydispersity in both potentials and behaviors than those of the BSA-polymer interactions in **Fig. 6.2**. For all polymer coatings, individual colloids are also more stable against the hyaluronan than BSA surfaces, with a much larger fraction of freely diffusing colloids. The fraction of freely diffusing colloids is also greater for colloids with the thicker 20nm PEO and 21nm PMPC coatings (49/54 and 62/68 colloids, respectively) than with the thinner 13nm PMPC and 14nm PEO coatings (66/79 and 52/75 colloids, respectively).

The increased stability of colloids interacting with hyaluronan vs. BSA are largely explained by the greater hyaluronan coating thickness (8nm vs. 120nm). Hyaluronan can be expected to exert significant polymer repulsion well past the 50nm of colloid-slide separation where the colloidal van der Waals attractions are <1kT. Longer-ranged hyaluronan interactions are evident in the measured potentials, which exhibit polymer repulsion from h-h_M between -90nm and 20nm for stable colloids with all polymer coatings.

The deposited colloids in **Fig. 6.3** are somewhat surprising as the thick hyaluronan layer effectively screens colloidal van der Waals interactions to less than 1kT. Again, additional sources may increase the apparent colloid attraction. Specific molecular hyaluronan-polymer interactions would be dependent on polymer chemistry and independent of thickness. Specific hyaluronan-polymer interactions are thus unlikely as the

experimentally measured single-particle stability and polydispersity depend on polymer thickness (13-14nm vs 20-21nm) but not polymer chemistry (PEO vs. PMPC).

Instead, lateral defects in the hyaluronan and/or PEO and PMPC coatings likely cause spatially-dependent destabilization of colloids. Such defects would be somewhat mitigated by a thicker PEO or PMPC layer, with an increased capacity of thicker polymer layers to 'fill in' lateral coating gaps. This agrees with the increased stability observed for colloids with 20nm PEO and 21nm PMPC coatings (62/68 and 49/54 freely diffusing colloids, respectively) relative to the 14nm PEO and 13nm PMPC coatings (53/75 and 59/79 respectively).

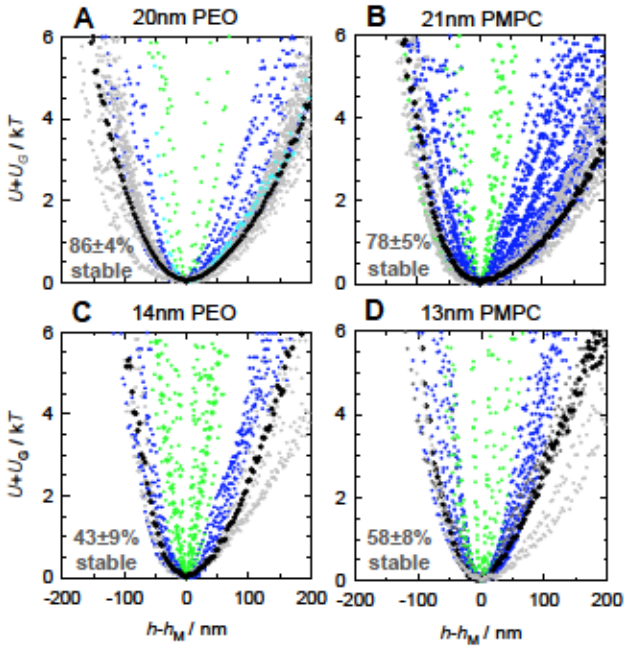

Fig. 6.4 Interaction measurements between PEO and PMPC-coated 3μm silica colloids and mucus-coated slide. In all panels, net interaction potential $U+U_G$ versus relative height $h-h_M$. Single particle interaction are coded gray, blue, and green to represent colloids that were freely diffusing, reversibly deposited, and permanently deposited respectively. Black circles are the average interaction of the most representative particles. Text reflects the percent of particles determined to be stable, with standard deviation estimated from the binomial distribution. (A) 20nm PEO coating. (B) 21nm PMPC coating. (C) 14nm PEO coating. (D) 13nm PMPC coating.

Colloidal interactions with mucus demonstrate very thick mucus layers, with repulsive contribution to potentials spanning ~200nm. Single-particle potentials for colloids with all polymer coatings are highly disperse, with a greater fraction of freely-diffusing particles for the 13-14nm polymer coatings than the 20-21nm polymer coatings. Polydispersity is also observed across the freely-diffusing potentials. As for the BSA and hyaluronan surfaces, polydispersity of the mucus interactions is largely attributed to surface heterogeneities in the mucus layer. The reduced stability of colloids interacting with the mucus vs. hyaluronan layer is likely due to a combination of the surface heterogeneities, as reduced resistance to compression (i.e reduced f_0) discussed in the following section.

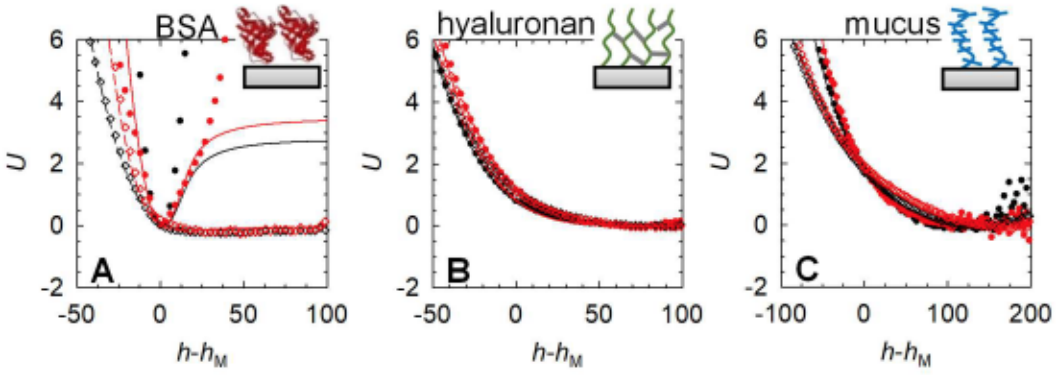

Fig. 6.5 Ensemble-average surface interactions *U* between colloids and biomaterial surfaces. In all panels, 20nm PEO (black diamond), 21nm PMPC (red diamond), 14nm PEO (black circle), 13nm PMPC (red circle). Measured (points) with fit to theory (lines) of Eq. (6.7) and Eq. (6.10) using L_0 and f_0 of the biomaterial layer as adjustable parameters.

6.4.4 Ensemble-average interactions

While the single-particle analysis of interactions in **Fig. 6.2**-**Fig. 6.4** reveals important aspects of colloidal polydispersity and layer heterogeneity, analysis of the ensemble interactions reveals important mechanisms of the polymer and biomaterial

interactions and compression. The ensemble average interactions from **Fig. 6.2**-**Fig. 6.4** (black circles) are plotted in **Fig. 6.5**, now with the gravitational contribution (U_G) subtracted to better isolate the contribution of polymer and van der Waals surface interactions on the net potentials. Ensemble averages are formed from sets of freely diffusing particle to mitigate any bias from surface defects. The exception is for the 13-14nm coated colloids with BSA, for which the permanently deposited colloids are the most representative interaction. All panels plot colloids with 14nm PEO (black circles), 13nm PMPC (red circles), 20nm PEO (black diamonds), and 21nm PEO (red diamonds).

For interactions with BSA (**Fig. 6.5A**), colloids with PEO and PMPC coatings of similar thicknesses exhibit nearly identical interaction, with very different potentials for layers of different thickness. This is consistent with the non-specific macromolecular model of polymer interactions, as the similar thicknesses (L_0 ~10nm) and free energies (f_0~10^5kT/μm^2) of the BSA and polymer coatings lead to compression of both layers during interaction. The polymer thicknesses are also of a size where the colloids are expected to experience a very different net attraction well at initial overlap between the BSA and polymers, as seen by the predicted potentials (lines) using the fit parameters in **Table 6.3** and Eq. (6.7) and (6.10) (and as discussed earlier).

Ensemble interactions of freely diffusing colloids with hyaluronan are depicted in **Fig. 6.5B**. Potentials demonstrate a much longer-range polymer repulsion across ~80nm, consistent with the ~120nm thick hyaluronan layer. Here, the ensemble colloidal interactions show a clear overlap for all polymer coatings irrespective of polymer layer thickness. This is consistent with the macromolecular interaction model, as the hyaluronan coating is much thicker than the PEO and PMPC polymer coatings, and has a significantly

reduced resistance to compression (e.g. f_0 for hyaluronan is 100-fold less than f_0 for PMPC and PEO). Hyaluronan compression mechanics thus dominate the net polymer interactions, resulting in very similar interactions for all of the polymer coatings.

Ensemble interactions with mucus (**Fig. 5C**) occur over approximately a 300nm distance, consistent with the ~570nm thickness in **Table 6.2**. The long-range mucus layer interactions indicate a very low resistance to compression, with a very low f_0~25kT/μm^2. Such high compressibility is likely a result of both physical properties of the mucus layer as well as a lower graft density of mucus layers. A lower surface density of mucus polymer may largely influence the significant polydispersity of single-particle behaviors for mucus, with small local fluctuations in mucus surface concentration creating sparse or bare surfaces.

All of the ensemble colloidal interactions in **Fig. 6.5A-C** are well represented by fits to theory (lines). Fits were created by adjusting L_0 and f_0 in Eq. (6.10) for the biomaterial layer only, and using previous measurements of PEO and PMPC parameters in **Table 6.1** from Ch 4. For all conditions, fit biomaterial layer L_0 and f_0 are within 10% of the values determined from symmetric experiments (**Fig. 6.6**). The sole exception is for the mucus interactions with 13-14nm PEO and PMPC layers, which determined a L_0 of 380nm (approximately 40% below the fit values in **Fig. 6.6**). However the 13-14nm PEO and PMPC interactions demonstrated significant polydispersity at the single-particle level, with significant variance among even the freely diffusing particles. It is thus likely that the lower fit L_0 for 14nm PEO and 13nm PMPC are due to relative destabilization of the colloids with 13-14nm polymer coatings relative to colloids with the 20-21nm coatings, causing poorly determined ensemble average potentials or tethering effects.

The macromolecular description of polymer and biomaterial interactions successfully describes the net colloidal interactions in **Fig. 6.5**, providing further evidence that interactions between the polymer and biomaterial layers are largely dominated by the polymer compression mechanics. This suggests that, for the well-solvated polymer chemistries in our study, layer stabilization and antifouling properties are largely determined by properties of the polymer layer architectures, especially architectural thickness and lateral grafting heterogeneities. Together, this suggests that the somewhat conflicting studies of antifouling and stabilization polymer performance in the literature may be due to differences in layer properties during comparison, especially thickness, graft density, and grafting defects.

Table 6.3 Biomaterial parameters determined by fitting the ensemble-average polymer interaction potentials to Eq. (6.10) in **Fig. 6.5**

	BSA		HA		mucus	
	L_0/nm	f_0/kT μm^{-2}	L_0/nm	f_0/kT μm^{-2}	L_0/nm	f_0/kT μm^{-2}
13nm PMPC	6	10^5	110	1000	310	20
14nm PEO	6	10^5	135	1000	350	20
20nm PEO	6	10^5	125	1000	650	20
21nm PMPC	6	10^5	110	1000	580	15

6.5 Conclusion

This work measured the interaction potentials and colloids with PEO and PMPC (ZW) polymer coatings interacting with model biomaterial surfaces. For a given biomaterial, colloidal interactions and stability were equivalent for PEO and PMPC

coatings of similar thicknesses. For all combinations of polymer coatings and biomaterials, individual colloids exhibited polydisperse stability with freely diffusing, reversibly deposited, and permanently deposited behaviors. The fraction of stable (freely diffusing) colloids increased with both increasing biomaterial and polymer coating thicknesses, with corresponding changes in the measured colloidal potentials. Ensemble-average potentials from freely diffusing particles agreed with estimates from colloidal theories of polymer and van der Waals interactions. The polydispersity in single-particle behaviors and interactions is thus largely attributable to lateral surface heterogeneities and defects in both polymer and biomaterials surfaces.

Together, these findings indicate that the colloidal interactions and stability are dominated by a combination of macromolecular interactions from the polymer layer (e.g. layer thickness and compression mechanics) and lateral defects. Increasing the polymer layer thickness improves colloidal stability by both screening attractive colloidal (e.g. van der Waals) attractions and mitigating surface defects. This offers evidence that, at least for well-solvated polymers such as PEO and PMPC ZW in this study (and typically preferred for anti-fouling applications), design of effective polymer coatings for colloidal stabilization applications should focus on optimization of layer architecture (e.g. thickness and lateral homogeneity) and not specific monomer chemistry. The polydisperse behavior of individual colloids also highlights the importance of single-particle studies during material optimization to understand polydispersity effects, as performance in many colloidal applications is a non-linear contribution of the various colloidal behaviors. Together, the data offer fundamental insights towards colloid and polymer design across a

wide range of applications including the design of antifouling materials and colloidal drug delivery.

6.6 Supplemental Information

Colloidal interaction measurements and dynamic light s scattering were used to characterize the thickness biomaterial coatings onto colloids. **Fig. 6.6** shows the ensemble-average colloidal interactions of symmetric systems, i.e. with the same biomaterial coating on both the colloid and planar substrate. Hyaluronan (red) and mucus (black) are measured on 3.2 μm nominal diameter colloids. BSA is measured on a 1.6μm colloid, as the BSA layer (with thickness ~8nm) was too thin to effectively stabilize 3 μm colloids. All ensembles were created from at least 10 total colloids.

The measured interactions in **Fig. 6.6** were used to estimate the steric layer thickness (L_0) and uncompressed free energy per area (f_0) in Eq. (6.9), as reported in **Table 6.2**. The fit L_0 indicate increasing thickness from BSA (9nm), hyaluronan (110nm), and mucus (570nm). These thicknesses agree within 10% of fit layer thicknesses in asymmetric measurement of interactions between polymer-coated colloids and biomaterial-coated planar substrates, **Table 6.3**. The measured BSA and mucus thicknesses are within 20% of the hydrodynamic thicknesses from DLS. The hyaluronan hydrodynamic thickness was not able to be obtained, as the carbodiimide reaction created particles of insufficient monodispersity for quantitative interpretation.

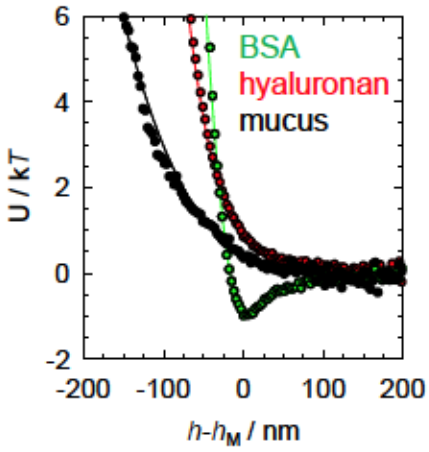

Fig. 6.6. Ensemble-average colloidal interactions of biomaterial-coated colloids with biomaterial-coated slides. BSA with 2.1um colloids (green), hyaluronan with 3.2um colloids (red), mucus with 3.2um colloids (black). Measured (points), and fit to $U=U_P+U_{vdW}$ (Eq. (6.7)+(6.9), lines) using L_0 and f_0 as adjustable parameters.

7 EFFECT OF SODIUM CHLORIDE ON ZWITTERIONIC POLYMER INTERACTIONS AND ARCHITECTURES

7.1 Introduction

Zwitterionic (ZW) polymers have largely drawn attention due to studies claiming improved stabilization and antifouling performance for ZW polymers over traditional poly(ethylene oxide) (PEO) based materials. The previous chapters of this thesis showed that the ZW poly[2-(methacryloyloxy)-ethyl phosphorylcholine] (PMPC) required a fraction of the repeat units to generate equivalent interactions and stability as PEO materials. This difference in interactions and stability was the cause of highly extended PMPC coating architectures, and that PEO and PMPC layers had equivalent interactions and stability when compared by the solvated polymer thickness. The current chapter uses studies of ZW polymers interactions and architectures to understand the molecular mechanisms causing the ZW brush extension.

Most studies of ZW polymer properties have focused on a molecular-level understanding of interactions and solution behavior. ZW polymers generally possess increasing aqueous solubility and expanded chain dimensions upon increasing salt concentration.[49,63,64,141,149–151] This salt-dependent behavior is generally termed the 'anti-polyelectrolyte' effect, and is caused by the screening of attractive dipole-dipole interactions by salt molecules from the solution.[151,152] Anti-polyelectrolyte behavior has been shown in several experimental studies of the effect of salt on polymer solubility, solution quality,[109,141,151,153] and architectures on surfaces.[63,65,130]

The sensitivity of a given ZW polymer to salt depends on both its dipole moment and specific monomer chemistry. In a recent neutron reflectivity study, Higaki et al

demonstrated that sulfobetaine sidechains with increased spacer length between the sidechain's positive and negative charges were more extended in low-salt solutions.[149] At high salt, all of their tested sulfobetaine chemistries were at similar extension relative to their dry state. Interestingly, some ZW polymers such PMPC are unaffected by NaCl.[72,106,109,154] However, the mechanism for this salt independence remains unclear. It may be due to specific chemical or solvation effect as, by simply reversing the PMPC sidechain orientation from phosphate-amine to amine-phosphate, the reverse-PMPC displays a strong sensitivity to dissolved salt.[155]

Despite the extensive studies of ZW polymers, the effect of salt on the interactions of ZW polymer-coated surfaces is still poorly understood. The previous measurements of ZW brush interactions have been mechanical measurements at high applied forces and polymer compression.[9,67,68,105,106] However, these have not assessed the impact of salt concentration[156,157] on polymer interactions, and have not managed to connect the measured interactions with important mechanical, architectural, or molecular properties. This is a significant missed opportunity, as such information could potentially build a connection between intramolecular ZW interactions and their effects on macromolecular polymer brush architectures.

This chapter reports the effect of dissolved NaCl and solution pH on the interaction potentials between surfaces with ZW polymer brushes. The impact of polymer chemistry and thickness were assessed using the ZW PMPC and poly(3-(N-2-methacryloyloxyethyl-N,N-dimethyl) ammonatopropanesulfonate) (PMAPS) copolymers introduced in Ch. 3.1.4 with varied molecular weights. Interaction potentials were measured between surfaces with adsorbed PMPC and PMAPS copolymer brushes using TIRM. PMAPS interaction

potentials and architectures were highly dependent on the NaCl concentration, while PMPC interaction potentials and architectures were nearly unaffected by NaCl. These results quantitatively demonstrate a balance between the attractive dipolar and repulsive molecular interactions of ZW polymers. Interactions are influenced by both the polymer's molecular properties and salt concentration, and directly influence the observed polymer brush architectures.

7.2 Theory

Video microscopy monitored diffusion of a spherical colloidal above a planar surface and in an evanescent wave. This allowed direct determination of the colloid's relative height distribution *p(h)*, and calculation of the potential energy distribution *U(h)* using the Boltzmann relation:

$$\frac{U(h)-U_{\mathrm{M}}}{kT}=\ln\left(\frac{p_i(h)}{p_{\mathrm{M}}}\right) \tag{7.1}$$

where *i* and M are indexes for any height bin and the most probable height bin respectively, *k* is Boltzmann's constant, and *T* is the absolute temperature. Colloidal potentials were modeled as a function of a colloid's height *h* above the planar surface, using a superposition of gravitational (G), Van der Waals (vdW), and polymer brush (P) potentials as:

$$U(h)=U_G(h)+U_{vdW}(h)+U_P(h) \tag{7.2}$$

Electrostatic contributions were insignificant and ignored, due to the high solution ionic strength and low colloidal surface potential (between -5 mV and 10 mV) under all conditions measured. The gravitational potential energy was modeled as:

$$U_G(h)=\frac{4}{3}\pi a^3\left(\rho_p-\rho_f\right)gh \tag{7.3}$$

in which a is the particle radius, ρ_p-ρ_f is the difference in particle and fluid densities, and g is the gravitational constant.

Van der Waals interactions between silica and polystyrene were modeled using the Derjaguin approximation to the Van der Waals attraction between parallel plates:

$$U_{VdW}(h) = \frac{a}{6}\int_h^\infty -\frac{A_{132}(l)}{l^2}dl \approx A_{eff}h^{-2} \tag{7.4}$$

Here $A_{132}(l)$ is the Hamaker function for silica-water-polystyrene interactions estimated using Lifshitz theory by Bitter et al., [75] and A_{eff} is a power-law approximation.

The free energy of a compressed polymer brush on a planar surface has been analytically described by Milner et al. [3,222] Milner's theory assumes well-solvated, flexible chains, and predicts a parabolic mean-field monomer concentration profile. It estimates the free energy/area f the compressed the brush at a thickness L as a function of the uncompressed brush's free energy/area f_0 and uncompressed thickness L_0 ($L_0 \geq L$) as:

$$f(L) = \frac{5}{9}f_0\left[\frac{L_0}{L} + \left(\frac{L}{L_0}\right)^2 - \frac{1}{5}\left(\frac{L}{L_0}\right)^5\right] \tag{7.5}$$

For symmetric interacting brushes with minimal inter-chain penetration, f can be converted into the steric colloidal potential U_p of two surfaces at separation $h<2L_0$ using the Derjaguin approximation in a half-space for sphere-planar geometry:

$$\begin{aligned} U_p &= 2\pi a\int_h^{2L_0} 2\left[f(l/2) - f_0\right]dl \\ &= \frac{40}{9}\pi a f_0 L_0\left[\ln\left(\frac{2L_0}{h}\right) + \frac{9}{5}\left(\frac{h}{2L_0}\right) - \frac{1}{3}\left(\frac{h}{2L_0}\right)^3 + \frac{1}{30}\left(\frac{h}{2L_0}\right)^6 - \frac{47}{30}\right] \end{aligned} \tag{7.6}$$

In which, L_0 and f_0 are the uncompressed thickness and free energy per area of the polymer brush.

Individual point measurements of a measured diffusion profile each have an error in determining the colloid's position. This error biases the measured potential (U) by distorting the measured height distribution. The contribution of point measurement error on measured distributions was modeled using convolution of a Gaussian probability *g(l)* with standard deviation ξ into the theoretical height probability distribution:

$$p_c = \int p_T(h-l)\, g(l,\zeta)\, dl \qquad (7.7)$$

ζ is used within a narrow range of 8-11nm as estimated by independent experiments. The theoretical potential with measurement noise is then calculated from the convoluted probability distribution (p_c) using Eq. (7.1)

7.3 Experimental

This section briefly summarizes the experimental methods used in this chapter. Additional details on methods, experiments, and materials can be found in Ch.7.6 (supplemental).

7.3.1 Polymer-coated colloids and slides

PMPC-b-PPO-b-PMPC (PMPC copolymers) and PMAPS-b-PPO-b-PMAPS (PMAPS copolymers) were synthesized by collaborators in the M. Herrera-Alonso lab as discussed in Ch. 3.1. The properties of polymers used in this chapter are summarized in **Table 7.1**.

Table 7.1 Overview of $PMPC_n$-b-PPO_{49}-b-$PMPC_n$ and $PMAPS_n$-b-PPO_{49}-b-$PMAPS_n$ copolymers used in this chapter

polymer	PDI[c]
$PMPC_{57}$-b-PPO_{49}-b-$PMPC_{57}$	1.4
$PMPC_{28}$-b-PPO_{49}-b-$PMPC_{28}$	1.1
$PMAPS_{90}$-b-PPO_{49}-b- $PMAPS_{90}$	1.4
$PMAPS_{29}$-b-PPO_{49}-b- $PMAPS_{29}$	1.3

Microscope slides (Fisher) were cleaned before use as and dried with N_2. Clean slides were rendered hydrophobic by spin-coating (3000 RPM, 1 min) with a 3% w/w solution of polystyrene. Silica colloids of nominal 2.3 µm, 3.3 µm, 4.1 µm, and 5.0 µm diameter (Bangs Laboratories) were rendered hydrophobic by reactive coating with octadecanol (Sigma-Aldrich). 120 nm nominal diameter polystyrene sulfate latex (Thermo Fisher Invitrogen) was used for DLS measurements of polymer size and stability. Polymer brushes were formed onto hydrophobic silica and polystyrene particles by dissolving PMPC and PMAPS copolymers in DI, and contacting polymer solutions with hydrophobic colloids or slides for a minimum of 4 hours. Free polymer was removed by at least 5 cycles of centrifugation and re-dispersion in the measurement solution (colloids), and 5 cycles of removing and replacing the liquid (slides).

7.3.2 Dynamic light scattering

Dynamic light scattering (DLS) was conducted using a Malvern Instruments Nano-ZS ZetaSizer. The mean (d_h) and standard deviation (σ_h) of measured hydrodynamic diameter were calculated using the method of cumulants. The hydrodynamic thickness (L_h) of adsorbed polymer brushes on colloids was estimated from measurements of bare and

coated polystyrene particles ($L_h = d_{h,brush} - d_{h,bare}$)/2. Hydrodynamic brush thickness was only reported for monodisperse colloidal dispersions with polydispersity index (PDI = σ_h^2/d_h^2) less than 0.08. Increases in PDI and d_h were used to infer aggregation of colloids.

7.3.3 Total internal reflection microscopy

Total internal reflection microscopy (TIRM) was used to measure interaction potentials between colloids and planar substrates with kT and nm resolution.[35,80] Briefly, an evanescent wave was excited along a SiO_2-DI interface using a 633 nm HeNe laser (Melles Griot). Images were captured using a 40× objective (LD Plan-NEOFLUAR), using a 12-bit CCD Camera (Hamamatsu Orca-ER) at 4 binning, 4 ms exposure, and a frame rate of 30 ms/frame. Custom software analyzed each image to estimate colloid scattering intensity. Relative height was calculated from

$$\frac{h}{h_m} = \beta^{-1} \ln\left(\frac{I}{I_m}\right)$$

in which I and h are the scattering intensity and colloid height, respectively, and the subscript M is the most probable observation bin. The decay length of the evanescent wave, β, was 113.2 nm, 113.67 nm, 125.99 nm, and 126.19 nm for 0.01M, 0.15M, 1M, and 3M NaCl solutions respectively.

7.4 Results & Discussion

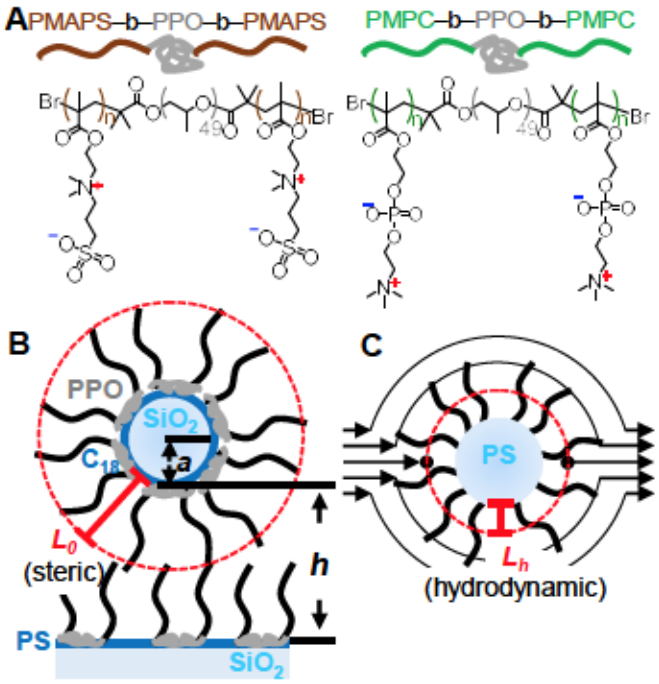

Fig. 7.1 Zwitterionic PMPC and PMAPS polymer brushes were formed from adsorption of amphiphilic triblock copolymers onto hydrophobic colloids. (**A**) $PMAPS_n$-b-PPO_{49}-b-$PMAPS_n$ and $PMPC_n$-b-PPO_{49}-b-$PMPC_n$ triblock copolymers used in this study. (**B**) Adsorbed ZW brushes formed from adsorption of polymers onto hydrophobic colloids and hydrophobic glass slides. This sphere-planar geometry is used in all measurements of colloidal interaction potentials using TIRM. The illustrated steric thickness (L_0) represents the onset of polymer interactions from overlapping polymer brushes. (**C**) Illustration of the hydrodynamic brush thickness (L_h) as the equivalent hard-sphere limit of penetration of flow into the polymer brush. L_h is obtained from DLS measurements of bare and polymer-coated colloids.

7.4.1 Brush formation and steric stabilization of colloids

Polymer brushes were formed through adsorption of PMAPS-b-PPO-b-PMAPS and PMPC-b-PPO-b-PMPC block copolymers onto hydrophobic surfaces, as shown in Fig. 7.1. Copolymers were synthesized by ARGET polymerization of MPC (phosphorylcholine-type) and MAPS (sulfobetaine-type) monomers onto a Br-PPO_{49}-Br macroinitiator, as discussed in Ch 3.1.4. Copolymers studied are summarized in **Table 7.1**,

with mean repeat of n=28, 57 for PMPC copolymers and n=29 and 90 for PMAPS copolymers.

The adsorbed PMPC and PMAPS polymer brushes effectively stabilized colloids against both deposition (>80% micron colloids stable against planar substrates) and aggregation (no observed size increases of 100nm colloids in solution) under all conditions tested. However temporary instability was noted for polymer-coated colloids after rapid addition to 1-3 M NaCl. Such instability was observed using dynamic light scattering, with abrupt but slight increases in polydispersity (**Fig. 7.6**) of $PMPC_{28}$ and $PMAPS_{29}$ coated 100nm colloids. Instability upon 1-3 M NaCl addition was also observed in TIRM experiments, with rapid deposition of 2-5 μm colloids with all polymer coatings.

The aggregation and deposition of polymer-coated colloids upon addition of 1-3M NaCl was halted by further addition of 30ppm polymer, with stability maintained over 24 hours of monitoring. Instability is thus most likely a result of lateral heterogeneities caused by polymer desorption upon NaCl addition. Sufficient lateral homogeneity of the adsorbed polymer brush is reestablished by addition of additional polymer, stabilizing the coated surfaces. This polymer addition increased the fraction of stable (not deposited or aggregated) colloids from ~15% to >80% for all TIRM experiments. Notably, the polymer addition was not found to affect the measured potentials of the stable colloids, with similar potentials of the stable particles with and without polymer addition.

7.4.2 NaCl-dependent interaction potentials

Colloidal interaction potentials U of brush-modified surfaces were measured using TIRM as a function of colloid-surface separation h. Interaction measurements were between hydrophobically-modified SiO_2 colloids of 2-5 μm diameter and polystyrene-

coated glass slides, as indicated in **Fig. 7.1B**. In both systems, single particles (black circles) show relative agreement, indicating brush homogeneity across both particles and batches (**Fig 7.9**). The ensemble average interaction potentials (red circles) of the single particles are well-described by theoretical fits of colloidal interactions (red lines) separated into van der Waals ($_{vdW}$)[44,75] and polymer ($_{P}$)[22,76,80] interactions:

$$U(h) = U_{vdW}(h) + U_{P}(h) \tag{7.8}$$

with details given in section 7.2.

7.4.3 Effect of NaCl on colloidal interaction potentials

The impact of dissolved NaCl on polymer-mediated colloidal interaction potentials was studied using TIRM, and shown in **Fig. 7.2**. Interactions were measured for PMAPS (n = 29, 90) PMPC (n = 28, 57) brushes, at pH 7, and at 0.01-3M NaCl as indicated. In all conditions, the ensemble average (circles) are well described by fits of colloidal theory (lines). The results shown for 3 μm colloids are consistent with those of 2 μm, 4 μm, and 5 μm colloids.

[NaCl] has a strong impact on the PMAPS-modified colloids interactions (**Fig. 7.2A-B**). Increasing [NaCl] causes (i) an increase in the most-probable separation, (ii) a decrease in the depth of the attractive interaction well, and (iii) a shift of the repulsive interactions and potential well minimum (most probable separation) towards larger separations. The $PMAPS_{90}$-mediated interactions also occur at larger separations and with smaller interaction wells than the $PMAPS_{29}$-mediated interactions, as expected for the formation of a thicker polymer brush with increased polymer repeat units.[22,23]

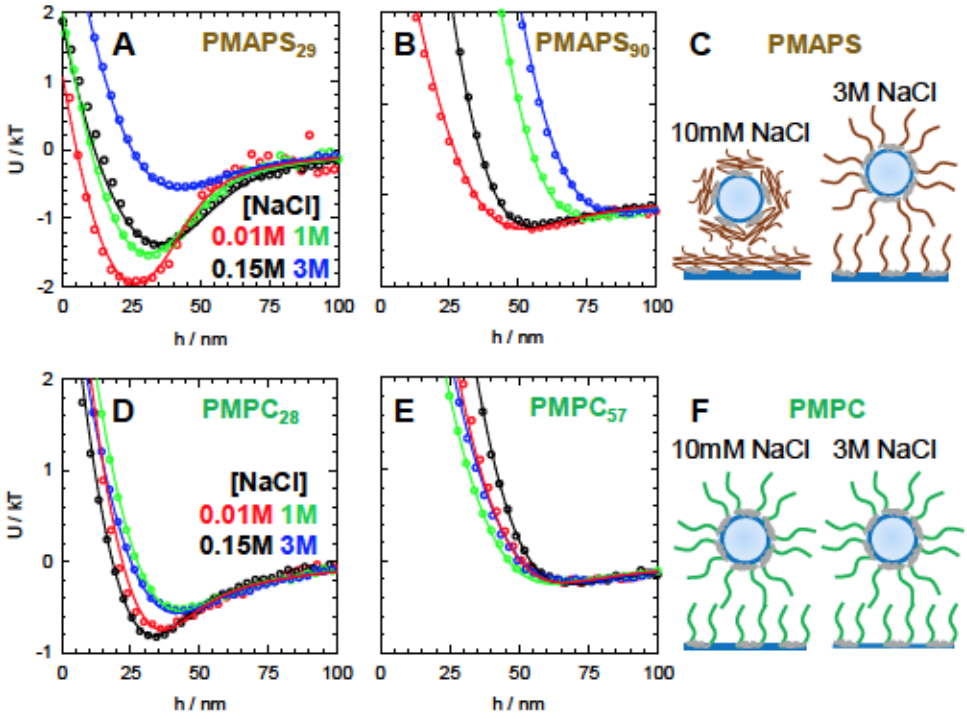

Fig. 7.2 NaCl-dependent ensemble-average interaction potentials between polymer-coated 3μm colloids and planar surfaces as measured by TIRM. (**A, B**) PMAPS-mediated colloidal potentials. Measured (points) and fit to Eqn. 1-3 (lines). (**C**) Interaction schematics indicating the sensitivity of PMAPS polymer brushes to [NaCl] indicated by the measured potentials. (**D, E**) PMPC-mediated colloidal potentials. Measured (points) and fit to Eqn. 1-3 (lines). (**F**) Interaction schematics indicating the insensitivity of PMPC brush to 0.01-3M NaCl.

In stark contrast to the PMAPS-mediated interactions, the interactions of PMPC-modified colloidal (**Fig. 7.2D-E**) display a very weak dependence on [NaCl]. $PMPC_{57}$-mediated potentials display a nearly identical across 0.01-3M NaCl, with nearly identical brush repulsions, attractive well depths, and location of the potential minimum. The $PMPC_{28}$-mediated potentials are also similar across 0.01-3M NaCl, although with additional variation in well location and size reasonable for measurement error across multiple conditions. This variation is only loosely correlated with NaCl concentration, with the measured most-probable separation following the order of 0.015M<0.01M<3M<1M.

$PMPC_{57}$-mediated interactions also occur at larger surface separations than the $PMPC_{28}$-mediated interactions, again expected for the increased repeat units.

The effects of [NaCl] on measured interactions are not a result of colloidal surface properties. Electrostatic interactions are negligible at all conditions due to both the low surface charge (1±4 mV zeta potential) and short debye length ($\kappa^{-1} < 3$ nm) for all conditions. Instead, [NaCl] is expected to primarily effect interaction potentials by changing the polymer architecture. As depicted in **Fig. 7.2C**, the increasing repulsion length of the PMAPS brush with [NaCl] reflects a transition from relatively compressed to swollen polymer architectures. In contrast, the NaCl-invariant potentials and architectures of PMPC brushes reflect swollen architectures across all [NaCl]. The changing polymer architectures is a result of NaCl addition weakening attractive dipole-dipole molecular interactions, which is reportedly important in influencing PMAPS but not PMPC interactions, brush architectures, and solubility.[58,72,141,149,154]

The effect of pH on interaction potentials was also investigated as an additional means of disrupting the ZW dipole-dipole interactions, shown in **Fig. 7.3** for $PMPC_{28}$ and $PMPC_{57}$ at 0.150M NaCl. PMPC is at a net neutral charge at pH 7.2 (black), with a zeta potential of 1±4mV for PMPC coated colloids. PMPC-coated colloids were partially charged at pH 2.5 with a moderately positive zeta potential of 12±5mV. This is expected as PMPC should be only slightly positive at pH 2.5 due to protonation of the phosphate group, as the monomer pK_a of 2.5-3 in solution is reduced to about 1.5 in polymer and micellar states.[46,158] The effect of pH on PMAPS was not investigated, as the MAPS monomer ($pK_a<1$)[150,151] requires very acidic conditions to obtain a net positive polymer charge that are not compatible with our setup.

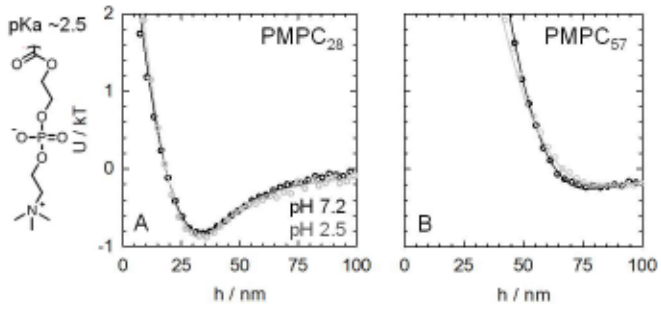

Fig. 7.3 pH-dependent interaction potentials *U*(h) of PMPC-coated 3μm colloids and surface. In both panels, the ensemble-average interaction potentials between 3μm colloids and surfaces with adsorbed polymer brushes. pH 7.2, 150mM NaCl (black). pH 2.5, 150mM NaCl (gray). (**A**) surfaces with adsorbed $PMPC_{28}$ brush. (**B**) surfaces with adsorbed $PMPC_{57}$ brush.

As shown in **Fig. 7.3**, both $PMPC_{28}$ and $PMPC_{57}$ interactions display very little effect upon changing pH. Both polymers show a near overlap of potentials at pH 2.5 and 7.2, with nearly identical potential well depths and similar locations of the most probable height. Together, these effects further suggest that disruption of the dipolar interactions has very little effect on the PMPC molecular interactions and polymer architectures.

7.4.4 Characterization of brush thickness

The impact of the PMAPS and PMPC brush architectures on the measured colloidal potentials was explored with studies of brush thickness (L). Here, we focused on two different aspects of brush thickness. The steric thickness L_0 (indicated in **Fig. 7.1B**, Eq. (7.6)) represents the effective length of onset for brush interactions between two overlapping polymer brushes. L_0 was obtained by fitting Eq. (7.8) to the measured colloidal interactions potentials. The hydrodynamic thickness L_h (**Fig. 7.1C**) represents the excess drag imposed on a colloid by the polymer brush.[159] L_h was obtained from measurements of the hydrodynamic radius of bare and polymer-coated 100 nm colloids using dynamic light scattering (DLS).

Polymer brushes exhibit a decaying monomer concentration profile away from the colloid surface. Steric interactions are sensitive to initial brush overlap at the low-concentration brush periphery, whereas hydrodynamic flow is able to penetrate to a moderate distance within the low-concentration polymer brush periphery.[22,23] While L_0 is thus typically expected to be somewhat larger than L_h, the quantitative details depend on the exact details of the polymer architectures and density profile.

Effect of [NaCl] on PMAPS brush thickness

The thickness of PMAPS brushes are highly dependent on [NaCl]. As shown in **Fig. 7.4A** for L_0 (circles, solid line) and L_h (triangles, dotted line), $PMAPS_{29}$ and $PMAPS_{90}$ brushes demonstrate a nearly 50% increase in thickness between 0.01-3M NaCl. $PMAPS_{90}$ is also significantly thicker than $PMAPS_{29}$. Scaling the $PMAPS_{29}$ and $PMAPS_{90}$ thicknesses by the weight-averaged contour length (Lc_w) of the PMAPS blocks collapses them onto similar curves (**Fig. 7.4B**). L_0 of both PMAPS brushes extend from 50-95% Lc_w between 0.01-3M NaCl. $L_0 > L_h$ across measurements, consistent with expectations for the increased sensitivity of steric interactions to the brush periphery.[22,23] The reduction of L_h relative to L_0 is especially pronounced at low 0.01-0.15M NaCl, and may indicate a highly compressed polymer region with an extended low-concentration tail in the brush periphery. Such an architecture is somewhat speculative, but consistent with the previously reported monomer density profiles for a moderately polydisperse PMAPS brush.[64]

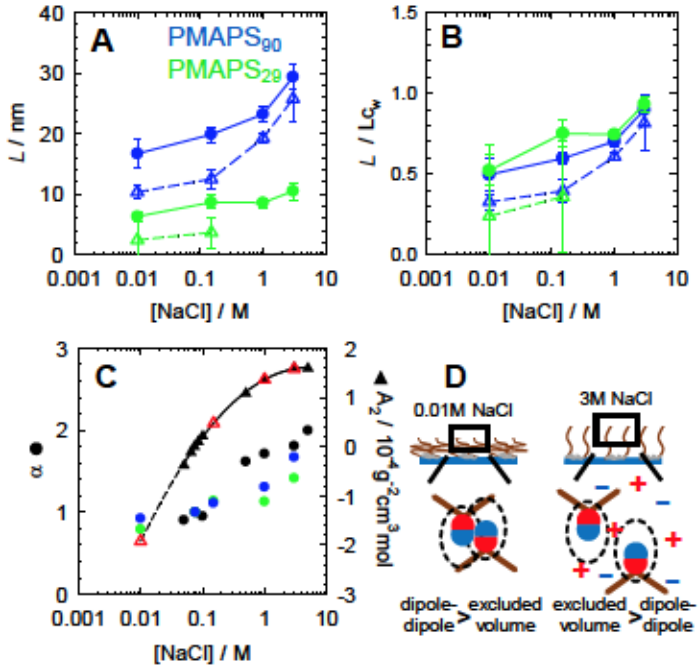

Fig. 7.4 PMAPS brush architectures are highly compressed and fully extended at low and high [NaCl], respectively. (**A**) NaCl-dependent brush thickness (L) of adsorbed $PMAPS_{29}$ and $PMAPS_{90}$ triblock copolymers. Steric thickness (L_0) (circles, solid lines) from fits of potentials to Eq. (7.8), and hydrodynamic thickness L_h (triangles, dashed lines) from DLS measurements of bare and coated colloids. Lines are included to guide the eye. (**B**) Brush thicknesses from panel A scaled by the weight-averaged contour length (Lc_w) of the PMAPS blocks. (**C**) Dependence of the expansion coefficient (α, circles) and second virial coefficient (A_2, triangles) on [NaCl]. α from steric L_0 of $PMAPS_{29}$ (green) and $PMAPS_{90}$ (blue) adsorbed brushes in this study, and the radius of gyration of $PMAPS_{884}$ grafted brushes (black) from Kikuchi et al[63] normalized to interpolated values at 0.076M NaCl (theta condition). A_2 of PMAPS homopolymer as measured by Kikuchi et al (measurement, circles; fit, line; extrapolated, dotted line).[63] (**D**) Representation of the brush architectures and molecular interactions to explain the measurements in panels A-C. Compressed brush architectures at low [NaCl] are caused by the dominance of attractive monomer-monomer dipolar interactions at low [NaCl]. Dipolar interactions are attenuated by addition of NaCl, causing highly extended brushes architectures with the dominance of repulsive excluded volume and solvation interactions.

The brush thickness measurements reflect relative brush compression and extension of the PMAPS brushes in low and high [NaCl], respectively. This compression and extension is quantified for L_0, using the chain expansion coefficient α in **Fig. 7.4C**:

$$\alpha = \sqrt{L_0(C_{NaCl}) / L_{0,\theta}} \qquad (7.9)$$

where each salt-dependent $L_0(C_{NaCl})$ is normalized by an interpolated $L_{0,\theta}$ at 0.076M NaCl, the PMAPS theta condition at 25°C. α is between 0.5-0.7 for all PMAPS polymers at 0.01M NaCl (relative compression) and increases to 1.5-2 at the very concentrated 3M NaCl (relative extension). The PMAPS brush extension agrees closely with second virial coefficient (A_2) measurements from Kikuchi et al[63] (black circles, **Fig. 7.4C**). PMAPS A_2 are slightly negative at 0.01M NaCl ($-1.9 \times 10^{-4} g^{-2} cm^3 mol$) indicating slightly attractive polymer-polymer interactions. A_2 becomes positive (net repulsive) with increasing NaCl, reaching $1.6 \times 10^{-4} g^{-2} cm^3 mol$ at 3M NaCl. This transition closely follows the transition of PMAPS brush architectures, suggesting that the molecular polymer interactions are the cause of the PMAPS swelling behavior.

The NaCl-dependence of PMAPS reflects classic 'anti-polyelectrolyte' behavior, with increasing NaCl attenuating the attractive dipole-dipole interactions between monomer units. As is illustrated in **Fig. 7.4D**, the attractive dipolar interactions dominate at low [NaCl] with net attractive monomer-monomer interaction. Attenuation of the dipolar interactions with addition of salt causes a domination of repulsive solvation and excluded volume effects. The high 3M NaCl required for full extension, and thus full attenuation of dipolar attractions, is reasonable as 1M NaCl generates a spacing between ions equivalent to the intramolecular spacing amongst repeat units in the polymer chain.[109] The nearly fully extended brushes at high [NaCl] likely indicates a large repulsive intermolecular interactions, although additional parameters such as polymer surface density and chain stiffness likely also contribute.[59,60]

It is somewhat surprising that the PMAPS brushes stabilized colloids at the 0.01M NaCl condition. Attractive polymer-polymer interactions between overlapping polymer

brushes may result in deposited or aggregated colloids, and the negative A_2 for PMAPS at 0.01M NaCl of -1.8×10^{-4} $g^{-2}cm^3mol$ approaches the phase separation regime.[160,161] However previous measurements reporting insolubility of PMAPS homopolymers at 10mM NaCl were for much larger polymers than this study.[150] The polymers in this study would thus likely possess increased solubility in the poor solvent condition. The A_2 value at 0.01M NaCl may also be somewhat inaccurate, as it was produced from extrapolation of Kikuchi's measurements spanning 0.5-5 M NaCl.

Notably, while PMAPS colloids in 10mM NaCl were stable against deposition during the 2 hours of our TIRM measurements, aggregated clusters of colloids were observed after 24 hours (**Fig. 7.8**). This suggests a weak attraction of overlapping PMAPS brushes, with reversible pairwise colloid-colloid interactions on the order of thermal energy, but stronger and irreversible multi-body attractions. Micron colloids displayed the same slow aggregation and deposition behavior for both the $PMAPS_{29}$ and $PMAPS_{90}$ polymer coatings despite the drastically increased $PMAPS_{90}$ brush length (7 nm vs. 17 nm). The colloidal deposition at 0.01M NaCl is thus attributable to the polymer-polymer interactions, and not colloidal Van der Waals interactions of the adsorb surfaces. Notably, 100 nm and 400 nm colloids did not noticeably aggregate in 0-10mM NaCl over 24 hours as monitored by DLS. This improved stability of smaller colloids further suggests that the PMAPS-PMAPS attraction of overlapping brushes is mild, as smaller colloids with a reduced area of polymer overlap possess reduced net polymer-polymer attraction.

7.4.5 Effect of NaCl on PMPC brush thickness

In stark contrast to the strong NaCl-dependence of PMAPS architectures, the thickness of PMPC brushes (**Fig. 7.5A**) are mostly unaffected from 0.01-3M NaCl. For

$PMPC_{28}$, L_0 and L_h are within 12-14 nm and 10-11 nm, respectively. For both PMPC brushes this variation is not correlated to increasing NaCl, all variation within the standard experimental error. Scaling the brush thickness by the Lc_w (**Fig. 7.4B**) also collapses $PMPC_{28}$ and $PMPC_{57}$ onto similar curves, with L_0 and L_h are within 90-110% Lc_w and 80-100% Lc_w respectively. This indicates that the PMPC brushes are highly extended with a large contribution from the higher molecular weight polymer variants. Notably, as the steric interactions between brushes begin with the onset of polymer overlap, only some of the higher molecular-weight polymers need to be at full extension for a brush's L_0 to follow its Lc_w. The full brush extension reported here thus does not preclude the decaying monomer concentration profiles away from the surface reported in previous studies of PMPC brushes.[66]

The NaCl-independence of the PMPC brush length is consistent with our PMPC-modified colloidal interactions and previous studies of PMPC brush architectures.[64,72,115] Increased L_0 of $PMPC_{57}$ relative to $PMPC_{28}$ is expected with the larger colloidal separation and stronger brush repulsion for the $PMPC_{57}$ brushes. The independence of measured PMPC brush lengths on [NaCl] also consistent with previous measurements of PMPC solution properties. This is shown in **Fig. 7.4C**, which reports the second virial coefficient A_2 measured by Kikuchi et al (triangles)[63] along with the brush expansion factor α (circles) normalized to an extrapolated L_0 at 0M NaCl. As seen in **Fig. 7.4**, the PMPC A_2 is positive and nearly constant at 0.2×10^{-4} $g^{-2}cm^3mol$ across 0-5M NaCl. The chain expansion coefficients are also very uniform, with random variation between α=0.95-1.05.

PMPC thus exhibits nearly constant intermolecular interactions and polymer architectures across the measured solution conditions. As illustrated in **Fig. 7.4D**, this

suggests that PMPC's attractive dipolar interactions are insignificant relative to the excluded volume and solvation contributions at all [NaCl]. As for PMAPS at 3M NaCl, the high PMPC brush extension suggests that these repulsive polymer-polymer molecular interactions are very large, although again additional parameters such as grafting density and chain stiffness likely also influence brush extension.[59,60]

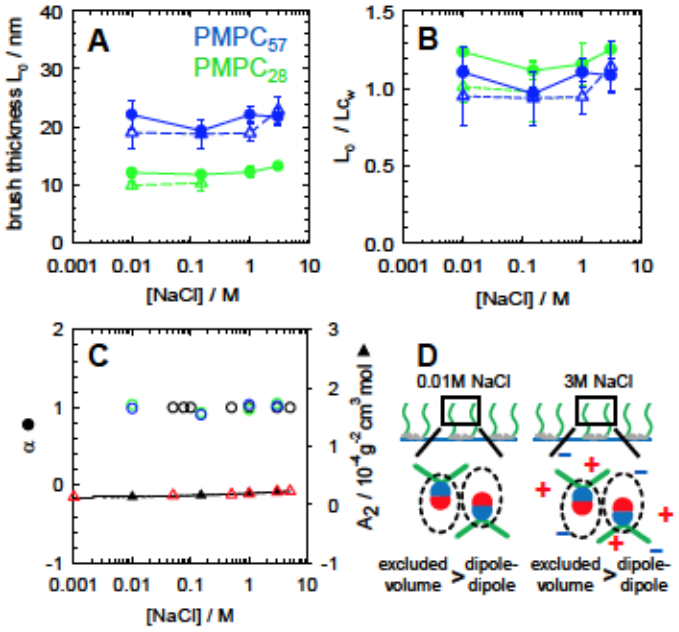

Fig. 7.5 PMPC brush architectures are highly extended across both low and high [NaCl]. (**A**) NaCl-dependent brush thickness (L) of adsorbed $PMPC_{28}$ and $PMPC_{57}$ triblock copolymers. Steric thickness (L_0) (circles, solid lines) from fits of potentials to Eqn. 1-3, and hydrodynamic thickness (L_h) (triangles, dashed lines) from DLS measurements of bare and coated colloids. Lines are included to guide the eye. (**B**) Brush thickness from panel A scaled by the weight-averaged contour length (Lc_w) of the PMAPS blocks. (**C**) Dependence of the expansion coefficient (α, circles) and second virial coefficient (A_2, triangles) on [NaCl]. α from steric L_0 of $PMPC_{28}$ (green) and $PMPC_{57}$ (blue) adsorbed brushes in this study, and the radius of gyration of $PMPC_{790}$ grafted brushes (black) from Kikuchi et al.[63] α are normalized to interpolated values at 0.076M NaCl (theta condition). A_2 of PMAPS homopolymer as measured by Kikuchi et al (measurement, circles; fit, line; extrapolated, dotted line).[63] (**D**) Representation of the brush architectures and molecular interactions to explain the measurements in panels A-C. Brushes are highly extended at all [NaCl], indicating the dominance of a repulsive monomer-monomer interaction term at all conditions.

7.4.6 PMPC and PMAPS molecular interaction mechanisms

The strong and weak NaCl dependence of PMAPS and PMPC architectures, respectively, are consistent with literature reports. This difference in behaviors is difficult to explain mechanistically using molecular interactions, however. We are not currently aware of work that mechanistically connects the molecular-scale monomer-monomer and monomer-solvent interactions to the macromolecular-scale brush architectures for these or similar polymers.

One possible explanation is that the dipolar interactions are significant for the PMAPS but insignificant for the PMPC polymers. Previous computational studies report dipole moments of 21 and 26 Debye for the MPC[162] and MAPS[163] side chains, respectively. Specific hydration or orientation effects may potentially further reduce the PMPC dipole moment. However, while reductions in the PMPC dipole moment would lead to reduced dipole-dipole interaction strengths, they most likely would not negate the PMPC dipole-dipole interactions.

Another possibility is that, for PMPC, a repulsive component of the molecular interactions is much stronger than that of PMAPS. That repulsive component would then dominate the PMPC dipolar interactions at all salt strengths. Strong solvation interactions are indicated by molecular simulation[164] and spectroscopic[58] studies of PMPC in solution. These studies include persistent water structure around the PMPC quaternary amine, which may give rise to highly persistent and extended polymer structures. Specific solvation effects seem to be a result of the specific monomer chemical structure, as a recent study by Morozova et al recovered NaCl sensitivity for a PMPC analog with swapped amine and phosphate positions.[155] Together, this suggests that the molecular interactions and architectures of a given ZW polymer is likely a result of both dipolar interactions (dipole moment, salt strength) and specific chemical affects.

7.5 Conclusion

In summary, this chapter investigated the NaCl-dependent, k*T*-scale interaction potentials and architectures of colloids with adsorbed ZW polymer brushes. ZW block copolymers PMPC-b-PPO-PMPC and PMAPS-b-PPO-PMPC adsorbed onto hydrophobic surfaces to form high-density polymer brush coatings. These coatings stabilized μm and

nm sized colloids against deposition and aggregation, respectively. Robust stability was observed across a wide range 0.01-3M NaCl, with the sole exception of initially stable but slowly depositing micron colloids under conditions of attractive polymer-polymer interactions (PMAPS polymer brushes at 0.01M NaCl).

Dissolved NaCl had a small role in influencing the interaction potentials of PMPC-coated colloidal surfaces. This was evident from PMPC brush thicknesses that were highly extended to between 90-110% Lc_w across all measured 0.01-3M NaCl. In contrast, dissolved NaCl had a strong influence on PMAPS-mediated colloidal interaction potentials, extending from 50-90% Lc_w from 0.01M to 3M NaCl respectively. The NaCl-dependence of the PMPC and PMAPS brush extension agrees closely with literature measurements of their second osmotic virial coefficients and solution behavior.

Together, this offers further evidence towards attractive dipolar and repulsive solvation and/or excluded volume interactions between ZW monomers that affect polymer brush properties. The balance between the attractive and repulsive contributions is highly affected by both solvent quality (dissolved salt) and specific monomer chemistry (specific solvation effects). High extension of the ZW polymer brushes during attenuation of dipolar attractions also offers a macromolecular-scale explanation for their reportedly enhanced antifouling and stabilization properties. These solvent quality effects are also an exploitable mechanism to achieve solution-insensitive brush performance (PMPC brushes) and solution-dependent brush performance (PMAPS brushes).

7.6 Supplemental Information

7.6.1 Determination of colloidal stability in NaCl solutions

Stability of 100nm PS with different polymer coatings and in 0.15M NaCl are shown in **Fig. 7.6**. For colloid size (**Fig. 7.6A**), error bars indicate the standard deviation of the size distribution. For polydispersity (**Fig. 7.6B**), error bars indicate the standard deviation of triplicate measurements. All colloids were monodisperse after polymer addition, with hydrodynamic diameter between 130-170nm depending on the hydrodynamic thickness of the polymer coating. Uncoated colloids exhibited rapid aggregation in 0.15M NaCl solution, with a substantial increase in the size (d_h>1μm) and polydispersity (σ_h^2/d_h^2>0.6) over 24 hours. Colloids with all polymer coatings were effectively stabilized, with statistically similar size and polydispersity after 24 hours of monitoring.

The stability of polymer-coated colloids was also monitored after addition of NaCl from 0.15M to 1M. This is reported in **Fig. 7.7**, for colloids after 24 hours in pbs solution, 4 hours after adjustment from 0.15M to 1M NaCl, and 4 hours after adjustment from 0.15M NaCl to 1M NaCl + 30ppm of the polymer. Error bars report the standard deviations of at least triplicate measurements for both size (**Fig. 7.7A**) and polydispersity (**Fig. 7.7B**).

Colloids with all polymer coatings displayed a small amount of aggregation after addition of NaCl from 0.15M to 1M. Aggregation was observed from polydispersity and size increases, with greater increases for the $PMAPS_{29}$ and $PMPC_{28}$ coated colloids (40-50nm Δd_h; 0.14-0.15 $\Delta(\sigma_h^2/d_h^2)$) than the $PMAPS_{90}$ and $PMPC_{57}$ coated colloids (Δ14-20nm d_h; 0.08-0.1 $\Delta(\sigma_h^2/d_h^2)$). Addition of 30ppm of polymer during the NaCl addition reduced the aggregation of $PMAPS_{29}$ and $PMPC_{28}$ coated colloids, and completely

eliminated aggregation of $PMAPS_{90}$ and $PMPC_{57}$ coated colloids. This suggests that the aggregation of colloids with addition of NaCl is caused by desorption of the polymers, creating a patchy or inhomogeneous polymer surface. Colloids would be expected to aggregate or deposit when separate oriented with overlapping bare or low-density polymer patches.

Colloids with longer polymer coatings would likely be less vulnerable to heterogeneity-induced destabilization. Longer brushes would be less vulnerable to forming bare patches, with more ability to smooth out local variations in brush thickness. Longer chains would also produce thicker brushes, requiring a larger local reduction in the brush thickness to get to a minimum brush thickness for colloidal stabilization. Together, these expectations for heterogeneity-induced destabilization are supported by the data in **Fig. 7.64**-**Fig. 7.7**.

TIRM experiments also noted deposition of polymer-coated 2-5μm colloids to polymer-coated planar substrates after addition of 1-3M NaCl. As a single-particle measurement technique, TIRM experiments measured bimodal stability behavior with some particles exhibiting very stable diffusion, and some irreversibly depositing against the surface. The fraction of stable (diffusing) colloids was significantly increased by including 30ppm polymer during salt addition, from about 10% for NaCl only to about 80% for NaCl plus polymer.

Both the deposition rate and extent of deposited of colloids were greater for the micron colloids with TIRM than the 100nm colloids with DLS. This is consistent with our proposed mechanism of aggregation from the alignment of low-polymer density surface patches of adjacent colloids. Specifically, larger colloids have stronger attractive Van der

Waals interactions, and require a stronger and longer-range polymer repulsion for robust stability. Larger colloids would thus tolerate smaller local fluctuations in polymer density and brush thickness, and be less stable than smaller colloids for a given polymer brush.

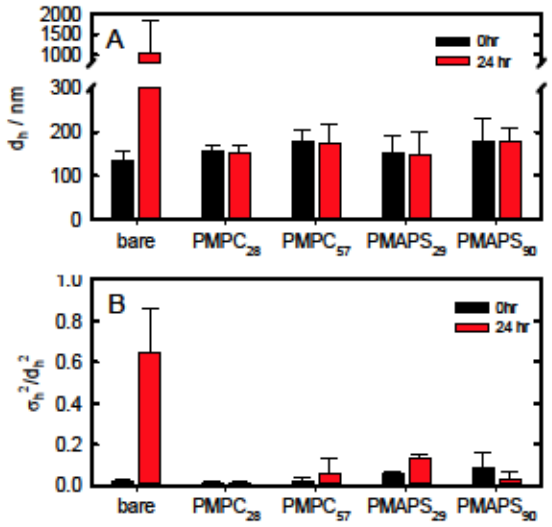

Fig. 7.6 Aggregation of polymer-coated PS colloids monitored by DLS. (A) Mean hydrodynamic diameter a_h of bare, PMPC coated, and PMAPS coated 100nm PS in 150mM NaCl. Error bars indicate the standard deviation of the measured size distribution. **(B)** Polydispersity index a_h of bare, PMPC coated, and PMAPS coated 100nm PS in solution. Error bars indicate the standard deviation of at least triplicate measurements.

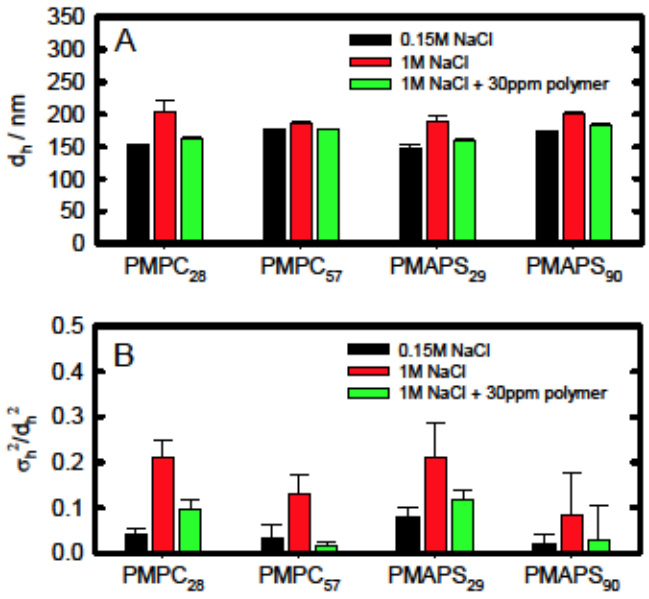

Fig. 7.7 Aggregation of polymer-coated colloids after addition of NaCl, monitored by DLS. In both panels the colloid dispersion after: 4 hours in 0.15M NaCl (black), 4 hours after addition of NaCl to 1M, 4hours after addition of NaCl to 1M plus 30ppm of polymer. In both panels, error bars indicate the standard deviation of at least triplicate measurements. (**A**) hydrodynamic radius of colloidal dispersion. (**B**) polydispersity of colloidal dispersion.

7.6.2 Stability of PMAPS-coated colloids in poor solvent

PMPC and PMAPS-coated colloids were all stable in salt solutions over the 24 hours of observation (example in **Fig. 7.8A,B**). The only exception is for PMAPS-coated colloids in 0.01M NaCl, which were stable during an initial 2 hours of observation, but both aggregated and deposited after 24 hours. The PMAPS-coated colloids in 0.01M NaCl also deposited in highly aggregated clusters (**Fig. 7.8C**). Interestingly, PMAPS-coated 100nm colloids were monodisperse in 0.01M NaCl (σ_h^2/d_h^2<0.08) over 24 hours of monitoring in DLS.

As discussed in the main text, the deposition of PMAPS-coated colloids in 0.01M NaCl is attributed to weak polymer-polymer attraction for several reasons. First, 0.01M NaCl is a poor solvent for PMAPS with net-attractive polymer-polymer interactions (**Fig.**

7.4C). Second, colloids with both $PMAPS_{29}$ and $PMAPS_{90}$ exhibited the deposition behavior discussed and showed in **Fig. 7.8B**. Finally, and most significantly, the deposited colloids were deposited as large aggregates (**Fig. 7.8C**).

The highly-aggregated state of deposited colloids is very unusual behavior for µm-colloids in sphere-planar interactions geometries. Typically, surface attractions are dominated by the colloidal surface (Van der Waals) interactions, which are twice as strong for sphere-planar interactions that sphere-sphere. In such systems, unstable particles typically deposit faster than they aggregate, and thus typically deposit as individual particles. The highly aggregated deposited states in **Fig. 7.8C** suggest a different mechanism, with stable isolated particles and unstable multi-particle clusters. Such behavior is possible for weakly attractive polymer-polymer interactions between overlapping brushes, with individual particle-particle interactions of ~kT but multi-body particle-particles interactions >kT. Together, this suggests that weak polymer-polymer attractions upon brush overlap are the likely cause of the highly aggregated and deposited colloids observed for PMAPS coatings in 0.01M NaCl

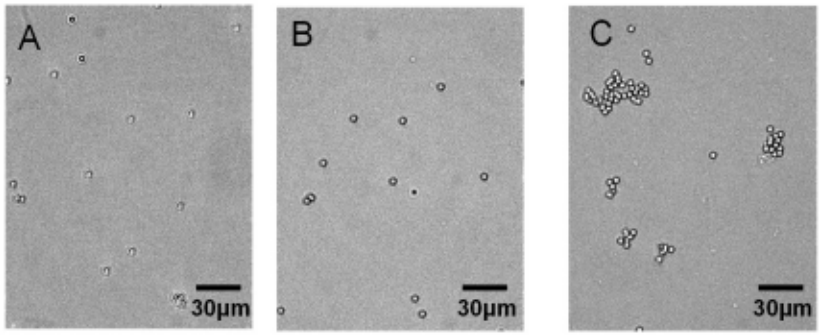

Fig. 7.8 Stability and deposition of $PMAPS_{29}$-coated 3µm SiO_2 in 0.15M NaCl and 0.01M NaCL (good and poor solvents for PMAPS, respectively). (**A**) 0.01M NaCl, 20 minutes after addition of colloids to the slide. (**B**) 0.15M NaCl, 1 day after addition of colloids. (C) 0.01M NaCl, 1 day after addition of colloids.

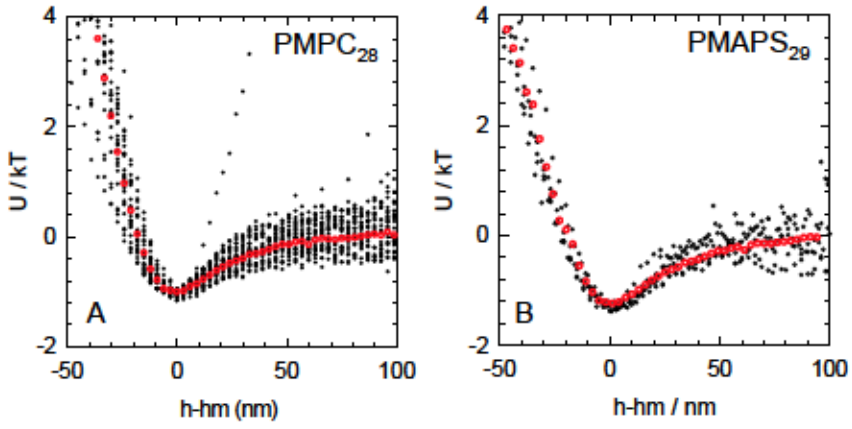

Fig. 7.9 Single-particle interaction potentials *U*(h) measured by TIRM. (**A**) $PMPC_{28}$-coated colloids and $PMPC_{28}$-coated slides. (**B**) $PMAPS_{29}$-coated colloids and $PMAPS_{29}$-coated slides. In both panels, single particle potentials (black circles) and the ensemble average potentials (red circles).

7.6.3 Colloid interaction potentials

Interaction potentials were measured at a single-particle level using TIRM. This is shown in **Fig. 7.9**, for 3μm colloids with either $PMPC_{28}$ (A) or $PMAPS_{29}$ (B) coatings in 0.15M NaCl. As seen, single particles are generally in close agree with the measured potential, and only small amount of heterogeneity in the measured potentials. Further discussion is included in Ch. 7.4.2.

8 CONCLUSIONS

Steric (polymer) stabilization of colloids is critical for materials performance in many physiological and environmental applications. Recent studies have suggested that novel zwitterionic chemistries may impart enhanced stabilization performance, but performance mechanisms are poorly understood and the development of effective polymer coatings is highly empirical.[54,90,96,128]

The general goal of this thesis was to gain a mechanistic understanding of steric stabilization of colloids, especially as pertains to zwitterionic polymer chemistries. Colloids were stabilized with novel adsorbed amphiphilic zwitterionic block copolymers, allowing facile and robust control over both the chemistry and architecture (e.g. thickness) of the polymer coatings. The important interaction mechanisms and polymer features in imparting colloidal stability were inferred from kT-scale interaction measurements of colloids with systematically varied adsorbed polymer layer properties. These systematic interaction measurements were compared to colloidal stability against deposition and aggregation in a variety of model systems of interest to various stabilization applications.

The first study compared interactions and architectures of colloids with poly(ethylene oxide) (PEO) and a common zwitterionic phosphorylcholine polymer (PMPC). PMPC coatings stabilized colloids with 2-3 fold reduced repeat units as PEO coatings. Measurements showed that this stabilization difference was due to differences in layer thickness, with the PMPC layer nearly fully extended to its molecular-weight averaged contour length. PEO and PMPC layers of equivalent thickness generated equivalent colloidal interactions and stability. Together, these results indicate that the layer thickness is the most important property in influencing colloidal stability. For the well-solvated polymers used in this study and most appropriate in stabilization applications,

molecular chemistry is thus only indirectly important as it influences layer thickness and extension.

Work then applied this understanding of the importance of polymer layer thickness to studies of PEO and PMPC stabilization and interactions against model protein, extracellular matrix, and mucus biomaterial surfaces. Here, increasing both the polymer and biomaterial thickness improved colloidal stability, again indicating the importance of non-specific colloidal and polymer interactions at determining stability.

Colloids also exhibited polydisperse stability behavior against each biomaterial, with populations of stable, intermittently deposited, and permanently deposited colloids in most combinations of biomaterial, polymer chemistry, and polymer layer thickness. Such polydisperse behavior was also observed at the single-particle level of colloidal interactions, with the population of robustly stable colloids demonstrating the non-specific interactions expected from independent characterization of polymer-polymer and biomaterial-biomaterial interactions. Together, this demonstrates that, while non-specific colloidal and polymer interactions determine the stability of colloids in material systems, effective polymer coatings must overcome heterogeneities in the target materials. Effective materials design thus requires studies at the single-particle level to determine the distribution of materials properties. Such studies should focus on both a systems-level of polydispersity in the target materials (e.g. various material substrates in a given system) as well as a local-level of material heterogeneity (e.g. lateral heterogeneities within a given layer).

While polymer layer thickness may be expected to be a key parameter in the steric stabilization of colloids, it was surprising that the PMPC layers were at full extension. This

thesis then concluded by examining the molecular properties causing the highly extended zwitterionic architectures. NaCl-dependent interactions and architectures of two common zwitterionic polymers (PMPC, phosphorylcholine type; PMAPS, sulfobetaine type) were studied to investigate the importance of dipole interactions on zwitterionic polymer properties. The polymers showed highly contrasting behaviors, with PMAPS layers ranging from compressed to fully extended from 0.01-3M NaCl but PMPC mostly unaffected. The PMAPS and PMPC layer thicknesses were highly correlated with literature measurements of polymer solvation. Using a literature survey of key molecular parameters, the difference in PMAPS and PMPC behaviors were shown to be a result of competition between attractive monomer-monomer dipole interactions and repulsive solvation and/or polymer stiffness effects. The balance of these interactions is highly dependent on both dipole moment, solvent ion composition, and specific solvation or structural effects. Practically, these properties allow for the creation of materials with responsive (solution-dependent) or unresponsive (solution-independent) properties, as desired for various applications.

In conclusion, this thesis studied the role of polymer chemistry and architecture in stabilizing colloids in a variety of settings. The solvated polymer layer thickness was the most important parameter in stabilizing a colloid. Zwitterionic polymers of interest as 'high performing materials' in drug delivery and anti-fouling materials were equivalent to conventional PEO coatings when compared across coating thicknesses. However, in applications layer thickness must be controlled beyond a minimum length to overcome not just non-specific colloidal interactions (e.g. van der Waals attractions from the underlying surfaces), but also to compensate for local heterogeneities in material grafting densities and

thicknesses. The polydispersity of colloidal behaviors in biomaterials systems suggests that single-particle level analyses are vital to the complete understanding of materials performance and properties. Together, these results provide valuable information that may prove useful in the design, performance, and characterization of drug delivery, diagnostic, and anti-fouling materials.

9 FUTURE RESEARCH

This thesis focused on understanding the stability of colloids with adsorbed polymer brushes. Measurements and modelling characterized and explained interactions at the kT scale, which determines the onset of colloidal stability in quiescent systems. Several important extensions are possible that may provide additional understanding towards materials design and behavior. This chapter attempts to provide a high-level overview of the extensions and their current state of realization.

9.1 Strong-force Measurements of Zwitterionic Polymer Layers

An important theme of this thesis was the relationship between k*T*-scale polymer interactions and their brush architectures. However, the dense polymer brushes that were studied (and that are typically desired for stabilization) only exhibit 1-5% compression at the kT scale. While the measured interactions in this thesis directly relate towards understanding colloidal stabilization, they provide a more limited understanding of polymer brush mechanics and hydrodynamic properties.

Measurement of polymer interactions using mechanical measurements techniques (such as colloidal-probe atomic force microscopy or the surface force apparatus), would be an excellent complement to our current measurement and characterization. Mechanical measurements may be less sensitive to the initial polymer overlap between two layers that our measurements are most appropriate for. However large applied forces would be able to probe a much larger range of polymer compression, more effectively probing the resistance of a polymer coating to compression. Systematic variation of architecture, chemistry, and solvent quality could effectively assess the molecular and continuum

influences of brush compression resistance (e.g. f_0 in Eq (2.13), which was only imprecisely determined by the measurements in this thesis.

Determining the dependence of f_0 on polymer chemistry, architecture, and solution quality may reveal significant insight into the roles of specific-ion effects, enthalpic polymer-polymer interactions, and chain stiffness. All of these properties likely have a more significant role in affecting brush stiffness (f_0) than brush thickness (L_0), which is largely determined by simply the net preference of monomer for solvent. While the literature includes some reports of mechanical force measurements of polymer interactions, none of these measurements include a systematic variation of polymer architectures or monomer chemistries. Such systematic variation is necessary for a fundamental understanding of the mechanisms dictating the measured polymer compression mechanics, and is accessible using the adsorbed polymer approach in our studies.

9.2 Interactions of Zwitterionic Polymers with Cells

While this thesis made progress in the understanding of polymer brush interactions, early dissertation work also explored the use of optical microscopy to measure interactions between polymer-coated colloids and cells. The general strategy was the measurement and analyses of lateral diffusion trajectories of colloids adjacent to cells, and using the statistical mechanical analyses outlined in the thesis to determine colloid-cell interactions. Such approaches could be used as a cell-based assay for optimization of drug delivery coatings with (1) non-specific repulsion to general cell types and (2) specific attraction to an intended target cell type.

Many of the key technical hurdles have been solved, including (a) the development of image-analysis routines for precise identification of cell and colloid boundaries and (b)

optimization of surface chemistry to generate a scaffold that will both adhere cells and stabilize colloids. Examples of the tools developed in early stages of this thesis are shown in **Fig. 9.1**. Panels A and B show an example of using a conventional segmentation technique (intensity thresholding) and an optimized segmentation technique (gradient-based segmentation with morphological filtering) to detect cell boundaries in dark-field microscopy images. The cell boundaries are very accurately detected using the optimized segmentation algorithm, with significant improvement over more conventional techniques. Optimization of particle chemistry effectively adheres breast cancer cells (**Fig. 9.1C**) while stabilizing a larger fraction of polymer-coated colloids (Chapter 6). Together, these techniques improve the quantitative nature of measured interactions. As shown in **Fig. 9.1D** for a case where particles adhere to cells, the improved segmentation algorithm (black) generates a 4kT well for adhered particles. This is an improvement over the standard segmentation algorithm (blue) which generates a 2kT net interaction that is similar to that observed for non-interacting particles and cells (red).

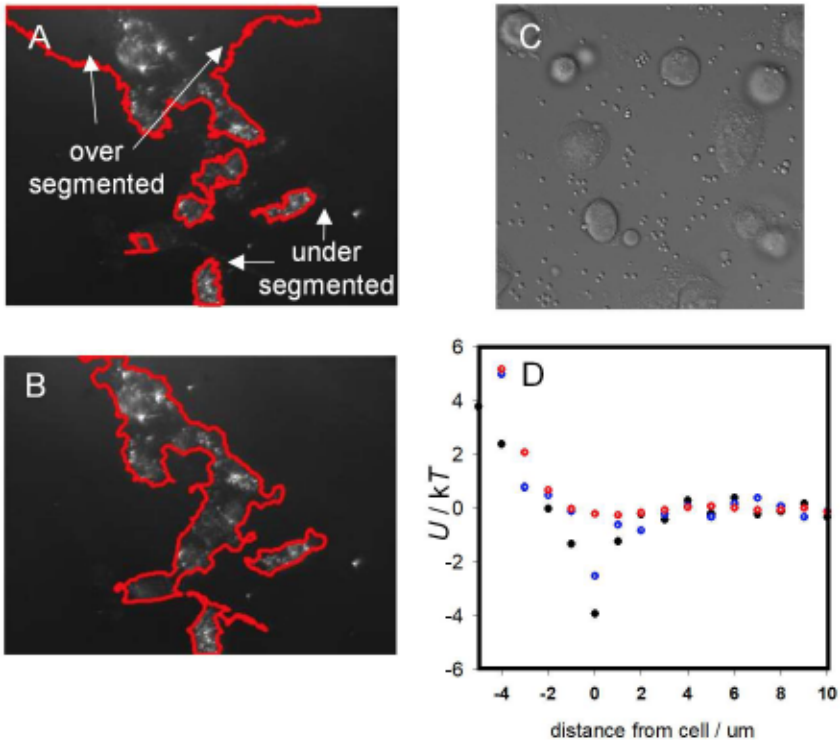

Fig. 9.1 Illustration of cell interaction measurement. (**A-B**) example of current (improved) tracking codes. (**C**) Example of hyaluronan surface that both adheres MDA241 breast cancer cells and stabilizes colloids. (**D**) Interaction measurements of polymer-coated colloids and cells. (red) 0μM specific polymer-receptor interaction with old analysis machinery; (blue) 60 μM polymer-receptor interaction with old analysis machinery; (black) 60 μM polymer-receptor interaction with updated particle tracking code.

This platform for measuring colloid-cell interactions can be used for the measurement of several parameters of key interest in the drug delivery community. First, it can provide a measure non-specific repulsion between zwitterionic polymer and cells (**Fig. 9.1D**). Such measurements can confirm many of the measurements and conclusions in Ch. 4-6 but using a less abstracted in-vitro model. More interestingly, the system may also be used to measure specific interactions between cellular membrane proteins and polymer brushes functionalized with the protein's target ligands. Such a kT, specific interaction measurement would provide the first practical system for the optimization of

targeting using multivalent weak interactions. Such measurements would empower the design of super selective drug targeting systems, an extremely hot topic in drug delivery.

9.3 Specific-ion Effects on Zwitterionic Polymer Interactions

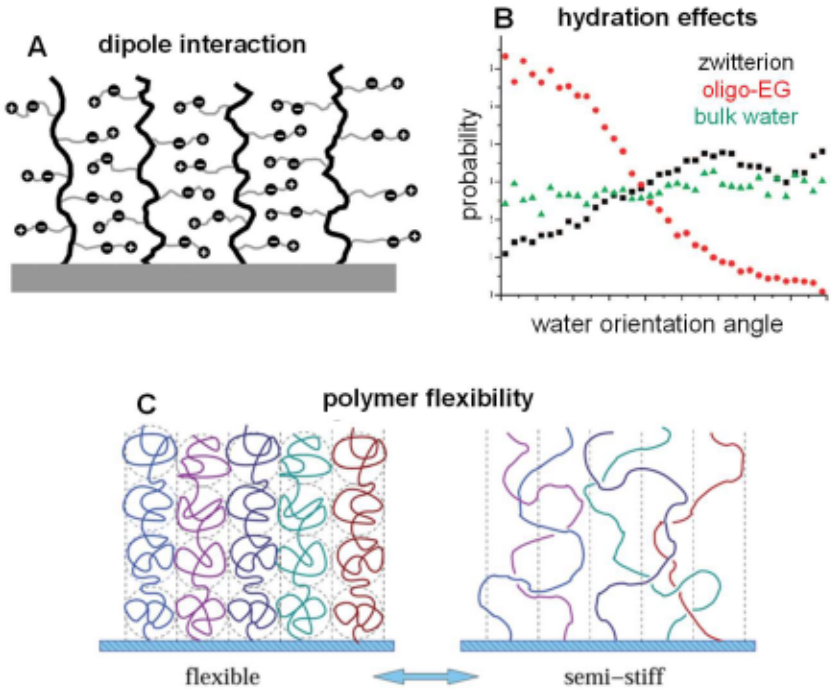

Fig. 9.2 Molecular interaction mechanisms that may cause the extended architectures of PMPC and PMAPS brushes observed in this study. The k*T*-scale interaction measurements of this study largely probe the unperturbed architecture dominated by the net solvent quality. However additional detail on molecular mechanisms may be gained through studies of solvent-quality dependent architectures and mechanical measurement of polymer compression. Figure panels are obtained from (**A**) Kikuchi et al,[63] (**B**) Shao et al[45], and (**C**) Egorov et al[116].

Chapter 7 described interaction measurements probing the effects of [NaCl] on zwitterionic polymer architectures and interactions. The manipulation of continuum-level brush behavior and architecture was used to gain molecular-level insights into the polymer-polymer and polymer-solvent interactions. While this study corroborated previous measurements of zwitterionic behavior, the proposed mechanisms were somewhat speculative and largely relied on inference from several key literature studies. The source

of the repulsive monomer-monomer interactions leading to extended brush architectures is especially uncertain. Several possibilities have been discussed in the literature. As illustrated in **Fig. 9.2**, they include a combination of chain stiffness, entropic polymer-solvent, and enthalpic polymer-polymer effects.

Additional insight into the molecular nature of zwitterionic brush behavior would be gained from solution-quality dependent measurements of polymer architectures, interactions, and solution behavior. Measurements would likely focus on manipulation of specific ion effects and temperature to disrupt polymer-solvent and polymer-polymer interactions. The effects of solvent quality could be studied with several methods, including (a) aggregation rates of colloids with polymer brushes, (b) colloidal interactions (kT-scale and mechanical), (c) SLS and solubility measurements of phase behavior and polymer-polymer interactions, and (d) neutron or x-ray scattering to measure position-dependent changes in monomer density profiles.

Fig. 9.3 gives one example of preliminary work using [$MgSO_4$] to disrupt water structure, perturbing the balance of polymer-polymer and polymer-solvent interactions. **Fig. 9.3** depicts the stability ratio W of 100nm colloids with polymer coatings. W represents the aggregation rate scaled by the diffusion-limited aggregation rate, and is plotted as a function of [$MgSO_4$] for several PEO copolymers (purple, blue, cyan), a PEO bottlebrush (diamond), bare silica (square), and the $PMPC_{28}$ copolymer from Ch. 4-7. Each colloid displays an initially large W representing stable conditions, with a rapid transition to small W (rapid aggregation) at some critical [$MgSO_4$]. The location of the critical $MgSO_4$ reflects important differences in the sensitivity of brush structure to [$MgSO_4$]. Notably, unlike the bare colloids and PEO variants, the PMPC polymer does not exhibit a critical [$MgSO_4$]

concentration. $MgSO_4$ perturbs water structure, and thus solvation, of the polymer species. The lack of dependence of PMPC coated-particles on [$MgSO_4$] may suggest that non-solvation effects such as chain stiffness may be an important contribution to the PMPC architectures and behavior.

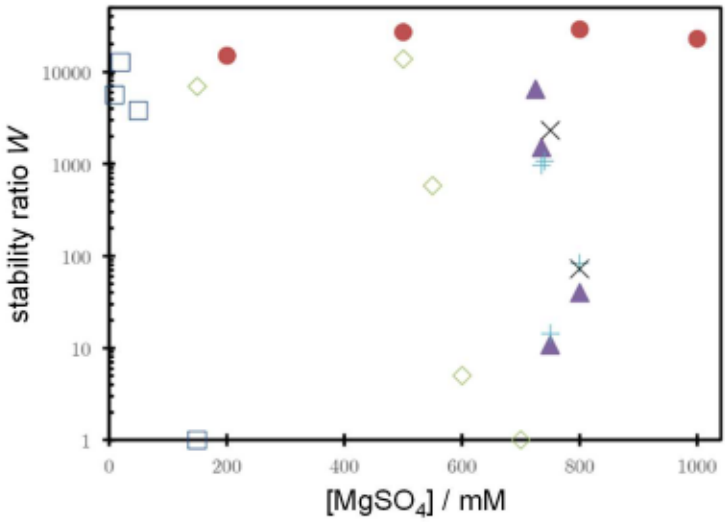

Fig. 9.3 Solvent-quality dependent aggregation of 100nm PS colloids with various polymer coatings. Stability ratio *W* is the measured aggregation rate scaled by the diffusion-limited aggregation rate. Open squares (bare), open diamond (PEO bottlebrush), triangle (PEO_{141} copolymer), cross (PEO_{100} copolymer), x (PEO_{76} copolymer), circles ($PMPC_{28}$ copolymer).

9.4 Solvent-Quality Effects on Grafted Polymer Layers

Grafting polymer from solution (graft-to) onto colloid surfaces is often favored due to its chemical simplicity and ease. However graft-to strategies typically create low-density polymer coatings due to steric hindrance from initially grafted chains during layer formation. One strategy to overcome this limitation is the manipulation of solvent quality. As demonstrated in **Fig. 9.4**, reduction of solvent quality before grafting can artificially 'shrink' the solvated volume of polymer. Grafting of the 'shrunken' polymer can create higher surface densities than grafting in a good solvent. Return of the colloids to a good

solvent for the polymer restores the solvated polymer size, forming a higher-density polymer coating than typically observed from a graft-to approach.

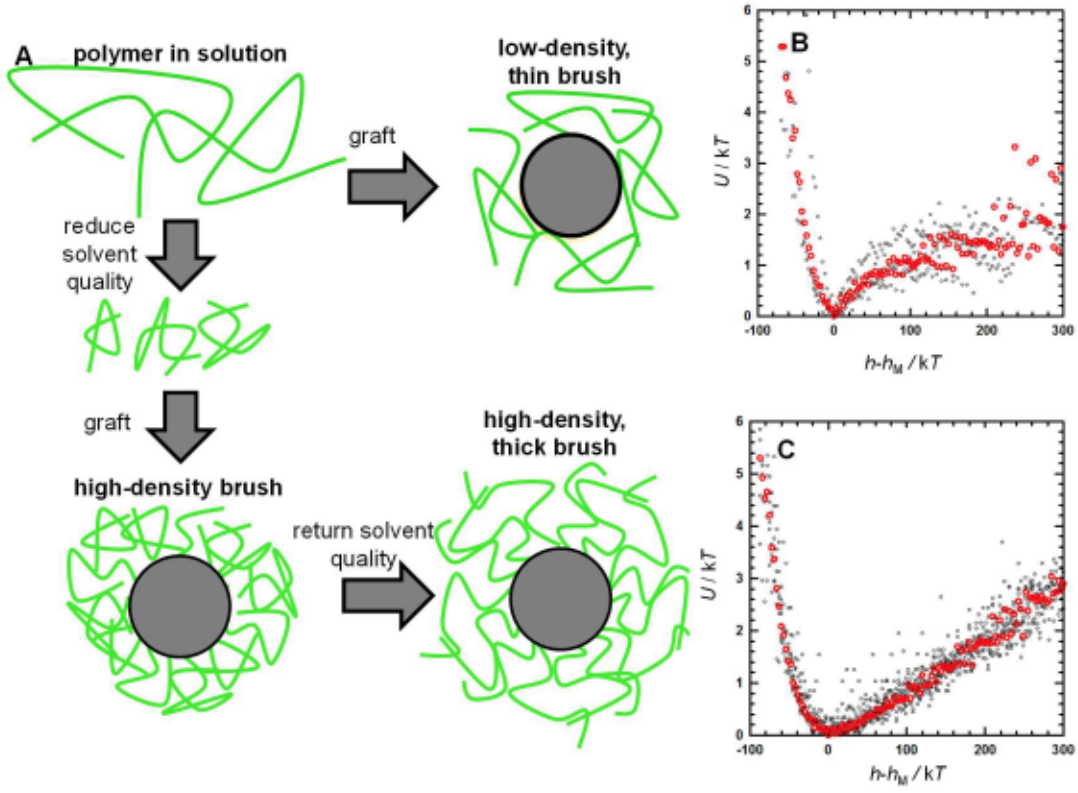

Fig. 9.4 Manipulation of solvent quality to improve graft-to brush density. (A) Conventional graft-to brush creation produces low-quality, sparsely-coated brushes. Shrinking of the polymer in reduced solvent quality can increase the density of the grafted brush. **(B)** TIRM measurement of interactions for a conventionally-grafted 15k PEO brush. Many colloids have a net attraction with polydisperse behavior. **(C)** TIRM measurement of interactions for a 15k PEO brush grafted under poor solvent condition. Single particles potentials are less polydisperse than in panel B, and with less net observed colloid-slide attraction.

This solvent-manipulation graft-to strategy has currently been tested for systems with grafted PEO and hyaluronan polymers. **Fig. 9.4B-C** are example interactions of colloids with graft-to PEO with the conventional approach in DI (panel B) and the manipulation of solvent quality with grafting in 0.5M $MgSO_4$ (panel C). Both interactions are measured in 150mM NaCl solution. The interactions for grafting in a good solvent (conventional method, **Fig. 9.4B**) are highly polydisperse, and with an attractive well for

the colloid-slide interaction. Interactions for the grafting in a poor solvent (proposed method, **Fig. 9.4C**) display less polydispersity and greater sign of colloid stability. This approach has also been applied to the grafting of hyaluronan coatings in high-ionic strength media (1M NaCl).

REFERENCES

(1) Halperin, A. Polymer Brushes That Resist Adsorption of Model Proteins: Design Parameters. *Langmuir* **1999**, *15* (7), 2525–2533.

(2) Ostuni, E.; Chapman, R. G.; Holmlin, R. E.; Takayama, S.; Whitesides, G. M. A Survey of Structure-Property Relationships of Surfaces That Resist the Adsorption of Protein. *Langmuir* **2001**, *17* (18), 5605–5620.

(3) Robinson, K. J.; Coffey, J. W.; Muller, D. A.; Young, P. R.; Kendall, M. A. F.; Thurecht, K. J.; Grøndahl, L.; Corrie, S. R. Comparison between Polyethylene Glycol and Zwitterionic Polymers as Antifouling Coatings on Wearable Devices for Selective Antigen Capture from Biological Tissue. *Biointerphases* **2015**, *10* (4), 04A305.

(4) Zhang, L.; Cao, Z.; Bai, T.; Carr, L.; Ella-Menye, J. R.; Irvin, C.; Ratner, B. D.; Jiang, S. Zwitterionic Hydrogels Implanted in Mice Resist the Foreign-Body Reaction. *Nat. Biotechnol.* **2013**, *31* (6), 553–556.

(5) Vaisocherová, H.; Yang, W.; Zhang, Z.; Cao, Z.; Cheng, G.; Piliarik, M.; Homola, J.; Jiang, S. Ultralow Fouling and Functionalizable Surface Chemistry Based on a Zwitterionic Polymer Enabling Sensitive and Specific Protein Detection in Undiluted Blood Plasma. *Anal. Chem.* **2008**, *80* (20), 7894–7901.

(6) Wilson, B.; Wu, Z. Mechanisms and Biomaterials in PH- Responsive Tumour Targeted Drug Delivery : A Review. *Biomaterials* **2016**, *85* (February), 152–167.

(7) Tibbitt, M. W.; Dahlman, J. E.; Langer, R. Emerging Frontiers in Drug Delivery. *J. Am. Chem. Soc.* **2016**, *138* (3), 704–717.

(8) Rajabzadeh, S.; Sano, R.; Ishigami, T.; Kakihana, Y.; Ohmukai, Y.; Matsuyama, H. Preparation of Hydrophilic Vinyl Chloride Copolymer Hollow Fiber Membranes with Antifouling Properties. *Appl. Surf. Sci.* **2015**, *324*, 718–724.

(9) Lu, R.; Zhang, C.; Piatkovsky, M.; Ulbricht, M.; Herzberg, M.; Nguyen, T. H. Improvement of Virus Removal Using Ultrafiltration Membranes Modified with Grafted Zwitterionic Polymer Hydrogels. *Water Res.* **2017**, *116*, 86–94.

(10) Ueda, T.; Oshida, H.; Kurita, K.; Ishihara, K.; Nakabayashi, N. Preparation of 2-Methacryloyloxyethyl Phosphorylcholine Copolymers with Alkyl Methacrylates and Their Blood Compatibility. *Polym. J.* **1992**, *24* (11), 1259–1269.

(11) Zhu, Y.; Sundaram, H. S.; Liu, S.; Zhang, L.; Xu, X.; Yu, Q.; Xu, J.; Jiang, S. A Robust Graft-to Strategy to Form Multifunctional and Stealth Zwitterionic Polymer-Coated Mesoporous Silica Nanoparticles. *Biomacromolecules* **2014**, *15* (5), 1845–1851.

(12) Zhou, T.; Qi, H.; Han, L.; Barbash, D.; Li, C. Y. Towards Controlled Polymer Brushes via a Self-Assembly-Assisted-Grafting-to Approach. *Nat. Commun.* **2016**, *7*, 1–8.

(13) Schlenoff, J. B. Zwitteration: Coating Surfaces with Zwitterionic Functionality to Reduce Nonspecific Adsorption. *Langmuir* **2014**, *30* (32), 9625–9636.

(14) Wei, Q.; Becherer, T.; Angioletti-Uberti, S.; Dzubiella, J.; Wischke, C.; Neffe, A. T.; Lendlein, A.; Ballauff, M.; Haag, R. Protein Interactions with Polymer Coatings and Biomaterials. *Angew. Chemie - Int. Ed.* **2014**, *53* (31), 8004–8031.

(15) Chen, S.; Zheng, J.; Li, L.; Jiang, S. Strong Resistance of Phosphorylcholine Self-Assembled Monolayers to Protein Adsorption: Insights into Nonfouling Properties of Zwitterionic Materials. *J. Am. Chem. Soc.* **2005**, *127* (41), 14473–14478.

(16) Joshi, S.; Pellacani, P.; Van Beek, T. A.; Zuilhof, H.; Nielen, M. W. F. Surface Characterization and Antifouling Properties of Nanostructured Gold Chips for Imaging Surface Plasmon Resonance Biosensing. *Sensors Actuators, B Chem.* **2015**, *209*, 505–514.

(17) Ostuni, E.; Chapman, R. G.; Liang, M. N.; Meluleni, G.; Pier, G.; Ingber, D. E.; Whitesides, G. M. Self-Assembled Monolayers That Resist the Adsorption of Proteins and the Adhesion of Bacterial and Mammalian Cells. *Langmuir* **2001**, *17* (20), 6336–6343.

(18) Fleer, G. J. Polymers at Interfaces and in Colloidal Dispersions. *Adv. Colloid Interface Sci.* **2010**, *159* (2), 99–116.

(19) Yamamoto, S.; Ejaz, M.; Tsujii, Y.; Matsumoto, M.; Fukuda, T. Surface Interaction Forces of Well-Defined, High-Density Polymer Brushes Studied by Atomic Force Microscopy. 1. Effect of Chain Length. *Macromolecules* **2000**, *33* (15), 5602–5607.

(20) Zhao, B.; Brittain, W. J. Polymer Brushes: Surface-Immobilized Macromolecules. *Prog. Polym. Sci.* **2000**, *25* (April), 677–710.

(21) Hansen, P. L.; Cohen, J. A.; Podgornik, R.; Parsegian, V. A. Osmotic Properties of Poly (Ethylene Glycols): Quantitative Features of Brush and Bulk Scaling Laws. *Biophys. J.* **2003**, *84* (1), 350–355.

(22) Milner, S.; Witten, T.; Cates, M. Theory of the Grafted Polymer Brush. *Macromolecules* **1988**, *21* (10), 2610–2619.

(23) Milner, S. T. Polymer Brushes. *Science (80-.).* **1991**, *251* (4996), 905–914.

(24) Chen, W.; Cordero, R.; Tran, H.; Ober, C. K. Polymer Brushes: Novel Surfaces for Future Materials. *Macromolecules* **2017**, *50*, 4089–4113.

(25) Letchford, K.; Burt, H. A Review of the Formation and Classification of Amphiphilic Block Copolymer Nanoparticulate Structures: Micelles, Nanospheres, Nanocapsules and Polymersomes. *Eur. J. Pharm. Biopharm.* **2007**, *65* (3), 259–269.

(26) Shar, J. A.; Obey, T. M.; Cosgrove, T. Adsorption Studies of Polyethers Part 1. Adsorption onto Hydrophobic Surfaces. *Colloids Surfaces A Physicochem. Eng. Asp.* **1998**, *136*, 21–33.

(27) Kozlov, M. Y.; Melik-Nubarov, N. S.; Batrakova, E. V.; Kabanov, A. V. Relationship between Pluronic Block Copolymer Structure, Critical Micellization Concentration and Partitioning Coefficients of Low Molecular Mass Solutes. *Macromolecules* **2000**, *33* (9), 3305–3313.

(28) Alexandridis, P.; Alan Hatton, T. Poly(Ethylene Oxide)-Poly(Propylene Oxide)-

Poly(Ethylene Oxide) Block Copolymer Surfactants in Aqueous Solutions and at Interfaces: Thermodynamics, Structure, Dynamics, and Modeling. *Colloids Surfaces A Physicochem. Eng. Asp.* **1995**, *96* (1–2), 1–46.

(29) Baker, J. A.; Berg, J. C. Investigation of the Adsorption Configuration of Poly (Ethylene Oxide) and Its Copolymers with Poly (Propylene Oxide) on Model Polystyrene Latex Dispersions. *Langmuir* **1988**, *4*, 1055–1061.

(30) Brandani, P.; Stroeve, P. Adsorption and Desorption of PEO - PPO - PEO Triblock Copolymers on a Self-Assembled Hydrophobic Surface. *Macromolecules* **2003**, *36*, 9492–9501.

(31) Ensign, L. M.; Cone, R.; Hanes, J. Oral Drug Delivery with Polymeric Nanoparticles: The Gastrointestinal Mucus Barriers. *Adv. Drug Deliv. Rev.* **2012**, *64* (6), 557–570.

(32) Otsuka, H.; Nagasaki, Y.; Kataoka, K. PEGylated Nanoparticles for Biological and Pharmaceutical Applications. *Adv. Drug Deliv. Rev.* **2003**, *55*, 403–419.

(33) Hoang, N. H.; Lim, C.; Sim, T.; Lee, E. S.; Youn, Y. S.; Kim, D.; Oh, K. T. Characterization of a Triblock Copolymer, Poly(Ethylene Glycol)-Polylactide-Poly(Ethylene Glycol), with Different Structures for Anticancer Drug Delivery Applications. *Polym. Bull.* **2017**, *74* (5), 1595–1609.

(34) Nag, O. K.; Awasthi, V. Surface Engineering of Liposomes for Stealth Behavior. *Pharmaceutics* **2013**, *5* (4), 542–569.

(35) Everett, W. N.; Bevan, M. A. KT-Scale Interactions between Supported Lipid Bilayers. *Soft Matter* **2013**, *10* (2), 332–342.

(36) Kawaguchi, S.; Imait, G.; Suzuki, J.; Miyahara, A. Aqueous Solution Properties of Oligo- and Poly(Ethylene Oxide) by Static Light Scattering and Intrinsic Viscosity. *Polymer (Guildf).* **1997**, *38* (12), 2885–2891.

(37) Wang, S.; Wang, C.; Chang, F.; Tsao, H. Second Virial Coefficients of Poly(Ethylene Glycol) in Aqueous Solutions at Freezing Point. *Macromolecules* **2002**, *35* (6), 9551–9555.

(38) Devanand, K.; Selser, J. C. Solutions of Poly(Ethylene Oxide). *Macromolecules* **1991**, *24*, 5943–5947.

(39) Lee, H.; Venable, R. M.; Jr, A. D. M.; Pastor, R. W. Molecular Dynamics Studies of Polyethylene Oxide and Polyethylene Glycol: Hydrodynamic Radius and Shape Anisotropy. *Biophys. J.* **2008**, *95* (August), 1590–1599.

(40) Hill, R. J. Hydrodynamics and Electrokinetics of Spherical Liposomes with Coatings of Terminally Anchored Poly(Ethylene Glycol): Numerically Exact Electrokinetics with Self-Consistent Mean-Field Polymer. *Phys. Rev. E - Stat. Nonlinear, Soft Matter Phys.* **2004**, *70* (5 1), 1–16.

(41) Musoke, M.; Luckham, P. F. Solvent Quality Dependent Interactions between Adsorbed Block Copolymers Measured by AFM. *Colloids Surfaces A Physicochem. Eng. Asp.* **2009**, *337*, 1–8.

(42) Musoke, M.; Luckham, P. F. Interaction Forces between Polyethylene Oxide – Polypropylene Oxide ABA Copolymers Adsorbed to Hydrophobic Surfaces. *J. Colloid Interface Sci.* **2004**, *277*, 62–70.

(43) Fernandes, G. E.; Bevan, M. A. Equivalent Temperature and Specific Ion Effects in Macromolecule-Coated Colloid Interactions. *Langmuir* **2007**, *23* (3), 1500–1506.

(44) Bevan, M. a.; Prieve, D. C. Forces and Hydrodynamic Interactions between Polystyrene Surfaces with Adsorbed PEO-PPO-PEO. *Langmuir* **2000**, *16* (10), 9274–9261.

(45) Shao, Q.; Jiang, S. Molecular Understanding and Design of Zwitterionic Materials. *Chem. Eng.* **2010**, *920*, 5539.

(46) Laschewsky, A. Structures and Synthesis of Zwitterionic Polymers. *Polymers (Basel).* **2014**, *6*, 1544–1601.

(47) Fujii, S.; Kido, M.; Sato, M.; Higaki, Y.; Hirai, T.; Ohta, N.; Kojio, K.; Takahara, A. PH-Responsive and Selective Protein Adsorption on an Amino Acid-Based Zwitterionic Polymer Surface. *Polym. Chem.* **2015**, *6* (39), 7053–7059.

(48) Perttu, E. K.; Szoka, F. C. Zwitterionic Sulfobetaine Lipids That Form Vesicles with Salt-Dependent Thermotropic Properties. *Chem. Commun.* **2011**, *47* (47), 12613.

(49) Yang, J.; Chen, H.; Xiao, S.; Shen, M.; Chen, F.; Fan, P.; Zhong, M.; Zheng, J. Salt-Responsive Zwitterionic Polymer Brushes with Tunable Friction and Antifouling Properties. *Langmuir* **2015**, *31*, 9125–9133.

(50) Choi, H.; Jung, Y.; Han, S.; Tak, T.; Kwon, Y. N. Surface Modification of SWRO Membranes Using Hydroxyl Poly(Oxyethylene) Methacrylate and Zwitterionic Carboxylated Polyethyleneimine. *J. Memb. Sci.* **2015**, *486*, 97–105.

(51) Welsher, K.; McManus, S. A.; Hsia, C. H.; Yin, S.; Yang, H. Discovery of Protein- and DNA-Imperceptible Nanoparticle Hard Coating Using Gel-Based Reaction Tuning. *J. Am. Chem. Soc.* **2015**, *137* (2), 580–583.

(52) Kalasin, S.; Letteri, R. A.; Emrick, T.; Santore, M. M. Adsorbed Polyzwitterion Copolymer Layers Designed for Protein Repellency and Interfacial Retention. *Langmuir* **2017**, *33*, 13708–13717.

(53) Wang, W.; Ji, X.; Kapur, A.; Zhang, C.; Mattoussi, H. A Multifunctional Polymer Combining the Imidazole and Zwitterion Motifs as a Biocompatible Compact Coating for Quantum Dots. *J. Am. Chem. Soc.* **2015**, *137* (44), 14158–14172.

(54) Yang, W.; Liu, S.; Bai, T.; Keefe, A. J.; Zhang, L.; Ella-Menye, J. R.; Li, Y.; Jiang, S. Poly(Carboxybetaine) Nanomaterials Enable Long Circulation and Prevent Polymer-Specific Antibody Production. *Nano Today* **2014**, *9* (1), 10–16.

(55) Wu, J.; Zhao, C.; Hu, R.; Lin, W.; Wang, Q.; Zhao, J.; Bilinovich, S. M.; Leeper, T. C.; Li, L.; Cheung, H. M.; et al. Probing the Weak Interaction of Proteins with Neutral and Zwitterionic Antifouling Polymers. *Acta Biomater.* **2014**, *10* (2), 751–760.

(56) Cao, Z.; Jiang, S. Super-Hydrophilic Zwitterionic Poly (Carboxybetaine) and

Amphiphilic Non-Ionic Poly (Ethylene Glycol) for Stealth Nanoparticles. *Nano Today* **2012**, *7* (5), 404–413.

(57) Shao, Q.; He, Y.; White, A. D.; Jiang, S. Difference in Hydration between Carboxybetaine and Sulfobetaine. *J. Phys. Chem. B* **2010**, *114* (49), 16625–16631.

(58) Leng, C.; Han, X.; Shao, Q.; Zhu, Y.; Li, Y.; Jiang, S.; Chen, Z. In Situ Probing of the Surface Hydration of Zwitterionic Polymer Brushes: Structural and Environmental Effects. *J. Phys. Chem. C* **2014**, *118* (29), 15840–15845.

(59) Liu, P.; Chen, Q.; Li, L.; Lin, S.; Shen, J. Anti-Biofouling Ability and Cytocompatibility of the Zwitterionic Brushes-Modified Cellulose Membrane. *J. Mater. Chem. B* **2014**, *2* (41), 7222–7231.

(60) Liu, Q.; Singh, A.; Liu, L. Amino Acid-Based Zwitterionic Poly(Serine Methacrylate) as an Antifouling Material. *Biomacromolecules* **2013**, *14* (1), 226–231.

(61) Xing, C. M.; Meng, F. N.; Quan, M.; Ding, K.; Dang, Y.; Gong, Y. K. Quantitative Fabrication, Performance Optimization and Comparison of PEG and Zwitterionic Polymer Antifouling Coatings. *Acta Biomater.* **2017**, *59*, 129–138.

(62) Shi, S.; Huang, Y.; Chen, X.; Weng, J.; Zheng, N. Optimization of Surface Coating on Small Pd Nanosheets for in Vivo Near-Infrared Photothermal Therapy of Tumor. *ACS Appl. Mater. Interfaces* **2015**, *7* (26), 14369–14375.

(63) Kikuchi, M.; Terayama, Y.; Ishikawa, T.; Hoshino, T.; Kobayashi, M.; Ogawa, H.; Masunaga, H.; Koike, J. I.; Horigome, M.; Ishihara, K.; et al. Chain Dimension of Polyampholytes in Solution and Immobilized Brush States. *Polym. J.* **2012**, *44* (1), 121–130.

(64) Kobayashi, M.; Ishihara, K.; Takahara, A. Neutron Reflectivity Study of the Swollen Structure of Polyzwitterion and Polyeletrolyte Brushes in Aqueous Solution. *J. Biomater. Sci. Polym. Ed.* **2014**, *25* (14–15), 1673–1686.

(65) Terayama, Y.; Arita, H.; Ishikawa, T.; Kikuchi, M.; Mitamura, K.; Kobayashi, M.; Yamada, N. L.; Takahara, A. Chain Dimensions in Free and Immobilized Brush States of Polysulfobetaine in Aqueous Solution at Various Salt Concentrations. *J. Phys. Conf. Ser.* **2011**, *272* (1).

(66) Kobayashi, M.; Mitamura, K.; Terada, M.; Yamada, N. L.; Takahara, A. Characterization of Swollen States of Polyelectrolyte Brushes in Salt Solution by Neutron Reflectivity. *J. Phys. Conf. Ser.* **2011**, *272* (1).

(67) Iuster, N.; Tairy, O.; Driver, M. J.; Armes, S. P.; Klein, J. Cross-Linking Highly Lubricious Phosphocholinated Polymer Brushes: Effect on Surface Interactions and Frictional Behavior. *Macromolecules* **2017**, *50* (18), 7361–7371.

(68) Chen, M.; Briscoe, W. H.; Armes, S. P.; Klein, J. Lubrication at Physiological Pressures by Polyzwitterionic Brushes. *Science (80-.).* **2009**, *323* (5922), 1698–1701.

(69) Tairy, O.; Kampf, N.; Driver, M. J.; Armes, S. P.; Klein, J. Dense, Highly Hydrated Polymer Brushes via Modified Atom-Transfer-Radical-Polymerization: Structure,

Surface Interactions, and Frictional Dissipation. *Macromolecules* **2015**, *48* (1), 140–151.

(70) Schön, P.; Kutnyanszky, E.; Santonicola, M. G.; Tecim, T.; Aldred, N.; Clare, A. S.; Vancso, G. J. Probing Biofouling Resistant Polymer Brush Surfaces by Atomic Force Microscopy Based Force Spectroscopy. *Colloids Surfaces B Biointerfaces* **2013**, *102*, 923–930.

(71) Simon, a; Cohen-Bouhacina, T.; Porté, M. C.; Aimé, J. P.; Baquey, C. Study of Two Grafting Methods for Obtaining a 3-Aminopropyltriethoxysilane Monolayer on Silica Surface. *J. Colloid Interface Sci.* **2002**, *251* (2), 278–283.

(72) Zhang, Z.; Moxey, M.; Alswieleh, A.; Morse, A. J.; Lewis, A. L.; Geoghegan, M.; Leggett, G. J. Effect of Salt on Phosphorylcholine-Based Zwitterionic Polymer Brushes. *Langmuir* **2016**, *32* (20), 5048–5057.

(73) Russel, W. B.; Saville, D. A.; Schowalter, W. R. *Colloidal Dispersions*; Cambridge University Press: Cambridge and New York, 1991.

(74) Wu, H.-J.; Pangburn, T. O.; Beckham, R. E.; Bevan, M. a. Measurement and Interpretation of Particle-Particle and Particle-Wall Interactions in Levitated Colloidal Ensembles. *Langmuir* **2005**, *21* (22), 9879–9888.

(75) Bitter, J. L.; Duncan, G. A.; Beltran-villegas, D. J.; Fairbrother, D. H.; Bevan, M. A. Anomalous Silica Colloid Stability and Gel Layer Mediated Interactions. *Langmuir* **2013**, *29*, 8835–8844.

(76) Milner, S. Compressing Polymer Brushes: A Quantitative Comparison of Theory and Experiment. *Europhys. Lett.* **1988**, *7* (8), 695–699.

(77) Ball, R. C.; Marko, J. F.; Witten, T. A.; Milner, S. T. Polymers Grafted to a Convex Surface. *Macromolecules* **1991**, *24* (3), 693–703.

(78) Li, H.; Witten, T. A. Polymers Grafted to Convex Surfaces: A Variational Approach. *Macromolecules* **1994**, *27* (2), 449–457.

(79) Lin, S.; Wiesner, M. R. Theoretical Investigation on the Steric Interaction in Colloidal Deposition. *Langmuir* **2012**, *28* (43), 15233–15245.

(80) Eichmann, S. L.; Meric, G.; Swavola, J. C.; Bevan, M. A. Diffusing Colloidal Probes of Protein-Carbohydrate Interactions. *Langmuir* **2013**, *29* (7), 2299–2310.

(81) Pavliotis, G. A. *Stochastic Processes and Applications*; Antman, S., Greengard, L., Holmes, P., Eds.; Springer: London, 2014; Vol. 60.

(82) Risken, H. *Risken, H.*, 2nd ed.; Haken, H., Ed.; Springer-Verlag: New York, 1989.

(83) Happel, J.; Brenner, H. *Low Reynolds Number Hydrodynamics, 1965*; 1983.

(84) Bevan, M. a.; Prieve, D. C. Hindered Diffusion of Colloidal Particles Very near to a Wall: Revisited. *J. Chem. Phys.* **2000**, *113* (3), 1228.

(85) Beckham, R. E. *CONFOCAL MICROSCOPY STUDY OF COLLOIDAL SEDIMENTATION AND CRYSTALLIZATION*; Texas A&M University: College Station, 2008.

(86) Marx, K. A. Quartz Crystal Microbalance: A Useful Tool for Studying Thin Polymer Films and Complex Biomolecular Systems at the Solution - Surface Interface. *Biomacromolecules* **2003**, *4* (5), 1099–1120.

(87) Baba, A.; Taranekar, P.; Ponnapati, R. R.; Knoll, W.; Advincula, R. C. Electrochemical Surface Plasmon Resonance and Waveguide-Enhanced Glucose Biosensing with N-Alkylaminated Polypyrrole/Glucose Oxidase Multilayers. *ACS Appl. Mater. Interfaces* **2010**, *2* (8), 2347–2354.

(88) Lai, S. K.; O'Hanlon, D. E.; Harrold, S.; Man, S. T.; Wang, Y.-Y.; Cone, R.; Hanes, J. Rapid Transport of Large Polymeric Nanoparticles in Fresh Undiluted Human Mucus. *Proc. Natl. Acad. Sci. U. S. A.* **2007**, *104* (5), 1482–1487.

(89) Curtis, C.; Toghani, D.; Wong, B.; Nance, E. Colloidal Stability as a Determinant of Nanoparticle Behavior in the Brain. *Colloids Surfaces B Biointerfaces* **2018**, *170* (March), 673–682.

(90) He, M.; Gao, K.; Zhou, L.; Jiao, Z.; Wu, M.; Cao, J.; You, X.; Cai, Z.; Su, Y.; Jiang, Z. Zwitterionic Materials for Antifouling Membrane Surface Construction. *Acta Biomater.* **2016**, *40* (92), 142–152.

(91) Zhang, G.; Yang, Z.; Lu, W.; Zhang, R.; Huang, Q.; Tian, M.; Li, L.; Liang, D.; Li, C. Influence of Anchoring Ligands and Particle Size on the Colloidal Stability and in Vivo Biodistribution of Polyethylene Glycol-Coated Gold Nanoparticles in Tumor-Xenografted Mice. *Biomaterials* **2009**, *30*, 1928–1936.

(92) Tria, M. C. R.; Grande, C. D. T.; Ponnapati, R. R.; Advincula, R. C. Electrochemical Deposition and Surface-Initiated RAFT Polymerization: Protein and Cell-Resistant PPEGMEMA Polymer Brushes. *Biomacromolecules* **2010**, *11* (12), 3422–3431.

(93) Yasin, S.; Luckham, P. F. Investigating the Effectiveness of PEO/PPO Based Copolymers as Dispersing Agents for Graphitic Carbon Black Aqueous Dispersions. *Colloids Surfaces A Physicochem. Eng. Asp.* **2012**, *404*, 25–35.

(94) Kostarelos, K.; Tadros, T. F.; Luckham, P. F. Physical Conjugation of (Tri-) Block Copolymers to Liposomes toward the Construction of Sterically Stabilized Vesicle Systems. *Langmuir* **1999**, *15* (2), 369–376.

(95) Alswieleh, A. M.; Cheng, N.; Canton, I.; Ustbas, B.; Xue, X.; Ladmiral, V.; Xia, S.; Ducker, R. E.; El Zubir, O.; Cartron, M. L.; et al. Zwitterionic Poly(Amino Acid Methacrylate) Brushes. *J. Am. Chem. Soc.* **2014**, *136* (26), 9404–9413.

(96) Yang, W.; Zhang, L.; Wang, S.; White, A. D.; Jiang, S. Functionalizable and Ultra Stable Nanoparticles Coated with Zwitterionic Poly(Carboxybetaine) in Undiluted Blood Serum. *Biomaterials* **2009**, *30* (29), 5617–5621.

(97) Shao, Q.; He, Y.; Jiang, S. Molecular Dynamics Simulation Study of Ion Interactions with Zwitterions. *J. Phys. Chem. B* **2011**, *115* (25), 8358–8363.

(98) Wang, B.; Li, B.; Dong, B.; Zhao, B.; Li, C. Y. Homo- and Hetero-Particle Clusters Formed by Janus Nanoparticles with Bicompartment Polymer Brushes. *Macromolecules* **2010**, *43* (22), 9234–9238.

(99) Boyes, S. G.; Granville, A. M.; Baum, M.; Akgun, B.; Mirous, B. K.; Brittain, W. J.

Recent Advances in the Synthesis and Rearrangement of Block Copolymer Brushes. In *Polymer Brushes: Synthesis, Characterization, Applications*; Advincula, R. C., Brittain, W. J., Caster, K. C., Rühe, J., Eds.; Wiley-VCH Verlag GmbH & Co, 2004.

(100) Doncom, K. E. B.; Willcock, H.; O'Reilly, R. K. The Direct Synthesis of Sulfobetaine-Containing Amphiphilic Block Copolymers and Their Self-Assembly Behavior. *Eur. Polym. J.* **2017**, *87*, 497–507.

(101) Jiménez, Z. A.; Yoshida, R. Temperature Driven Self-Assembly of a Zwitterionic Block Copolymer That Exhibits Triple Thermoresponsivity and PH Sensitivity. *Macromolecules* **2015**, *48* (13), 4599–4606.

(102) Mäkinen, L.; Varadharajan, D.; Tenhu, H.; Hietala, S. Triple Hydrophilic UCST-LCST Block Copolymers. *Macromolecules* **2016**, *49* (3), 986–993.

(103) Canning, S. L.; Neal, T. J.; Armes, S. P. PH-Responsive Schizophrenic Diblock Copolymers Prepared by Polymerization-Induced Self-Assembly. *Macromolecules* **2017**, *50* (16), 6108–6116.

(104) Dembele, F.; Tasso, M.; Trapiella-Alfonso, L.; Xu, X.; Hanafi, M.; Lequeux, N.; Pons, T. Zwitterionic Silane Copolymer for Ultra-Stable and Bright Biomolecular Probes Based on Fluorescent Quantum Dot Nanoclusters. *ACS Appl. Mater. Interfaces* **2017**, *9* (21), 18161–18169.

(105) Kobayashi, M.; Terayama, Y.; Hosaka, N.; Kaido, M.; Suzuki, A.; Yamada, N.; Torikai, N.; Ishihara, K.; Takahara, A. Friction Behavior of High-Density Poly(2-Methacryloyloxyethyl Phosphorylcholine) Brush in Aqueous Media. *Soft Matter* **2007**, *3* (6), 740–746.

(106) Zhang, Z.; Morse, A. J.; Armes, S. P.; Lewis, A. L.; Geoghegan, M.; Leggett, G. J. Nanoscale Contact Mechanics of Biocompatible Polyzwitterionic Brushes. *Langmuir* **2013**, *29* (34), 10684–10692.

(107) Bagchi, P. Theory of Stabilization of Spherical Colloidal Particles by Nonionic Polymers. *J. Colloid Interface Sci.* **1974**, *47* (1), 86–99.

(108) Wu, H.; Bevan, M. A. Particle - Surface Potential Energy Profiles. *Langmuir* **2005**, *21*, 1244–1254.

(109) Kobayashi, M.; Terayama, Y.; Kikuchi, M.; Takahara, A. Chain Dimensions and Surface Characterization of Superhydrophilic Polymer Brushes with Zwitterion Side Groups. *Soft Matter* **2013**, *9* (21), 5138.

(110) Voinova, M. V.; Rodahl, M.; Jonson, M.; Kasemo, B. Viscoelastic Acoustic Response of Layered Polymer Films at Fluid-Solid Interfaces: Continuum Mechanics Approach. *Phys. Scr.* **1999**, *59*, 391–396.

(111) Wu, H.; Shah, S.; Beckham, R.; Meissner, K. E.; Bevan, M. a. Resonant Effects in Evanescent Wave Scattering of Polydisperse Colloids. *Society* **2008**, *24* (November), 13790–13795.

(112) Everett, W. N.; Wu, H.-J.; Anekal, S. G.; Sue, H.-J.; Bevan, M. a. Diffusing Colloidal Probes of Protein and Synthetic Macromolecule Interactions. *Biophys. J.* **2007**, *92* (3), 1005–1013.

(113) Johannsmann, D. Viscoelastic, Mechanical, and Dielectric Measurements on Complex Samples with the Quartz Crystal Microbalance. *Phys. Chem. Chem. Phys.* **2008**, *10* (31), 4516.

(114) Reviakine, I.; Johannsmann, D.; Richter, R. P. Hearing What You Cannot See and Visualizing What You Hear: Interpreting Quartz Crystal Microbalance Data from Solvated Interfaces. *Anal. Chem.* **2011**, *83* (23), 8838–8848.

(115) Matsuda, Y.; Kobayashi, M.; Annaka, M.; Ishihara, K.; Takahara, A. Dimensions of a Free Linear Polymer and Polymer Immobilized on Silica Nanoparticles of a Zwitterionic Polymer in Aqueous Solutions with Various Ionic Strengths. *Langmuir* **2008**, *24*, 8772–8778.

(116) Egorov, S. A.; Hsu, H.; Milchev, A.; Binder, K. Semi Fl Exible Polymer Brushes and the Brush- Mushroom Crossover. *Soft Matter* **2015**, *11*, 2604–2616.

(117) Hsu, H.; Binder, K. Stretching Semiflexible Polymer Chains : Evidence for the Importance of Excluded Volume Effects from Monte Carlo Simulation. *J. Chem. Phys.* **2012**, *136*, 024901-1-024901-3.

(118) Milchev, A.; Binder, K. Semiflexible Polymers Grafted to a Solid Planar Substrate: Changing the Structure from Polymer Brush to " Polymer Bristle ." *J. Chem. Phys.* **2012**, *136* (194901).

(119) de Vos, W. M.; Leermakers, F. A. M. Modeling the Structure of a Polydisperse Polymer Brush. *Polymer (Guildf).* **2009**, *50* (1), 305–316.

(120) Milner, S. T.; Witten, T. A.; Cates, M. E. Effects of Polydispersity in the End-Grafted Polymer Brush. *Macromolecules* **1989**, *22*, 853–861.

(121) Kharlampieva, E.; Izumrudov, V. A.; Sukhishvili, S. A. Electrostatic Layer-by-Layer Self-Assembly of Poly(Carboxybetaine)s: Role of Zwitterions in Film Growth. *Macromolecules* **2007**, *40* (10), 3663–3668.

(122) Salloum, D. S.; Olenych, S. G.; Keller, T. C. S.; Schlenoff, J. B. Vascular Smooth Muscle Cells on Polyelectrolyte Multilayers: Hydrophobicity-Directed Adhesion and Growth. *Biomacromolecules* **2005**, *6* (1), 161–167.

(123) Coughlan, A. C. H.; Torres-Diaz, I.; Jerri, H. A.; Bevan, M. A. Direct Measurements of *KT* -Scale Capsule–Substrate Interactions and Deposition Versus Surfactants and Polymer Additives. *ACS Appl. Mater. Interfaces* **2018**, acsami.8b06987.

(124) Dan, N.; Tirrell, M. Polymers Tethered to Curved Interfaces. A Self-Consistent-Field Analysis. *Macromolecules* **1992**, *25* (11), 2890–2895.

(125) Pailthorpe, B. A.; Russe, W. B. The Retarded van Der Waals Interaction between Spheres. *J. colloid interface Sci.* **1982**, *89* (2), 563–566.

(126) Chang, Y.; Yandi, W.; Chen, W. Y.; Shih, Y. J.; Yang, C. C.; Chang, Y.; Ling, Q. D.; Higuchi, A. Tunable Bioadhesive Copolymer Hydrogels of Thermoresponsive Poly(N -Isopropyl Acrylamide) Containing Zwitterionic Polysulfobetaine. *Biomacromolecules* **2010**, *11* (4), 1101–1110.

(127) Feng, W.; Brash, J. L.; Zhu, S. Non-Biofouling Materials Prepared by Atom

Transfer Radical Polymerization Grafting of 2-Methacryloloxyethyl Phosphorylcholine: Separate Effects of Graft Density and Chain Length on Protein Repulsion. *Biomaterials* **2006**, *27* (6), 847–855.

(128) Zhang, Z.; Chao, T.; Chen, S.; Jiang, S. Superlow Fouling Sulfobetaine and Carboxybetaine Polymers on Glass Slides. *Langmuir* **2006**, *22* (24), 10072–10077.

(129) Estephan, Z. G.; Jaber, J. A.; Schlenoff, J. B.; States, U. Zwitterion-Stabilized Silica Nanoparticles: Toward Nonstick Nano. *Langmuir* **2010**, *26* (22), 16884–16889.

(130) Dong, Z.; Mao, J.; Yang, M.; Wang, D.; Bo, S.; Ji, X. Phase Behavior of Poly(Sulfobetaine Methacrylate)-Grafted Silica Nanoparticles and Their Stability in Protein Solutions. *Langmuir* **2011**, *27* (24), 15282–15291.

(131) Petroff, M. G.; Garcia, E. A.; Herrera-Alonso, M.; Bevan, M. A. KT-Scale Interactions and Stability of Colloids with Adsorbed Ethylene Oxide and Zwitterionic Polymers. *Macromol. (under Rev.* **2018**.

(132) Duncan, G. A.; Howard, D.; Bevan, M. A. Diffusing Colloidal Probes of Cell Surfaces. *Soft Matter* **2016**, *12*, 4731–4738.

(133) Wu, H. J.; Everett, W. N.; Anekal, S. G.; Bevan, M. a. Mapping Patterned Potential Energy Landscapes with Diffusing Colloidal Probes. *Langmuir* **2006**, *22* (16), 6826–6836.

(134) Duncan, G. A.; Gerecht, S.; Fairbrother, D. H.; Bevan, M. A. Diffusing Colloidal Probes of KT -Scale Biomaterial − Cell Interactions. *Langmuir* **2016**, *32*, 1212–1220.

(135) Chang, Y.; Chen, S.; Zhang, Z.; Jiang, S. Highly Protein-Resistant Coatings from Well-Defined Diblock Copolymers Containing Sulfobetaines. *Langmuir* **2006**, *22* (5), 2222–2226.

(136) Lu, P.; Weaver, V. M.; Werb, Z. The Extracellular Matrix: A Dynamic Niche in Cancer Progression. *J. Cell Biol.* **2012**, *196* (4), 395–406.

(137) Cone, R. A. Barrier Properties of Mucus. *Adv. Drug Deliv. Rev.* **2009**, *61* (2), 75–85.

(138) Curtis, C.; Zhang, M.; Liao, R.; Wood, T.; Nance, E. Systems-Level Thinking for Nanoparticle-Mediated Therapeutic Delivery to Neurological Diseases. *Wiley Interdiscip. Rev. Nanomedicine Nanobiotechnology* **2017**, *9* (2).

(139) Swavola, J. C.; Edwards, T. D.; Bevan, M. A. Direct Measurement of Macromolecule Coated Colloid-Mucus Interactions. *Langmuir* **2015**, *31*, 9076–9085.

(140) Mi, L.; Jiang, S. Integrated Antimicrobial and Nonfouling Zwitterionic Polymers. *Angew. Chemie - Int. Ed.* **2014**, *53* (7), 1746–1754.

(141) Kikuchi, M.; Terayama, Y.; Ishikawa, T.; Hoshino, T.; Kobayashi, M.; Ohta, N.; Jinnai, H.; Takahara, A. Salt Dependence of the Chain Stiffness and Excluded-Volume Strength for the Polymethacrylate-Type Sulfopropylbetaine in Aqueous NaCl Solutions. *Macromolecules* **2015**, *48* (19), 7194–7204.

(142) Shao, Q.; Jiang, S. Influence of Charged Groups on the Properties of Zwitterionic Moieties: A Molecular Simulation Study. *J. Phys. Chem. B* **2014**, *118* (27), 7630–7637.

(143) Kutnyanszky, E.; Vansco, G. J. Nanomechanical Properties of Polymer Brushes by Colloidal AFM Probes. *Eur. Polym. J.* **2012**, *48* (1), 8–15.

(144) Sakata, S.; Inoue, Y.; Ishihara, K. Molecular Interaction Forces Generated during Protein Adsorption to Well-Defined Polymer Brush Surfaces. *Langmuir* **2015**, *31* (10), 3108–3114.

(145) Bevan, M. A.; Scales, P. . Solvent Quality Dependent Interactions and Phase Behavior of Polystyrene Particles with Physisorbed PEO-PPO-PEO. *Langmuir* **2002**, *18* (5), 1474–1484.

(146) Kim, J. U.; Matsen, M. W. Interaction between Polymer-Grafted Particles. *Macromolecules* **2008**, *41* (12), 4435–4443.

(147) Laloyaux, X.; Mathy, B.; Nysten, B.; Jonas, A. M. Surface and Bulk Collapse Transitions of Thermoresponsive Polymer Brushes. *Langmuir* **2010**, *26* (2), 838–847.

(148) Lavanant, L.; Paripovic, D.; Schu, N.; Sugnaux, C.; Tugulu, S.; Klok, H. Polymer Brushes via Surface-Initiated Controlled Radical Polymerization: Synthesis, Characterization, Properties, and Applications. *Chem. Rev.* **2009**, *109* (11), 5437–5527.

(149) Higaki, Y.; Inutsuka, Y.; Sakamaki, T.; Terayama, Y.; Takenaka, A.; Higaki, K.; Yamada, N. L.; Moriwaki, T.; Ikemoto, Y.; Takahara, A. Effect of Charged Group Spacer Length on Hydration State in Zwitterionic Poly(Sulfobetaine) Brushes. *Langmuir* **2017**, *33*, 8404–8412.

(150) Weers, J. G.; Rathman, J. F.; Axe, F. U.; Crichlow, C. A.; Foland, L. D.; Scheuing, D. R.; Wiersema, R. J.; Zielske, A. G. Effect of the Intramolecular Charge Separation Distance on the Solution Properties of Betaines and Sulfobetaines. *Langmuir* **1991**, *7* (5), 854–867.

(151) Mary, P.; Bendejacq, D. D.; Labeau, M.-P.; Dupuis, P. Reconciling Low-and High-Salt Solution Behavior of Sulfobetaine Polyzwitterions. *J. Phys. Chem. B* **2007**, *111*, 7767–7777.

(152) Higgs, P. G.; Joanny, J. Theory of Polyampholyte Solutions. *J. Chem. Phys.* **1991**, *94*, 1543–1554.

(153) Kato, T.; Takahashi, A. Excluded Volume Effects of Sulphobetaine Polymers. *Ber. Bunenges. Phys. Chem.* **1996**, *100*, 784–787.

(154) Morita, S.; Tanaka, M. Effect of Sodium Chloride on Hydration Structures of PMEA and P(MPC- R -BMA). *Langmuir* **2014**, *30* (35), 10698–10703.

(155) Morozova, S.; Hu, G.; Emrick, T.; Muthukumar, M. Influence of Dipole Orientation on Solution Properties of Polyzwitterions. *ACS Macro Lett.* **2016**, *5* (1), 118–122.

(156) Kamiyamat, Y.; Israelachvili, J. Effect of PH and Salt on the Adsorption and

Interactions of an Amphoteric Polyelectrolyte. *Macromolecules* **1992**, *25*, 5081–5088.

(157) Higaki, Y.; Fröhlich, B.; Yamamoto, A.; Murakami, R.; Kaneko, M.; Takahara, A.; Tanaka, M. Ion-Specific Modulation of Interfacial Interaction Potentials between Solid Substrates and Cell-Sized Particles Mediated via Zwitterionic, Super-Hydrophilic Poly(Sulfobetaine) Brushes. *J. Phys. Chem. B* **2017**, *121* (6), 1396–1404.

(158) Marsh, D. *CRC Handbook of Lipid Bilayers*; 1990.

(159) Bhattacharjee, S. DLS and Zeta Potential - What They Are and What They Are Not? *J. Control. Release* **2016**, *235*, 337–351.

(160) Neal, B. L.; Asthagiri, D.; Velev, O. D.; Lenhoff, A. M.; Kaler, E. W. Why Is the Osmotic Second Virial Coefficient Related to Protein Crystallization? *J. Cryst. Growth* **1999**, *196* (2–4), 377–387.

(161) Yamakawa, H. The Radius Expansion Factor and Second Virial Coefficient for Polymer Chains below the Theta Temperature. *Macromolecules* **1993**, *2626* (19), 5061–5066.

(162) Mashaghi, A.; Partovi-Azar, P.; Jadidi, T.; Nafari, N.; Maass, P.; Tabar, M. R. R.; Bonn, M.; Bakker, H. J. Hydration Strongly Affects the Molecular and Electronic Structure of Membrane Phospholipids. *J. Chem. Phys.* **2012**, *136* (11), 114709.

(163) Mathis, A.; Zheng, Y. L.; Galin, J. C. Random Ethylacrylate Zwitterionic Copolymers: 3. Microphase Separation as a Function of the Zwitterion Structure. *Polymer (Guildf).* **1991**, *32* (17), 3080–3085.

(164) Ishihara, K.; Mu, M.; Konno, T.; Inoue, Y.; Fukazawa, K. The Unique Hydration State of Poly(2-Methacryloyloxyethyl Phosphorylcholine). *J. Biomater. Sci. Polym. Ed.* **2017**, *28* (10–12), 884–899.

VITA

Name: Matthew G. Petroff

Birth: Feb 20, 1987, Chicago Illinois

Address: Matthew G. Petroff may be contacted through Dr. M. A. Bevan at the Chemical and Biomolecular Engineering Department, Johns Hopkins University, Baltimore, MD 21218

Email Address: mpetrof3@jhu.edu, mattpetroff@gmail.com

Education: B.S., Chemical Engineering, University of Delaware,

Newark, DE, 2009

Research:

2006-2009

Transport and adsorption of proteins in polymer-modified chromatography adsorbents

Advisor A.M. Lenhoff, Newark DE, 19711

2009-2013

Development and optimization of processes for the purification of recombinant therapeutic proteins

Merck and Co., manager T. Linden